Albitization and REE-U-enrichment in IOCG systems: Insights from Moonta-Wallaroo, Yorke Peninsula, South Australia

Thesis submitted in accordance with the requirements of the University of Adelaide for an Honours Degree in Geology

Alkiviadis Kontonikas-Charos

November 2013

THE UNIVERSITY of ADELAIDE

ALBITIZATION AND REE-U-ENRICHMENT IN IOCG SYSTEMS: INSIGHTS FROM MOONTA-WALLAROO, YORKE PENINSULA, SOUTH AUSTRALIA

ALBITIZATION AND REE-U: MOONTA-WALLAROO

ABSTRACT

Iron Oxide Copper Gold (IOCG) deposits are the products of crustal-scale metasomatic alteration, generally considered to be associated with the emplacement of large felsic intrusions. These systems are typified by zoned, broad alteration haloes comprising the products of an early, barren albitization event, and late, ore-hosting potassic/calcic (skarn) alteration associated with mineralization. Yttrium and rare earth elements (REY), and also uranium, are prominent components of most IOCG systems. The REY-signatures of feldspars and accessory apatite, Fe-(Ti)-oxides and other minerals are geochemical tracers of alteration stages within a magmatic-hydrothermal system.

This study sets out to identify links between magmatism and initiation of hydrothermal activity, and to test the hypothesis that albitization is a pre-requisite stage for REE-U enrichment in magmatically-derived IOCG systems. The compositions and trace element concentrations in key minerals have been analysed using scanning electron microscopy, electron probe microanalysis and laser-ablation inductively-coupled plasma mass spectrometry in a varied range of magmatic to metasedimentary lithologies from the Moonta-Wallaroo region, an area in which broad regional-scale alkali alteration is recognised.

Results confirm a strong link between albitization and REE-U-enrichment. The process of albitization is seen to consume, redistribute and lock-in REY, LILE and HFSE via complex fluid-rock reactions dependent on the pre-existing mineral assemblages and fluid characteristics, providing a holistic model for IOCG-driven alkali metasomatism. The trace element signatures recorded by K-feldspar reflect a transition from magmatic to hydrothermal stages within an evolving IOCG system.

Although further constraints on these signatures are required, they could prove invaluable in mineral exploration as they suggest a quantifiable distinction between alteration associated with mineralization, and regional background. This hypothesis requires testing elsewhere in the Olympic Province and in analogous terranes.

KEYWORDS

Albitization, REE-U enrichment, IOCG, Feldspar, Trace elements, Moonta-Wallaroo

TABLE OF CONTENTS

LIST OF FIGURES AND TABLES

INTRODUCTION

Iron Oxide Copper Gold (IOCG) mineralization is presently considered part of a broad group of deposit types that form within ore systems spanning from Archean to Phanerozoic in age (Groves *et al.* 2010). These systems are typified by zoned, broad alteration haloes comprising early, barren albite, and late, ore-hosting potassic/calcic (skarn) alteration (subdivided into deeper K-feldspar + biotite and upper sericite (hydrolytic) shells, where magnetite and hematite are the typical Fe-oxides, respectively). Formation models for these deposits are still debated, particularly regarding typical metal source(s), fluids and geodynamic settings (e.g. Barton & Johnson 2004; Williams *et al.* 2005; Chiaradia *et al.* 2006; Pollard *et al.* 2007; Groves *et al.* 2010).

The Olympic Province, Eastern Gawler Craton, South Australia (Skirrow *et al.* 2007) is one of the archetypal Mesoproterozoic examples of giant IOCG provinces. The conceptualisation of IOCG deposits relies on the Cu-Au-U deposit at Olympic Dam (OD), (Figure 1a; Hitzman *et al.* 1992), which contains the largest known concentration of U, under exploitation (Hitzman & Valenta 2005; Cuney 2010), as well as the one of the largest known occurrences of Rare Earth Elements (REE) on Earth. Uranium and REE mineralization is related to the presence of discrete U- and REE-minerals formed late in the mineralization sequence. Hence, typical deposit characteristics include: large tonnages, low Cu and Au grades, large, granite-hosted breccia bodies, and typically, an Fe-oxide (magnetite and hematite) matrix hosting the Cu-Au-U ore.

The different alteration styles and metal endowment in IOCG systems vary widely throughout the Olympic Province (e.g. Skirrow *et al.* 2007; Hayward & Skirrow 2010), raising the question of what are the typical features in the alteration halo that can track the archetypal, 'fertile' OD model? The Moonta-Wallaroo area is known for past exploitation of small Cu-Au veins (Figure 1) hosted within porphyry-felsic rocks with potassic (K-feldspar) alteration (Conor *et al.* 2010). This region is also an example of an IOCG terrane in which broad regional-scale alkali alteration is recognised in different lithologies (e.g. Cowley *et al.* 2003; Conor *et al.* 2010), ranging from magmatic to metasedimentary rocks, and including the prototype of calcic-alkali 'metasomatite', the banded feldspar + calc-silicate rocks of the Moonta-Wallaroo Group.

An intrinsic part of the OD model is the REE-U enrichment which was recently attributed to F-rich magmatic fluids (McPhie *et al.* 2011). A granitophile affiliation for the ore fluid at OD was also inferred from the W-Mo-(REE)-signature of U-bearing hematite (Ciobanu *et al.* in press). Moreover, Pb-Pb ages obtained by dating such hematite show that U is introduced early, rather than late, in the alteration sequence. Such discoveries further open the debate about the significance of earlier-still alteration that can track these elements to the root of the main metal source, and whether there is a missing link between magmatism and initiation of hydrothermal activity. Can initiation of hydrothermal activity via albitization be tracked by patterns of REE-U enrichment in IOCG systems?

The present project aims at testing the hypothesis of albitization as a pre-requisite stage for REE-U enrichment in magmatically-derived IOCG systems. If there is such a link,

how would this be expressed across a varied range of lithologies, such as those present in the Moonta-Wallaroo region? Furthermore, do trace element signatures in minerals formed at this stage record the development of key reactions that will ultimately lead to ore deposition? Last, but not least, is there a better, refined IOCG-model that can be applied for local or regional exploration in terranes hosting IOCG deposits?

GEOLOGICAL BACKGROUND

IOCG mineralization and the Olympic Province

The World's largest known concentration of IOCG-style deposits lies in the Olympic Province (Figure 1a), an expansive metallogenic belt which hosts all of the IOCG mineralization in the Eastern Gawler Craton of South Australia (Hayward & Skirrow 2010). This province extends for over 700 km and encompasses many economic IOCG systems including the World-class Olympic Dam deposit (>9,000 Mt of ore; Ehrig *et al.* 2013), Prominent Hill, Carrapateena and Hillside, as well as numerous other prospects (Ferris *et al.* 2002; Skirrow *et al.* 2002, 2007; Hayward & Skirrow 2010). The tectonic history of the Gawler Craton has been documented in detail by Ferris *et al.* (2002), Hand *et al.* (2007) and Reid *et al.* (2008). The Olympic Province comprises Palaeo- and Mesoproterozoic sediments, granites, volcanics and conglomerates (Conor *et al.* 2010; Hayward & Skirrow 2010), underlain by Mesoarchaean to Palaeoproterozoic basement in the west (Ferris *et al.* 2002). Felsic plutonism (Hiltaba Suite), extrusive magmatism (Gawler Range Volcanics), and deposition of Cu-Au mineralization, is considered to be broadly contemporaneous, or to immediately precede, the 1570-1540 Ma Kararan Orogeny (Hand *et al.* 2007; Reid *et al.* 2008; Reid & Hand 2011). Whole-rock geochemical data show enrichment in Light Rare Earth Elements (LREE) within the

felsic and mafic rock packages of the Olympic Province (Hand *et al.* 2007).

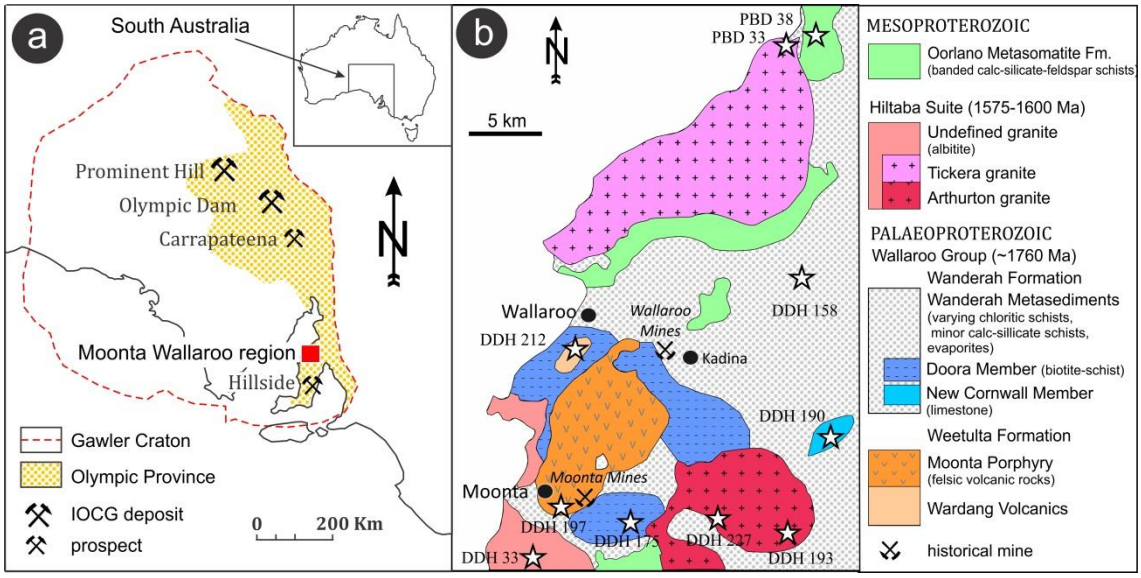

Figure 1 a) Location of Moonta-Wallaroo region and IOCG deposits/prospects within the Olympic Province, Gawler Craton. Inset: Location of South Australia. b) Geological sketch of basement stratigraphy and location of drill hole locations in the Moonta-Wallaroo region (adapted from Conor *et al.* 2010; Forbes 2012).

Geology of the Moonta-Wallaroo region

The Moonta-Wallaroo region, northern Yorke Peninsula, encompasses the Palaeoproterozoic (~1760 Ma) Wallaroo Group and the (~1600-1575 Ma) Mesoproterozoic Hiltaba Suite, both of which are underlain by the Donnington Suite (~1850 Ma). The region is unconformably overlain by incomplete sequences of Neoproterozoic, Cambrian, Permian and Tertiary sediments (Ruano *et al.* 2002; Conor *et al.* 2010).

The Wallaroo Group is a diverse set of siltstone-dominated metasedimentary, felsic and mafic metavolcanic rock packages predominantly defined by the Wanderah and Weetulta Formations (Cowley *et al.* 2003; Conor *et al.* 2010). The Wanderah Formation consists of varying feldspathic, calc-silicate and carbonaceous metasediments of the

Doora and New Cornwall Members, whereas the large rhyodacite Moonta Porphyry Member and Wardang Volcanics Member comprise the Weetulta Formation (Cowley *et al.* 2003).

The Hiltaba Suite encompasses varying felsic granitic (Tickera and Arthurton Granites) and mafic rock packages which are closely associated to regional alkali metasomatism and Cu-Au mineralization (Skirrow *et al.* 2002). Research by Zang *et al.* (2007) has defined both the Tickera and Arthurton Granite as composite batholiths, composed of varying intrusions ranging from monzogranite and granodiorite to tonalite in composition.

Regional alteration, typically metasomatic in character, is widespread throughout the northern Yorke Peninsula. Alteration styles display similar characteristics (strongly oxidised, K-feldspar dominated, brecciation) to those of the Olympic Province (Bastrakov *et al.* 2007; Belpiero *et al.* 2007; Davidson *et al.* 2007), Curnamona Province (Skirrow & Ashley 2000) and Cloncurry district of the Mount Isa Inlier, Queensland (Williams & Pollard 2001). The alteration style in the Moonta-Wallaroo area is typified by sodium- and calcium-rich calc-silicate skarn-like assemblages (Raymond *et al.* 2002; Conor *et al.* 2010). However, this differs from the highly developed magnetite and hematite bodies associated with alteration in the northern Olympic Province (Belpiero & Freeman 2004; Bastrakov *et al.* 2007). Mineral assemblages reflect the high temperatures associated with greenschist to amphibolite-facies metamorphism (Zang *et al.* 2007; Conor *et al.* 2010). Calc-silicate-albite-magnetite and biotite-magnetite-albite are the two dominant alteration assemblages

(Raymond *et al.* 2002; Conor *et al.* 2010), and are always observed to be overprinted by chlorite-quartz-hematite-K-feldspar alteration followed by late argillic alteration (Conor *et al.* 2010). Each of these alteration styles is comprehensively covered by Conor *et al.* (2010).

The concentration of REE and intensity of Cu-Au mineralization is variable depending on alteration assemblage. According to Ferris *et al.* (2002), the Hiltaba Suite is enriched in Rb, Y, Zr, Th and U, and depleted in Ba and Sr. Apatite, monazite, allanite and fluorite in the biotite-magnetite-albite assemblage are also indicative of significant P, REE and F in the hydrothermal fluids (Conor *et al.* 2010). The late chlorite-quartz-hematite-K-feldspar alteration overprint is strongly associated with Cu-mineralization, brecciation and pseudobreccias in the Moonta-Wallaroo area (Raymond *et al.* 2002; Skirrow *et al.* 2007). Isotope dating shows an overlapping age range for all alteration styles, suggesting that they developed within a single regional-scale hydrothermal event, even if the currently available geochronological dataset is not sufficiently accurate to determine the timing of each alteration style (Conor *et al.* 2010).

APPROACH AND METHODOLOGY

A total of 15 drillcore samples previously collected from drillcores in the Moonta-Wallaroo region (Forbes 2012) were studied. These samples (Figure 1, Table 1) are representative of the various lithologies and mineral associations present.

An FEI Quanta 450 scanning electron microscope (SEM) with energy dispersive X-ray spectrometry and back-scatter electron (BSE) imaging capabilities (Adelaide

Microscopy, University of Adelaide; AM-UoA) was used. BSE imaging (accelerating voltage, 20 kV, and beam current of 10 nA) allowed for characterisation of each sample in terms of significant textures and mineralogical relationships, and identification of suitable areas for further microanalysis.

Quantitative compositions of feldspars and accessory minerals within representative samples were determined using a Cameca SX-Five Electron Probe Microanalyser (EPMA) (AM-UoA). Standards, X-ray lines, count times, typical minimum detection limits (mdl) are given in Appendix A.

Laser-Ablation Inductively-Coupled Mass Spectrometry (LA-ICP-MS) was used on selected samples to provide quantitative trace element data (as spot analyses and element maps) for potassium feldspar, albite, rutile, titanite, apatite, zircon and calcite. This was performed on a Resonetics M-50-LR 193-nm Excimer laser microprobe coupled to an Agilent 7700cx Quadrupole ICP-MS (AM-UoA). Full details of the analytical methods for the LA-ICP-MS work are given in Appendix A.

PETROGRAPHY

Three main types of lithologies have been studied: altered magmatic rocks, intensively altered rocks of magmatic origin and metamorphic rocks (Table 1, Figure 1). These lithologies are representative of early regional alkali metasomatism (in particular albitization) in the Moonta area. Key textures and mineral relationships are depicted in Figures 2-5, and compositional data (EPMA) for feldspars, actinolite, epidote, accessory and REE-minerals is presented in Tables 2-7

Table 1: Summary of sample stratigraphy and mineralogy

Sample ID	Stratigraphy	Rock Type	Main Mineralogy			Accessory minerals					Minor/trace minerals	
			Kfs	Ab	Qz	Chl	Ap	Rt	Ttn	Zrc	Other	REEm
227DDH1	Arthurton Granite	Alkali monzogranite	**xx**	**x**	**xx**	**xx**	x	x		x	Hm, Chl	Xn, Bast,
227DDH2	Arthurton Granite	Alkali monzogranite	**xx**	**xx**	**xx**	**x**	x	x		x	Hm, Chl	Xen, Bast,
193DDH1	Arthurton Granite	Alkali monzogranite	**xx**	**x**	**xx**	**xx**		x		x	Hm, Chl	Xen, Mon
33PBD1	Tickera Granite	Variable monzogranite and quartz monzonite	**xx**	**xx**	**x**	**x**	x	x	x	x	Hm, Chl, Cp	Bast, Mon
33PBD2	Tickera Granite	Variable monzogranite and quartz monzonite	**xx**	**xx**	**x**	**x**	x	x		x	Hm, Chl, Cal	Bast, Xen
212DDH1	Wardang Volcanics	Rhyodacite felsic volcanic	**xxx**	**x**	**xx**	**x**	x	x			Hm, Chl	Bast, Mon
212DDH2	Wardang Volcanics	Rhyodacite felsic volcanic	**xxx**	**x**	**xx**	**x**	x	x		x	Hm, Chl	
33DDH1	Undefined Hiltaba Suite	Highly albitised granite (albitite)	**x**	**xxx**	**xx**	**xx**	x	x		x	Hm, Chl	Bast, Xen, Syn
197DDH1	Moonta Porphyry	Highly altered rhyodacite	**xxx**	**x**	**xx**	**xx**	x	x		x	Hm, Chl,	Xen, Mon
175DDH1	Doora Member	Bt-feldspar schist	**xx**	**xx**	**x**	**x**		x			Bt, Mu, Hm, Chl, Mht, Cp	
158DDH1	Wanderah Formation	Chloritic schist	**xx**	**x**	**xx**	**xx**	x	x			Hm, Chl	
190DDH1	New Cornwall Member	Limestone		**x**	**x**	**x**	x				Dol, Chl,	
190DDH2	New Cornwall Member	Limestone		**x**	**x**	**x**	x	x			Dol, Chl,	Bast,
38PBD1	Oorlano Metasomatite	Calc-sillicate feldspar schist	**x**	**xx**	**x**	**x**	x		x		Ep, Act, Hm, Chl, , Cp, Cal	Bast,
38PBD2	Oorlano Metasomatite	Calc-sillicate feldspar schist	**x**	**xx**		**x**	x		x	x	Ep, Act, Hm, Chl, Cp	Mon

Abbreviations: Ab – albite, Act – actinolite, Ap – apatite, Bast – bastnasite, Bt – biotite, Cal – calcite, Chl – chlorite, Cp – chalcopyrite, Dol – dolomite, Ep – epidote, Hm – hematite, Ilm – ilmenite, Kfs – K-feldspar, Mon – monazite, Mht – maghemite, Mt – magnetite, Mu – muscovite, Plag – plagioclase, Rt – rutile, Ser – sericite, Syn – synchisite, Ttn – titanite, Xen – xenotime, Zrc – zircon, REEm – REE minerals. Note on compositions: **xxx** = >50%, **xx** = 20-50%, **x** = 5-20%, x = <5%. Also note: Samples obtained at contact between cover sequences and basement

Main rock types: primary and alteration features

ALTERED MAGMATIC ROCKS

Three types of igneous rocks were studied: two granitoids (Tickera and Arthurton); and a felsic volcanic (rhyodacite; Wardang Volcanics).

The two granitoids, although similar with respect to main mineral assemblages, differ in the intensity of alteration and deformation, as well as in terms of feldspar types and their replacement and alteration textures. Both rocks are coarse-grained and consist of K-feldspar, plagioclase, quartz and chlorite as main components, minor Fe- and Ti-oxides, as well as abundant accessory minerals such as zircon and apatite. Large xenoblastic K-feldspars (>2 mm) commonly display zonation with respect to Ba content, areas of sericitisation and varying porosity (Figure 2a, b). In addition, exsolution lamellae of albite are preserved at various scales within K-feldspar, forming perthitic textures (Figure 2c). However, in the Tickera granitoid, the perthite shows preferentially-oriented lenses of albite within the K-feldspar (Figure 2d), indicating superimposed deformation. Magmatic accessory minerals such as apatite and zircon are clustered around pockets of Fe-Ti-oxides (Figure 2e, f).

Hydrothermal alteration is expressed as three types of mineral associations resulting from replacement of pre-existing minerals within the two granitoids. Firstly, pre-existing feldspars are replaced by widespread albite. The latter is present as large, porous grains (>2 mm), typically proximal to domains of quartz and K-feldspar (Figure 2g). An important difference between the two granitoids is that, although albite is

presently the dominant plagioclase feldspar in both rocks, an intermediate member of the plagioclase series (5.98 wt.% CaO, i.e. andesine; Table 2a) is also present as relicts in the Tickera granitoid (Figure 2h). The hydrothermal nature of the albite can be inferred from similar textures such as porosity in both cases, but in the case of Tickera there are a range of other textures indicating replacement of the andesine by albite + sericite and a new generation of K-feldspar (see albitization textures sub-section).

Secondly, foliation-controlled chlorite + hematite alteration is recognised, in some cases leading to pervasive, intense hematisation (Figure 2i) of pre-existing mafic minerals. Such aspects were previously described by Conor *et al.* (2010) as part of the regional alteration in the area.

Thirdly, primary Fe- and Fe-Ti-oxides have been replaced by hematite (Figure 2e) and symplectites of rutile + chlorite ± hematite (Figure 2f, j). Both these replacement types preserve pre-existing mineral contours indicating pseudomorphism of magnetite and ilmenite, respectively. In the case of the Tickera granitoid, this is further supported by the presence of relict ilmenite within the symplectite areas (Figure 2f). The relatively reduced character of the Tickera relative to Arthurton granitoid can be inferred from the abundant primary ilmenite in the former.

The rhyodacite felsic volcanic (Wardang Volcanics) is predominantly composed of K-feldspar, quartz, minor albite and contains abundant hematite and accessory apatite. This rock has an overall fine-grained to aphanitic texture with porphyritic and flow banding fabrics (Figure 2k). Potassium feldspar aggregates commonly display minor

perthitic textures and varying porosity (Figure 2l). In addition, their grain boundaries are rimmed by hematite. In contrast to the granites, albitization is relatively minor whereas advanced hematisation acts as the prevailing replacement type.

INTENSIVELY ALTERED ROCKS OF MAGMATIC ORIGIN

Two intensively, pervasively altered rocks attributed to magmatic suites, i.e., a granitoid from an undefined Hiltaba suite granite, and a porphyritic felsic volcanic (rhyodacite) attributed to the Moonta Porphyry, were also studied. These are representative of distinct alteration types, i.e., intense albitization and K-feldspar + silicification, respectively. Although relict textures are still recognisable in both rocks, the dominant feldspar within each of them is prominently of hydrothermal origin.

Mainly composed of albite, quartz, K-feldspar and chlorite, and containing abundant accessory minerals clustering Fe-Ti-oxides, this most strongly albitised granitoid (hereafter albitite) has otherwise an overall phaneritic texture and shares similar alteration features with the aforementioned granitoids. Remarkable is that albite shows Ca-enriched, homogenous internal domains surrounded by porous areas with sericite intergrowth (Figure 2m). This feature is similar to relationships between the two plagioclase varieties observed in the Tickera granitoid, however in the albitite, the internal domains contain no more than 1-2 wt.% CaO. This raises the question of whether Ca-enrichment in albite is part of the hydrothermal alteration rather than inherited from a pre-existing Ca-richer plagioclase, as in the Tickera samples.

The highly altered felsic volcanic representing Moonta porphyry is similar to the Wardang Volcanics with respect to the matrix character, i.e., fine-grained, flow banding, and porphyritic texture. The Moonta porphyry, however, features strong silicification, which is seen as layering within the K-feldspar-rich domains (Figure 2n). Secondly, albite is only present in trace amounts, if at all. In both rocks, Fe-oxides, both magnetite and hematite are important components of the alteration, either as dusty inclusions underlining the break-down of mafic minerals to chlorite, or as large, fractured porphyroblasts (Figure 2n). The latter suggest precipitation within strain shadows of larger K-feldspar porphyroblasts. Cores of K-feldspar are surrounded by porous margins with mutual boundaries suggesting inwards-directed corrosion and replacement (Figure 2o).

METAMORPHIC ROCKS

Three banded metamorphic rocks were studied. They all contain feldspars as major components but differ in terms of the other components, i.e. mica, dominantly biotite (Biotite-schist; Doora Member), chlorite (Chlorite-schist; Wanderah Fm.) and actinolite + epidote, (Calc-silicate-schist; Oorlano Metasomatite Formation). Whereas the biotite- and calc-silicate-schists contain both K-feldspar and albite in relatively equal proportions, the latter is very minor in the chlorite-schist. In addition to the three schists, a limestone (New Cornwall Member) with incipient but pervasive dolomitisation and albitization was studied. With the exception of the calc-silicate-schist (Oorlano Metasomatite Fm.), all these rocks are considered to be of sedimentary origin. The pre-metamorphic protolith is not clearly understood for these rocks, which are tied to intrusive contacts in the Moonta-Wallaroo region (Figure 1).

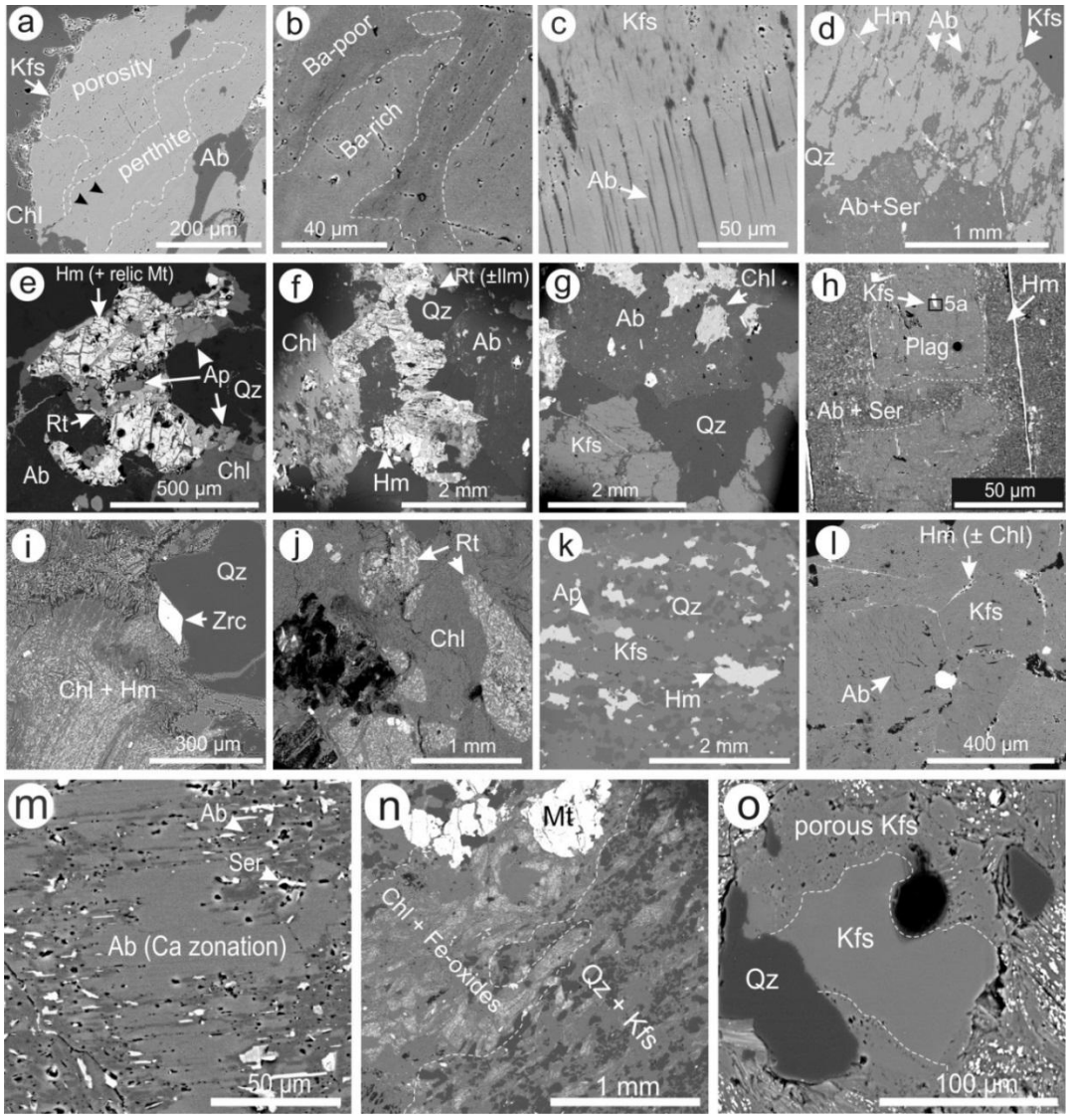

Figure 2: Back-scatter electron (BSE) images showing petrographic aspects of igneous rocks; Arthurton and Tickera granitoids (a-j), felsic rhyodacite Wardang Volcanics (k-l), albitite (m) and Moonta Porphyry rhyodacite (n-o). (a) Perthite texture and varying porosity displayed by K-feldspar. (b) Distinct Ba-zonation within K-feldspar. (c) Detail of perthitic texture showing a domain with albite as lamellar exsolution. (d) Preferentially-oriented albite lenses within K-feldspar suggesting deformation. (e, f) Large aggregates of primary Fe-Ti-oxides replaced by rutile and hematite; note clustering of apatite. (g) Typical mineral association consisting of coarse K-feldspar, albite and quartz. (h) Large relict of plagioclase (andesine) containing small inclusions of K-feldspar and replaced by an intergrowth of albite and sericite. (i) Typical alteration of primary mafic minerals consisting of chlorite and cleavage-oriented hematite; note zircon at the boundary between chlorite and quartz. (j) Typical rutile-chlorite ± hematite symplectites resulting from replacement of primary ilmenite. (k) Porphyritic and flow banding fabric in felsic volcanic. Note abundant hematite and accessory apatite (l) Coarse, perthitic K-feldspar with varying porosity and hematite rims. (m) Internal, Ca-enriched domains within porous albite and preferentially-oriented sericite lamellae. (n) Exemplary texture of Moonta porphyry consisting of domains with quartz + K-feldspar and chlorite + Fe-oxides; note large, fractured porphyroblasts of magnetite. (o) Corroded relict K-feldspar surrounded by an overgrowth of porous K-feldspar. See Table 1 for abbreviations.

The accessory minerals, abundant in the magmatic rocks, vary widely in terms of abundance in the metamorphic rocks. Such minerals are least abundant in the biotite-schist, i.e. occasional, small grains of zircon, or Fe-Ti-oxides. In contrast, apatite is quite abundant and coarse in the chlorite-schist and also to some extent in the limestone. By far the richest in accessory minerals, even richer than the magmatic rocks, is the calc-silicate-schist where titanite and apatite are predominant. As in the case of magmatic rocks, Fe-oxides are also widespread in all cases. The presence of more abundant magnetite can be inferred from grains that are now altered to either maghemite (e.g. in the biotite-schist) or secondary Fe-hydroxides.

The biotite-schist (Figure 3a, b) comprises of fine-medium grained laminated layers of quartz + K-feldspar + albite + biotite ± muscovite ± magnetite (partially oxidised to maghemite). It has an overall porphyroblastic schistose fabric defined by K-feldspar and biotite, respectively. Albite layers are characterised by large, metamorphic magnetite grains and disseminated grains of platy biotite, chlorite and muscovite. Larger biotite and disseminated quartz are interspersed within the K-feldspar layers. In addition, K-feldspar shares some commonalities with the granitoids, i.e. displaying distinct Ba-zonation and, likely metamorphic, perthitic textures (Figure 3c). Alteration is evident with the oxidation of magnetite to maghemite, presence of patchy chlorite textures within albite and the breakdown of ilmenite to rutile.

The chlorite-schist is a medium-grained rock that displays banding by changes in the relative abundance of K-feldspar and quartz (Figure 3d). Furthermore, crosscutting chloritic veins associated with minor albite are also common. Similarly to the biotite-

schist, K-feldspar displays metamorphic textures, particularly porphyroblastic grains (< 200 µm) which frequently vary in porosity and Ba-content, but in this case it exhibits multiple stages of deformation-assisted growth (Figure 3e).

Representing the archetypal lithology of Moonta-Wallaroo banded rocks, the skarn-like calc-silicate-schist (Oorlano Metasomatite) displays remarkable textures and morphologies. These are primarily composed of feldspars, calc-silicates displaying well-defined feldspathic and calc-silicate mineral banding (Figure 3f) and contain abundant titanite and Fe-(Ti)-oxides (Figure 3g). Some of these calc-silicate domains have been superimposed by feldspars and it is in such cases that disequilibrium textures occur between K-feldspar and albite at the finer scale (Figure 3h). Euhedral clinozoisite (Fe/(Fe+Al) ~0.3; Table 3) and acicular actinolite (Fe/(Fe+Mg) 0.3-0.4; Table 3) commonly display internal zonation (Figure 3h, i); the latter also shows fibrous overgrowths.

The limestone unit is fine-grained and porous. Besides calcite, it also comprises minerals such as quartz, dolomite, feldspar (mainly albite) and chlorite (Figure 3j). Variation is seen in terms of grain size, e.g. coarser dolomite-rich parts. Dolomitisation of calcite appears to be part of the chloritic and albite alteration (Figure 3k, l). The albite features patchy domains enriched in Ca (up to 1-2 wt.%), as seen in the albitite above.

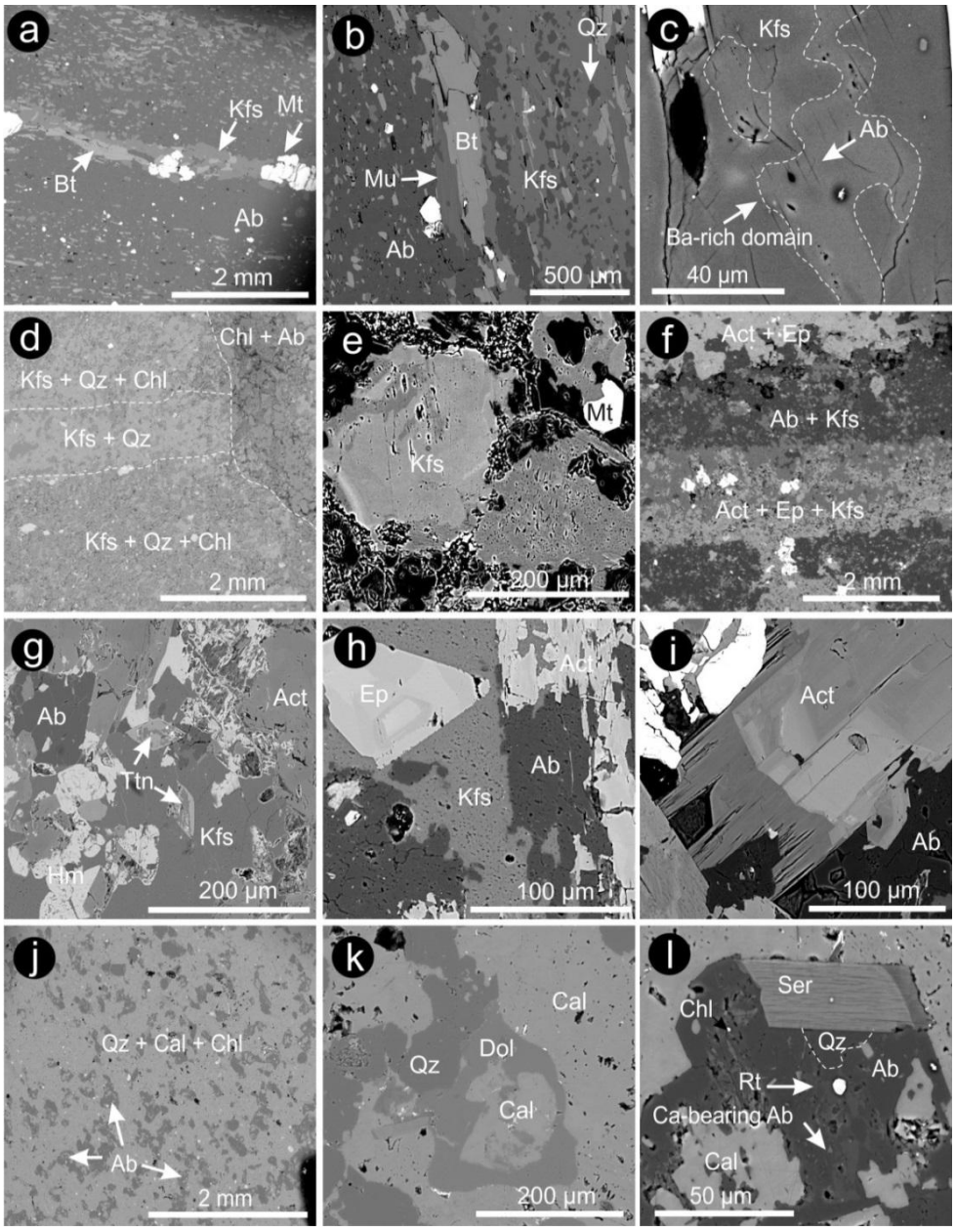

Figure 3: BSE images showing petrographic aspects of metamorphic rocks; biotite-feldspar schist (a-c), chlorite-schist (d-e), calc-silicate schist (f-i) and limestone (j-l). (a, b) Typical banded texture consisting of albite-quartz and K-feldspar with variable proportions of biotite ± muscovite. Note layers with coarser micas and magnetite. (c) Ba-rich domains in K-feldspar. Note the presence of fine albite lamellae (perthite). (d) Quartz + K-feldspar banding within chlorite schist. Note crosscutting albite veinlets. (e) K-feldspar porphyroblast showing corrosion of Ba-rich domains and an overgrowth of porous K-feldspar. (f) Typical texture of the Oorlano Metasomatite showing calc-silicate and feldspathic bands. (g) Abundant, lozenge-shaped titanite and Fe-oxides. (h) Ragged boundaries between K-feldspar and albite suggesting local disequilibrium and replacement between the two. Note oscillatory zoning in adjacent clinozoisite. (i) Actinolite displaying internal zonation and a marginal, acicular Mg-rich rim. (j) Typical spotted texture in limestone consisting of albite + quartz + chlorite within a calcite matrix. (k) Detail showing local dolomitisation of calcite. (l) Detail of albite with Ca-bearing, patchy domains. Note also presence micas. See Table 1 for abbreviations.

Table 2a. Electron probe analytical data for albite

	Arthurton Granite	Tickera Granite	Felsic Volcanic	Albitite	Limeston	Bt-schist	Chl-schist	Calc-silicate schist	Tickera Granite	
	227DDH2	33PBD1	212DDH2	33DDH1	190DDH	175DDH1	158DDH1	38PBD1	33PBD1*	
	(n=5)	(n=4)	(n=5)	(n=5)	(n=9)	(n=5)	(n=8)	(n=15)	Albite	Andesine
F	0.02	0.80	0.07	0.18	0.06	0.05	0.03	0.23		
Na_2O	10.89	9.12	10.89	8.87	10.16	10.54	11.50	10.74	8.75	6.6
SiO_2	67.29	64.44	65.31	73.98	67.54	62.31	68.81	68.84	68.01	61.83
MgO	0.25	0.50	0.03		1.17	0.03		0.07		
Al_2O_3	20.52	22.96	19.62	16.42	20.96	18.27	19.57	20.72	20.79	24.92
P_2O_5	0.03				0.02	0.14	0.02			
Cl		0.19		0.03	0.12	0.02		0.10		
K_2O	0.49	0.90	0.26	0.07	0.29	0.12	0.02	0.11		0.48
CaO	0.16	1.33	0.44	0.17	0.68	0.88	0.04	0.28	1.39	5.98
FeO	0.09	0.26	0.55	0.16	0.33	0.09	0.08	0.47		
Total	**99.72**	**100.51**	**97.20**	**99.88**	**101.35**	**92.46**	**100.07**	**101.55**	**98.94**	**99.81**
									* SEM-EDAX data	
%Ab	96.4	87.3	96.3	98.4	94.7	94.9	99.7	97.9	91.9	66.6
%An	0.8	7.0	2.1	1.1	3.5	4.4	0.2	1.4	8.1	33.4
%KFsp	2.8	5.7	1.5	0.5	1.8	0.7	0.1	0.6		

Table 2b. Electron probe analytical data for K-feldspar

	Arthurton Granite	Tickera Granite	Felsic volcanic		Albitite	Calc-silicate schist
	227DDH2	33PBD1	212DDH2	212DDH1	33DDH1	38PBD1a
	(n=5)	(n=13)	(n=5)	(n=5)	(n=4)	(n=21)
F			0.07	0.31	0.24	0.12
Na_2O	0.76	1.06	0.29	0.31	0.42	0.64
SiO_2	63.24	64.30	61.06	62.46	63.78	63.24
MgO				0.12		0.05
Al_2O_3	17.65	18.28	17.38	17.88	17.90	18.13
Cl	0.05	0.03	0.04	0.03	0.05	0.13
K_2O	15.39	14.68	15.37	15.86	16.17	15.52
CaO	0.03	0.06	0.08	0.54		0.03
TiO_2	0.02		0.02			
FeO	0.04	0.17	0.07	0.25	0.08	0.13
Total	**97.19**	**98.59**	**94.39**	**97.76**	**98.64**	**97.99**
%Ab	7.0	9.9	2.8	2.8	3.8	5.9
%An	0.1	0.3	0.4	2.7	0.0	0.1
%KFsp	92.8	89.8	96.8	94.5	96.2	93.9

Table 3. Electron probe microanalyses of epidote and actinolite

	EPIDOTE			ACTINOLITE						
	38PBD1			38PBD2						
	8	**9**	**10**	**6**	**7**	**8**	**1**	**2**	**3**	**4**
F				0.09	0.23	0.80	0.82	0.39	0.24	0.77
Na_2O	0.05	0.25	0.05	0.15	0.36	0.35	0.84	0.56	0.68	0.62
SiO_2	37.86	34.70	35.66	54.28	55.48	54.02	52.70	54.57	53.77	54.49
MgO	0.01	0.15		12.95	13.09	14.34	13.89	15.77	14.29	15.76
Al_2O_3	22.85	20.46	22.02	0.23	0.72	1.06	2.40	0.99	1.68	0.95
Cl	0.02	0.08	0.16	0.03		0.07	0.10	0.03	0.07	0.03
K_2O				0.04	0.11	0.13	0.25	0.22	0.24	0.23
CaO	23.52	23.10	22.92	12.41	11.58	12.44	11.95	12.12	11.77	11.91
TiO_2						0.05	0.04	0.05	0.10	0.05
FeO				17.91	17.68	15.44	15.51	13.39	15.87	13.47
Fe_2O_3	12.40	12.60	11.61							
MnO	0.09	0.04	0.09	0.21	0.17	0.15	0.16	0.18	0.19	0.20
Total	**96.42**	**91.21**	**92.21**	**98.32**	**99.53**	**98.80**	**98.64**	**98.31**	**98.90**	**98.51**
Calculated formulae (atoms per formula unit)										
Ca	1.992	2.101	2.037	1.949	1.789	1.938	1.872	1.872	1.826	1.843
Na	0.004	0.021	0.004	0.022	0.050	0.050	0.119	0.079	0.095	0.087
K	0.000	0.000	0.000	0.000	0.000	0.000	0.000	0.000	0.000	0.000
Total	**1.996**	**2.121**	**2.041**	**1.971**	**1.838**	**1.987**	**1.991**	**1.951**	**1.921**	**1.930**
Mg	0.001	0.019	0.000	2.829	2.812	3.107	3.025	3.389	3.083	3.393
Fe	0.819	0.894	0.805	2.195	2.132	1.878	1.897	1.615	1.922	1.628
Mn	0.006	0.003	0.006	0.026	0.021	0.018	0.020	0.022	0.023	0.024
Al	2.129	2.047	2.153	0.040	0.122		0.049			
Ti	0.000	0.000	0.000	0.000	0.000	0.011	0.009	0.010	0.022	0.010
Total	**2.955**	**2.963**	**2.964**	**5.091**	**5.087**	**5.014**	**5.000**	**5.037**	**5.051**	**5.056**
Si	2.992	2.946	2.959	7.957	8.002	7.857	7.707	7.869	7.787	7.875
Aliv						0.182	0.365	0.169	0.287	0.163
Total	**2.992**	**2.946**	**2.959**	**7.957**	**8.002**	**8.039**	**8.072**	**8.038**	**8.075**	**8.037**
Fe/(Fe+Mg)				**0.44**	**0.43**	**0.38**	**0.39**	**0.33**	**0.39**	**0.33**
Fe/(Fe+Al)	**0.28**	**0.31**	**0.27**							
F	0.000	0.000	0.000	0.042	0.105	0.369	0.377	0.176	0.111	0.351
Cl	0.003	0.012	0.023	0.007	0.000	0.017	0.024	0.006	0.016	0.007
(OH)	0.997	0.988	0.977	1.951	1.895	1.614	1.598	1.818	1.873	1.643
Total	**1.000**	**1.000**	**1.000**	**2.000**	**2.000**	**2.000**	**2.000**	**2.000**	**2.000**	**2.000**

Accessory and REE-minerals

As mentioned above, all rocks contain variable amounts of accessory minerals (Figure 4). These include, in addition to zircon, apatite, rutile and titanite, REE-minerals (bastnäsite, xenotime, synchysite, monazite), which are widespread in the magmatic rocks and calc-silicate-schist. The occurrence of most observed REE-minerals relates to

hydrothermal overprints accompanying albitization rather than a pre-magmatic or metamorphic origin.

Apatite and zircon are refractory minerals that tend to preserve superimposed alteration as textural overprints, thus serving as a useful tool to better define the overall petrographic context. Apatite is always characterised by chemical zoning observable on back-scatter electron images (BSE). Compositional data indicates fluorapatite throughout all the lithologies (Table 4), with higher F in magmatic relative to metasedimentary rocks, i.e. ~4.5 and ~3.5 wt.%, respectively. EPMA data shows no minor components that would explain the observed zoning; these are instead attributed to REE+Y variation as measured by LA-ICP-MS spot analysis (see next section).

Apatite from all display oscillatory zonation with various patterns from core to rim, e.g. inverse trends in terms of bright/dark shades on BSE images (Figure 4a, b). The magmatic versus hydrothermal core and rim zones, are underlined by porosity, corrosion and changes in the zonation cycle, as well as inwards growth of new apatite (Figure 4a). In the altered volcanic rocks this is further emphasised by reshaping of the oscillatory zoning, porous overgrowths and formation of monazite at the outer margin (Figure 4c). Apatite from the chlorite-schist preserves a history of metamorphic growth (darker rim surrounding an oscillatory-zoned, rounded and deformed core; Figure 4d).

Zircon is only found in significant abundance and size within the two granitoids and albitite. These grains commonly display intense fracturing, metamict cores and oscillatory zoning on BSE images (Figure 4e). Recrystallization of zircon likely took

place during hydrothermal alteration. Compositional data (Table 5) show little variation in terms of Hf (1.2-1.6 wt.% HfO_2) or U content (hundreds to thousands ppm).

Hydrothermal titanite and rutile are typically associated with formation of discrete REE-bearing minerals. Both contain measurable amounts of Nb, Ta, V, REE, and Y (calc-silicate-schist) or U (albitite) (Table 6). Remarkable is the presence of F in both rutile (albitite) and titanite, as well as Sr in the latter.

The calc-silicate-schist is the only host for abundant titanite. It is found that coarser euhedral grains are host to acicular bastnäsite (Figure 4f). Rutile, on the other hand, is abundant throughout almost all lithologies, forming as a pseudomorphic symplectite replacement of Fe-Ti-oxides. Second generation rutile crystallises within vughs accompanied by chlorite + quartz alteration (Figure 4g).

REE-bearing minerals such as xenotime and bastnäsite are frequently associated with rutile (Figure 4h). Xenotime forms contiguous to rutile grains of subangular crystal habit (Figure 4i), while minor acicular bastnäsite forms between aggregates of elongate rutile grains (Figure 4j). In addition, the rutile + chlorite symplectites can also host other REE-minerals, including synchysite-(Ce) which displays stunning oscillatory zoning and thin lamellae of thorite (Figure 4k). Compositional data for both synchysite-(Ce) and bastnäsite-(Ce) are given in (Table 7).

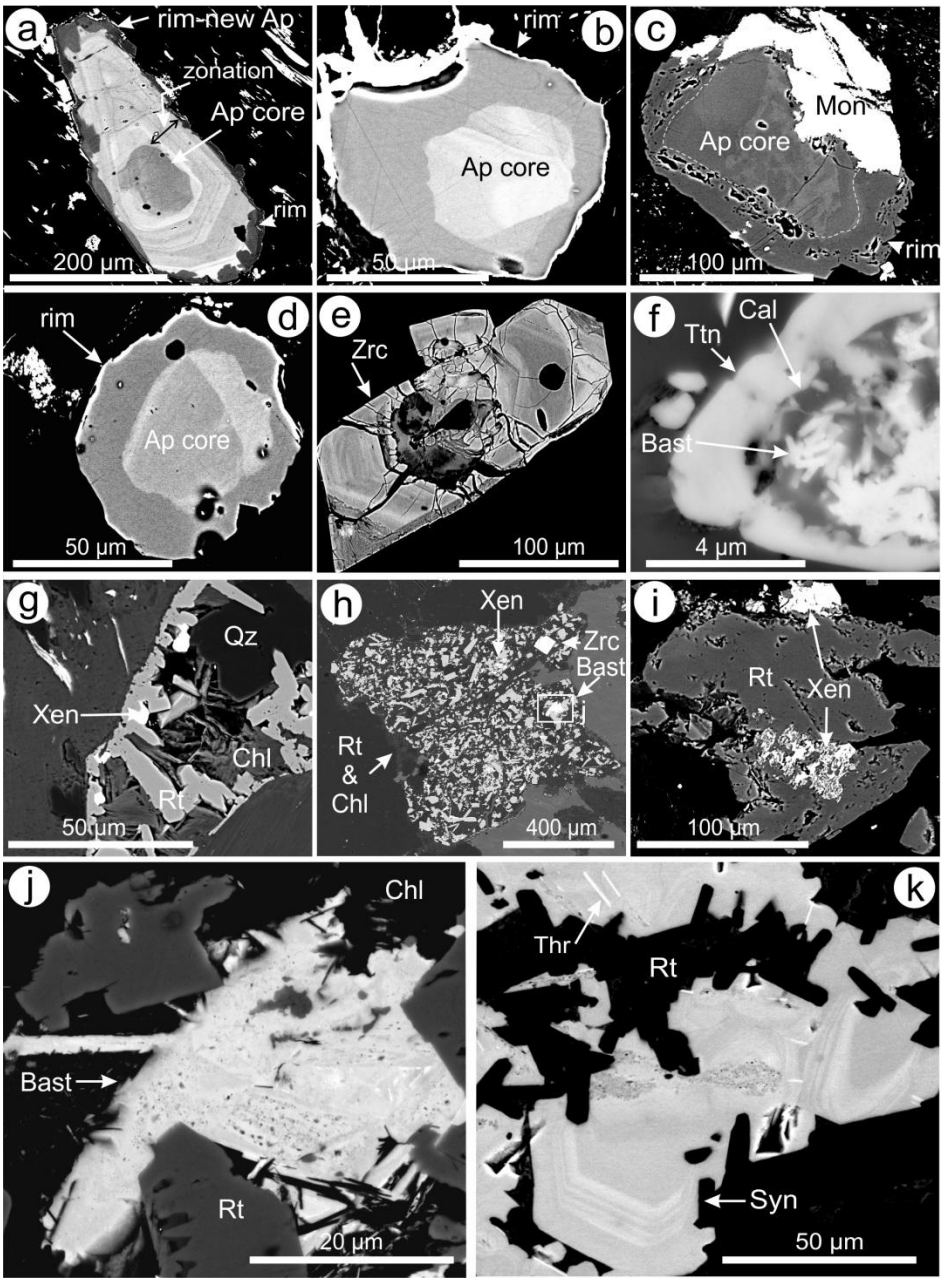

Figure 4: BSE images showing common accessory and REE-minerals; (a-c) Magmatic apatite (bright, REE-rich relict parts) showing hydrothermal overprint (REE-poor dark zones). Note the overprint is expressed as either core-replacement (a) and rims (b, c). Rims can also show porosity and formation of monazite (c). (d) Typical texture of apatite in the chlorite schist showing a rounded, deformed REE-rich core surrounded by a REE-poor rim. (e) Highly fractured, metamict zircon with oscillatory zoning typical of the granitoids. (f) Acicular bastnäsite forming within titanite from calc-silicate schist. (g) Vugh filled with rutile and xenotime in albitite. (h) Pseudomorphic replacement of ilmenite by rutile and chlorite in granitoids. Note abundant REE-minerals (xenotime and bastnäsite) as well as zircon. (i) Xenotime associated with large, corroded rutile in the rhyodacite felsic volcanic. (j) Detail of rutile from (h) showing larger bastnäsite with internal compositional variation. (k) Synchysite displaying stunning oscillatory zoning and thin lamellae of thorite. See Table 1 for abbreviations.

Table 4. Electron probe microanalyses of apatite

	Arthurton granite	Felsic volcanic (Weetula Fm)		Albitite		Calc-silicate schist		Limestone
	227DDH2	212DDH2		33DDH1		38PBD1	38PBD2	190DDH2a
		area 1	area 2	area 1	area 2			
	Mean (n=3)	Mean (n=4)	Mean (n=4)	Mean (n=4)	Mean (n=3)	Mean (n=3)	Mean (n=4)	Mean (n=2)
F	4.55	4.21	5.33	4.48	4.52	3.55	3.62	3.38
Na_2O		0.05	0.05					0.43
MgO								0.04
Al_2O_3	0.03	0.34	0.06				0.04	0.44
SiO_2	0.41	1.14	0.45	0.25	0.18	0.15	0.14	0.81
P_2O_5	42.98	43.24	43.76	43.41	43.45	43.71	43.37	43.83
SO_2	0.07	0.03	0.02	0.05	0.10	0.03	0.06	0.02
Cl	0.05	0.22	0.27	0.05	0.03	0.04	0.01	0.31
K_2O	0.01	0.11	0.03					0.03
CaO	47.41	51.43	52.77	52.65	50.15	47.56	51.43	55.48
TiO_2	0.02	0.03						
MnO		0.04	0.03	0.03		0.03		0.07
FeO	0.76	0.31	0.06	0.09	0.03	0.22	0.07	0.04
SrO	0.04	0.07	0.05	<0.03	0.05	0.05	0.04	<0.03
Y_2O_3	0.15	0.07	0.12	<0.04	0.08	0.06	0.11	
La_2O_3	0.55							
Ce_2O_3	0.47	<0.05	0.20		<0.05	<0.05	<0.05	
Pr_2O_3	0.15	0.11	0.15	0.10	0.14	0.12	0.06	0.09
Nd_2O_3	0.29	0.16	0.27	0.18	0.20	0.19	0.17	0.11
Sm_2O_3								
Eu_2O_3	0.14	0.10	0.10	0.15	0.13	0.13	0.12	0.10
Tb_2O_3			<0.05	<0.04	<0.04	<0.04		
Gd_2O_3				<0.04		<0.04		
Dy_2O_3	0.32	0.25	0.33	0.28	0.28	0.26	0.28	0.30
Total	**98.40**	**101.90**	**104.04**	**101.73**	**99.33**	**96.10**	**99.53**	**105.48**
Calculated formulae (atoms per formula unit)								
Ca	4.465	4.698	4.702	4.826	4.670	4.578	4.842	4.991
Sr	0.002	0.003	0.003	0.000	0.002	0.003	0.002	0.000
Mg	0.000	0.000	0.000	0.000	0.000	0.000	0.000	0.004
Mn	0.000	0.003	0.002	0.002	0.000	0.002	0.000	0.005
Y	0.007	0.003	0.005	0.000	0.004	0.003	0.005	0.000
La	0.018	0.000	0.000	0.000	0.000	0.000	0.000	0.000
Ce	0.015	0.000	0.006	0.000	0.000	0.000	0.000	0.000
Pr	0.005	0.004	0.005	0.003	0.004	0.004	0.002	0.003
Nd	0.009	0.005	0.008	0.005	0.006	0.006	0.005	0.003
Sm	0.000	0.000	0.000	0.000	0.000	0.000	0.000	0.000
Eu	0.004	0.003	0.003	0.004	0.004	0.004	0.004	0.003
Gd	0.000	0.000	0.000	0.000	0.000	0.000	0.000	0.000
Tb	0.000	0.000	0.000	0.000	0.000	0.000	0.000	0.000
Dy	0.009	0.007	0.009	0.008	0.008	0.008	0.008	0.008
Na	0.000	0.008	0.008	0.000	0.000	0.000	0.000	0.070
K	0.001	0.011	0.003	0.000	0.000	0.000	0.000	0.003
Fe	0.050	0.020	0.004	0.006	0.002	0.015	0.005	0.003
Ti	0.001	0.002	0.000	0.000	0.000	0.000	0.000	0.000
Al	0.003	0.034	0.006	0.000	0.000	0.000	0.004	0.043
Total	**4.589**	**4.802**	**4.764**	**4.855**	**4.700**	**4.622**	**4.876**	**5.136**
ΣREY	0.067	0.021	0.036	0.021	0.026	0.024	0.024	0.017
P	3.198	3.121	3.081	3.144	3.197	3.325	3.226	3.115
S	0.006	0.002	0.001	0.004	0.008	0.003	0.005	0.002
Si	0.036	0.097	0.037	0.022	0.016	0.014	0.013	0.068
Total	**3.240**	**3.220**	**3.119**	**3.170**	**3.221**	**3.341**	**3.244**	**3.185**
F	1.264	1.136	1.402	1.212	1.242	1.008	1.005	0.897
Cl	0.008	0.032	0.038	0.007	0.004	0.006	0.002	0.044

* As was consistently below minimum detection limit

Table 5. Electron probe microanalyses of zircon

	Arthurton Granite	Albitite	Calc-silicate schist			
	227DDH24	33DDH15	33PBD11	33PBD12	33PBD13	33PBD14
F		0.99				
Al_2O_3		1.28				
SiO_2	31.99	33.21	29.74	28.88	29.17	31.16
SiO_2	0.02	0.23				0.02
Cl		0.08				
K_2O		1.08				
CaO		0.06				0.03
TiO_2	0.13					0.03
FeO	0.22	1.50	0.17	0.26	0.21	0.47
SrO	0.52	0.49	0.48	0.54	0.50	0.52
Y_2O_3	0.17	0.22	0.12	0.08	0.06	0.40
ZrO_2	66.37	56.69	63.14	63.49	62.69	67.18
Pr_2O_3	0.15	0.12	0.18	0.17	0.16	0.20
Nd_2O_3	0.16	0.16	0.21	0.12	0.12	0.15
Eu_2O_3	0.14	0.16	0.19	0.18	0.12	0.17
Gd_2O_3	0.11					
Tb_2O_3	0.03					
Dy_2O_3	0.46	0.46	0.39	0.39	0.35	0.42
Er_2O_3	0.08					0.14
HfO_2	1.61	1.29	1.46	1.28	1.25	1.34
UO_2	0.04	0.29	0.08			0.11
Total	**102.20**	**97.32**	**96.16**	**95.40**	**94.64**	**102.35**
Calculated formulae (atoms per forumla unit)						
Ca	0.000	0.002	0.000	0.000	0.000	0.001
Sr	0.009	0.009	0.009	0.010	0.010	0.009
Y	0.003	0.003	0.002	0.001	0.001	0.006
Pr	0.002	0.001	0.002	0.002	0.002	0.002
Nd	0.002	0.002	0.002	0.001	0.001	0.002
Eu	0.001	0.002	0.002	0.002	0.001	0.002
Gd	0.001	0.000	0.000	0.000	0.000	0.000
Tb	0.000	0.000	0.000	0.000	0.000	0.000
Dy	0.005	0.005	0.004	0.004	0.004	0.004
Er	0.001	0.000	0.000	0.000	0.000	0.001
U	0.000	0.002	0.001	0.000	0.000	0.001
K	0.000	0.042	0.000	0.000	0.000	0.000
Fe	0.005	0.034	0.004	0.006	0.005	0.011
Ti	0.000	0.000	0.000	0.000	0.000	0.000
Al	0.000	0.046	0.000	0.000	0.000	0.000
Zr	0.989	0.839	1.002	1.019	1.009	1.005
Hf	0.013	0.011	0.013	0.012	0.011	0.011
Total	**1.031**	**0.996**	**1.041**	**1.059**	**1.045**	**1.056**
S	0.001	0.007	0.000	0.000	0.000	0.001
Si	0.978	1.007	0.968	0.951	0.963	0.956
Total	**0.978**	**1.014**	**0.968**	**0.951**	**0.963**	**0.956**
F	0.000	0.095	0.000	0.000	0.000	0.000
Cl	0.000	0.004	0.000	0.000	0.000	0.000

Table 6. Electron probe microanalyses of rutile and titanite

	RUTILE							TITANITE	
	Arthurton granite 227DDH2		Albitite 33DDH1					Calc-silicate schist 38PBD2	
	1	2	7	8	9	10	11	5	6
F			0.39	0.45	0.38	0.44	0.42	1.01	1.08
Na_2O	0.02	0.02	0.01	0.01	0.09	0.03	0.02	0.02	0.02
MgO	0.34		0.01	0.01	0.03	0.13	0.01	0.03	0.04
Al_2O_3	0.13	0.02	0.05	0.06	0.18	0.18	0.10	1.32	1.49
SiO_2	0.28	0.07	0.20	0.27	0.83	0.37	0.26	29.99	30.50
CaO	0.04		0.17	0.19	0.17	0.17	0.15	27.52	28.10
TiO_2	97.09	97.44	96.41	96.86	91.24	95.51	92.13	34.09	34.77
V_2O_3	0.39	0.34	0.33	0.37	0.34	0.44	0.37	0.27	0.27
FeO	1.07	0.74	1.12	0.71	4.08	1.77	3.67	3.02	2.50
SrO								0.12	0.16
Y_2O_3								0.67	0.29
ZrO_2	0.09	0.15			0.07		0.04		
Nb_2O_5	0.56	0.66	0.59	0.38	0.75	0.32	0.29	0.37	0.18
Pr_2O_3	0.09	0.10	0.09	0.10	0.22	0.11	0.11	0.15	0.19
Nd_2O_3	0.18	0.09	0.12	0.19	0.14	0.16	0.18	0.63	0.39
Sm_2O_3	0.06	0.02	0.11		0.01	0.01	0.00	0.14	0.13
Eu_2O_3	0.12	0.17	0.13	0.10	0.18	0.13	0.22	0.19	0.11
Gd_2O_3								0.21	0.08
Tb_2O_3	0.00	0.02		0.04		0.04		0.04	0.04
Dy_2O_3	0.32	0.31	0.34	0.30	0.30	0.34	0.32	0.48	0.36
Ta_2O_5	0.04	0.12							
PbO			0.08		0.11	0.10	0.06		
UO_2					0.32	0.09			
Total	**100.81**	**100.27**	**99.76**	**99.57**	**99.07**	**99.88**	**97.96**	**99.27**	**99.64**
Calculated formulae (atoms per formula unit)									
Ca	0.001	0.000	0.002	0.003	0.003	0.002	0.002	**0.982**	**0.993**
Sr	0.000	0.000	0.000	0.000	0.000	0.000	0.000	0.002	0.003
Mg	0.007	0.000	0.000	0.000	0.001	0.003	0.000	0.001	0.002
Y	0.000	0.000	0.000	0.000	0.000	0.000	0.000	0.012	0.005
Pr	0.000	0.000	0.000	0.000	0.001	0.001	0.001	0.002	0.002
Nd	0.001	0.000	0.001	0.001	0.001	0.001	0.001	0.008	0.005
Sm	0.000	0.000	0.001	0.000	0.000	0.000	0.000	0.002	0.001
Eu	0.001	0.001	0.001	0.000	0.001	0.001	0.001	0.002	0.001
Gd	0.000	0.000	0.000	0.000	0.000	0.000	0.000	0.002	0.001
Tb	0.000	0.000	0.000	0.000	0.000	0.000	0.000	0.000	0.000
Dy	0.001	0.001	0.001	0.001	0.001	0.001	0.001	0.005	0.004
Pb	0.000	0.000	0.000	0.000	0.000	0.000	0.000	0.000	0.000
U	0.000	0.000	0.000	0.000	0.001	0.000	0.000	0.000	0.000
Na	0.001	0.000	0.000	0.000	0.002	0.001	0.000	0.001	0.001
Fe	0.011	0.007	0.011	0.007	0.042	0.018	0.038	0.076	0.062
Ti	0.970	0.979	0.966	0.969	0.931	0.957	0.946	**0.855**	**0.863**
Nb	0.004	0.005	0.004	0.003	0.005	0.002	0.002	0.006	0.003
Ta	0.000	0.000	0.000	0.000	0.000	0.000	0.000	0.000	0.000
Al	0.000	0.000	0.000	0.000	0.000	0.000	0.000	0.000	0.000
Zr	0.001	0.001	0.000	0.000	0.000	0.000	0.000	0.000	0.000
V	0.005	0.004	0.004	0.005	0.004	0.005	0.005	0.008	0.008
Si	0.004	0.001	0.003	0.004	0.011	0.005	0.003	**0.999**	**1.006**
Total	**1.005**	**1.001**	**0.995**	**0.993**	**1.004**	**0.998**	**1.001**	**2.964**	**2.962**
ΣREY	**0.003**	**0.003**	**0.004**	**0.003**	**0.004**	**0.004**	**0.004**	**0.033**	**0.020**
F	0.000	0.000	0.016	0.019	0.016	0.018	0.018	**0.107**	**0.112**

Table 7. Electron probe microanalyses of synchysite-(Ce) and basnasite-(Ce)

	SYNCHYSITE-(CE) Albitite 33 DDH1					BASTNASITE-(CE) Calc-silicate schist 33 PBD1			
	1	**2**	**3**	**5**	**6**	**1**	**2**	**3**	**4**
F	3.37	3.33	3.60	3.19	3.34	6.71	7.51	7.37	8.25
MgO						0.39		0.90	0.35
Al_2O_3						0.29		0.65	0.51
SiO_2	0.04	0.03	0.08	0.07	0.04	0.64	0.42	1.75	4.69
P_2O_5									0.19
SO_2							0.24	0.42	1.92
Cl	0.04	0.04	0.03	0.04	0.04	0.15	0.31	0.12	0.29
CaO	17.99	17.97	17.01	17.87	17.73	4.13	5.03	3.93	4.87
TiO_2	0.23	0.24	1.21	0.20	0.40			0.23	
FeO	0.13		0.45			0.83	0.39	1.90	3.79
As_2O_3						0.04			0.02
Y_2O_3	1.43	1.54	1.59	1.62	1.51	5.17	5.65	5.45	4.36
La_2O_3	10.78	11.54	11.91	10.93	12.30	15.84	14.66	13.12	13.07
Ce_2O_3	24.16	24.48	25.41	24.36	25.35	32.73	31.22	29.42	26.21
Pr_2O_3	2.92	2.73	3.01	2.92	2.75	3.53	3.47	3.45	2.91
Nd_2O_3	10.11	9.72	9.94	10.44	9.29	11.58	12.27	12.38	9.63
Sm_2O_3	1.92	1.83	1.63	1.95	1.53	1.84	2.12	1.93	1.52
Eu_2O_3	0.52	0.43	0.46	0.46	0.40	0.59	0.67	0.65	0.55
Gd_2O_3	1.52	1.43	1.32	1.45	1.14	1.72	2.04	1.95	1.48
Tb_2O_3	0.18	0.17	0.14	0.16	0.14	0.26	0.28	0.25	0.20
Dy_2O_3	0.91	0.92	0.99	0.94	0.96	1.56	1.62	1.58	1.32
Ho_2O_3	0.44	0.49	0.42	0.52	0.41	0.61	0.76	0.71	0.45
Er_2O_3						0.31	0.38	0.34	0.21
Yb_2O_3						0.14	0.14	0.18	0.10
WO_3	0.11	0.01	0.12	0.05	0.09	0.16	0.26	0.17	0.14
PbO						0.06			0.05
ThO_2						1.16	1.86	1.12	0.55
UO_2					0.01	0.10	0.12	0.09	0.06
Total	**76.80**	**76.91**	**79.34**	**77.17**	**77.43**	**90.54**	**91.43**	**90.05**	**87.67**
Calculated formulae (atoms per formula unit)									
Ca	**0.951**	**0.952**	**0.861**	**0.951**	**0.933**	0.183	0.216	0.162	0.182
Mg	0.000	0.000	0.000	0.000	0.000	0.024	0.000	0.052	0.018
Y	0.038	0.041	0.040	0.043	0.040	0.114	0.121	0.112	0.081
La	0.196	0.210	0.208	0.200	0.223	0.242	0.217	0.187	0.168
Ce	**0.436**	**0.443**	**0.439**	**0.443**	**0.456**	**0.496**	**0.459**	**0.416**	**0.335**
Pr	0.052	0.049	0.052	0.053	0.049	0.053	0.051	0.048	0.037
Nd	0.178	0.172	0.168	0.185	0.163	0.171	0.176	0.171	0.120
Sm	0.033	0.031	0.026	0.033	0.026	0.026	0.029	0.026	0.018
Eu	0.009	0.007	0.007	0.008	0.007	0.008	0.009	0.009	0.007
Gd	0.025	0.023	0.021	0.024	0.019	0.024	0.027	0.025	0.017
Tb	0.003	0.003	0.002	0.003	0.002	0.004	0.004	0.003	0.002
Dy	0.014	0.015	0.015	0.015	0.015	0.021	0.021	0.020	0.015
Ho	0.007	0.008	0.006	0.008	0.006	0.008	0.010	0.009	0.005
Er	0.000	0.000	0.000	0.000	0.000	0.004	0.005	0.004	0.002
Yb	0.000	0.000	0.000	0.000	0.000	0.002	0.002	0.002	0.001
Pb	0.000	0.000	0.000	0.000	0.000	0.001	0.000	0.000	0.000
Th	0.000	0.000	0.000	0.000	0.000	0.011	0.017	0.010	0.004
U	0.000	0.000	0.000	0.000	0.000	0.001	0.001	0.001	0.000
Fe	0.005	0.000	0.016	0.000	0.000	0.026	0.012	0.055	0.099
Ti	0.008	0.009	0.043	0.008	0.015	0.000	0.000	0.007	0.000
Al	0.000	0.000	0.000	0.000	0.000	0.014	0.000	0.030	0.021
Total	**1.956**	**1.962**	**1.905**	**1.973**	**1.953**	**1.433**	**1.376**	**1.347**	**1.133**
SREY	**0.992**	**1.002**	**0.985**	**1.015**	**1.006**	**1.173**	**1.130**	**1.031**	**0.808**
P	0.000	0.000	0.000	0.000	0.000	0.000	0.000	0.000	0.006
S	0.000	0.000	0.000	0.000	0.000	0.000	0.009	0.015	0.063
As	0.000	0.000	0.000	0.000	0.000	0.001	0.000	0.000	0.000
Si	0.002	0.002	0.004	0.003	0.002	0.026	0.017	0.067	0.164
W	0.001	0.000	0.002	0.001	0.001	0.002	0.003	0.002	0.001
CO_3	1.996	1.998	1.995	1.996	1.997	0.971	0.971	0.916	0.767
Total	**2.000**	**2.000**	**2.000**	**2.000**	**2.000**	**1.000**	**1.000**	**1.000**	**1.000**
F	1.051	1.041	1.075	1.000	1.036	0.879	0.954	0.899	0.910
Cl	0.004	0.004	0.003	0.003	0.003	0.011	0.021	0.008	0.017
OH						0.111	0.025	0.093	0.073
Total	**1.054**	**1.045**	**1.078**	**1.004**	**1.039**	**1.000**	**1.000**	**1.000**	**1.000**

Key albitization textures

All nine studied rocks show various degrees of albitization. The nature and mineralogy of each plays a role in how albite is expressed texturally, as well as its abundance. A striking aspect is that, although albite formation is the dominant feature, this is accompanied by formation of other minerals at finer scales.

Other minerals are expressed as thin cleavage films or dusty inclusions of sericite ± K-feldspar ± hematite ± REE/U-minerals attached to pores (Figure 5a), as well as regular, cleavage-oriented lamellar intergrowths with dominant sericite (Figure 5b), typical in Arthurton granitoid and felsic volcanic rocks. In the Tickera granitoid, the latter texture is found with variable size and sericite proportion, in particular in areas surrounding replacement of andesine.

There is clear evidence, in the same Tickera granitoid, that albite and new K-feldspar are both formed at this stage. The latter occurs either as irregular, subhedral grains (<20 µm; Figure 5c) or as mesh-domains interspersed with sericite and albite within host albite (Figure 5d, e). Importantly, sub-µm sized REE-minerals are abundant in such meshes.

The same type of sericite-nucleation also surrounds Ca-enriched albite cores (see above) in both albitite and limestone (Figure 5f). Skeletal intergrowths between K-feldspar and albite are clearly post-dated by nucleation of chlorite ± sericite ± titanite in the calc-silicate-schist (Figure 5g). Contrasting with the above, the calc-silicate and biotite-

schists host an extremely fine-grained (<40 µm), granoblastic albite with films of irregular, dusty hematite grains nucleating along grain boundaries (Figure 5h, i).

All these aspects point to the scale of albitization as being a complex phenomenon tied to sub-micron scale mineral reaction/nucleation and an overall chemistry that involves not only Na, but also K, Ca, Fe, all of which scavenge REE and/or U from hydrothermal fluids or from pre-existing minerals.

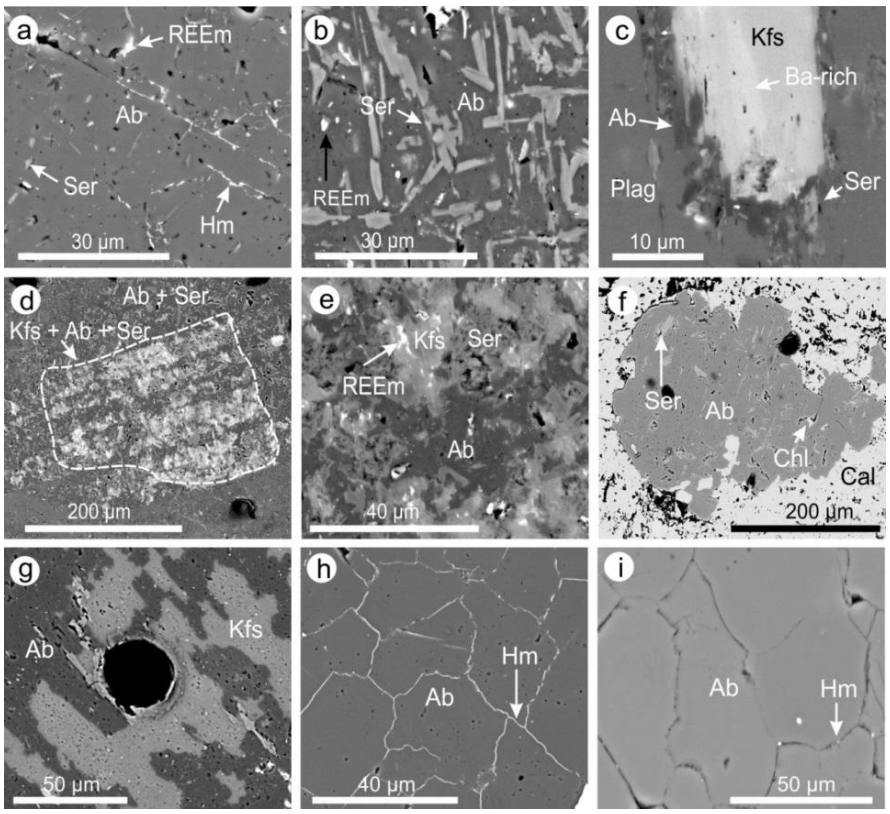

Figure 5: BSE images showing key albitization textures; (a) Arthurton granitoid, (b-e) Tickera granitoid (f) limestone, (g-h) calc-silicate schist and (i) biotite-schist. Typical albite textures showing progressive sericite formation, from scattered (a) to regular lamellar intergrowth with albite (b). Note also presence of minute REE-minerals and hematite. (c) Detail of plagioclase in figure 2h showing an inclusion of K-feldspar rimmed by albite. Note Ba-zonation in the K-feldspar. (d) Domain consisting of new K-feldspar forming mesh texture within albite (e) Detail of K-feldspar in (d) showing abundant, skeletal inclusions of REE-minerals (f) Typical albite in limestone showing patchy Ca-bearing domains and sericite inclusions. (g) Disequilibrium texture between albite and K-feldspar; note high porosity and dusty inclusions of Fe-oxides. (h, i) Fine-grained, granoblastic albite with films and scattered grains of hematite along grain boundaries, respectively. See Table 1 for abbreviations.

TRACE ELEMENT CONCENTRATIONS AND THEIR DISTRIBUTION IN FELDSPAR AND ACCESSORY MINERALS: LA-ICP-MS DATA

Seven minerals within representative samples of host lithologies of the Moonta-Wallaroo IOCG system were analysed by LA-ICP-MS to provide concentrations of rare earth elements and yttrium (hereafter REY) and other trace elements within each mineral (Tables 8-12). Chondrite-normalised REY trends for each mineral and individual time-resolved depth spectra (Figures 6, 7) allow comparative analysis of patterns for each mineral. Ternary and binary plots of large ion lithophile elements (LILE) and incompatible elements are shown for feldspars (Figure 8). In addition, elemental maps of larger feldspars (Figures 9, 10) provide further insight into grain-scale element distributions and partitioning.

For the purpose of constraining and defining the early albitization, the majority of analyses were carried out on feldspar minerals, in this case, the end-members K-feldspar and albite (Tables 2a, b). The REY fractionation trends of these minerals are useful for characterising inherited magmatic and hydrothermal signatures (e.g. as for the Hillside deposit, Yorke Peninsula; Ismail *et al.* in press). Moreover, individual time-resolved depth spectra, showing signal flatness for each element during ablation, allow a first assessment of whether inclusions (possibly at the nanoscale) or elements in solid solution are responsible for incorporation of those elements. However, this can be challenging when dealing with elements at low concentration. In addition to feldspar minerals, accessories such as apatite, titanite, zircon, rutile and calcite were analysed due to their paragenetic importance and ability to host significant amounts of REY.

Apatite is of particular interest as it is present within almost all representative lithologies, as well as rocks from across the Olympic Province.

Trace element distribution: REY trends

POTASSIUM FELDSPAR

Potassium feldspar was analysed in nine samples representing the three groups of lithologies. Their ΣREY mean concentrations is the lowest among the analysed minerals, varying from <1 ppm to tens of ppm in the chlorite-schist and Tickera granitoid, respectively (Table 8a). Three types of reproducible REY fractionation trends are depicted on Figure 6a-c. They are distinguished by differences in REY slope, as well as the size and strength of Eu- and Y-anomalies.

Magmatic signatures

Spot analyses of K-feldspar from altered magmatic rocks (granitoids and felsic volcanics) illustrate a trend characterised by La-enrichment, with a strong downward-sloping trend in the La-Pr interval, and also strong positive Eu-, and negative Y-anomalies (Figure 6a). The trends for different lithologies are, however, distinct from one another in terms of absolute ΣREY concentrations, which span two orders of magnitude (ΣREY = 1-14 ppm, Table 8a). Such trends are consistent with the K-feldspar trend shown by the relatively fresh Hillside granite (HS) in previous studies (Ismail *et al.* in press). Potassium feldspar displays similar textures, i.e. the presence of perthite, zonation with respect to Ba concentration and porosity (Figure 2a-d, k, l), throughout this lithological group. Such textures, except the presence of perthites, are also reported for the Hillside granite (Ismail. *et al.* in press). Importantly, as at Hillside,

REY concentrations in individual spot analyses do not vary relative to the Ba-zoning in the K-feldspar. Based on the similarities outlined above, this trend is attributed to be an inherited magmatic signature in the K-feldspar.

Hydrothermal signatures

Intensively altered rocks of magmatic origin and metasediments show considerably different REY fractionation trends (Figure 6b, c) compared to the altered magmatic rocks. Measured ΣREY concentrations are much lower for these types, ranging from 0.1-4 ppm (Table 8a). These are separated into two types of trends.

Trend type I (Figure 6b), obtained for K-feldspar from the biotite- and chlorite-schists and Moonta porphyry volcanics, is characterised by varying slopes of the La-Pr interval from one rock type to another, but share a gradual, slight HREE-enrichment. This trend is also characterised by a positive Eu-anomaly but with variable height from one rock to another, and no Y-anomaly, an aspect also reported for Moonta-Wallaroo red rock (Ismail *et al.* in press), one of the skarn protoliths at Hillside. In contrast to the granitoids and felsic volcanics, K-feldspar within the chlorite-schist shows a positive correlation between Eu, ΣREY and Ba concentration (Figure 6b).

Trend type II (Figure 6c), obtained for K-feldspar in the calc-silicate-schist, is characterised by slight LREE-depletion relative to the above, and a pronounced negative Y-anomaly. Ismail *et al.* (in press) observe a similar trend in K-feldspar of the Moonta-Wallaroo green-rock. Similarly to trend II, ΣREY concentrations are exceptionally low (<1 ppm). This K-feldspar is found as pervasive alteration in association with albite.

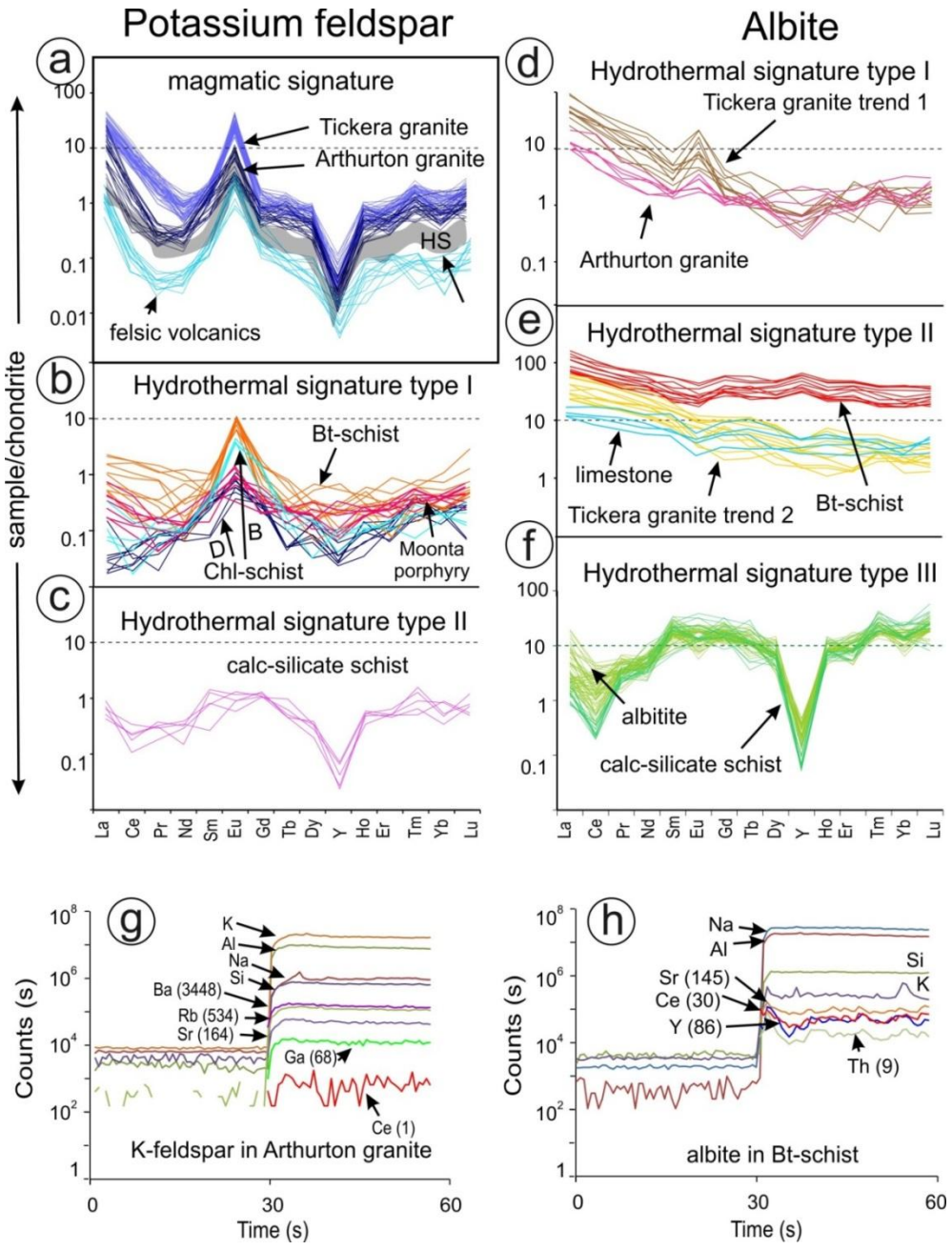

Figure 6: Chondrite-normalised REY plots outlining signatures of K-feldspar (a-c) and albite (d-f) in various lithologies. LA-ICP-MS time-resolved depth spectra for K-feldspar (g) and albite (h) showing representative signal morphologies for trace elements of interest.

HYDROTHERMAL ALBITE

Albite was analysed in seven samples representing the three groups of lithologies.

Unlike K-feldspar, albite shows higher ΣREY, ranging between 14 and 198 ppm (Table 9a). Three types of REY fractionation trends are observed (Figure 6d-f).

Trend type I, obtained from albite within the Arthurton granitoid, and an early generation of albite in the Tickera granitoid (T1), is downwards-sloping and characterised by a positive Eu-anomaly, but of variable size; average ΣREY is 49 and 39 ppm, respectively. This trend was obtained from albite that shows fine-grained intergrowths with sericite ± hematite ± REE-minerals where sericite is far more abundant within albite of the Tickera granitoid (Figure 5a, b). The average concentrations of K within this type of albite are different in the two granitoids: a few wt. %, and thousands of ppm in the Tickera (T1) and Arthurton granitoids, respectively (Table 9b). This is attributed to mixtures, in variable proportions, with sericite (size of intergrowth smaller than LA-ICP-MS spot size).

Trend type II (Figure 6e), representing albite in the biotite-schist, limestone, and a later generation of albite from the Tickera granitoid (T2), is defined by a slight LREE-enrichment, and a relatively flat pattern, with small differences in the slope from one rock type to another. This trend represents albite with highest average ΣREY from the biotite-schist (ΣREY = 198 ppm) and Tickera T2 (ΣREY = 91 ppm); the albite in the limestone is the lowest in average ΣREY (26 ppm). The textures representing trend type II are very different from one another, i.e. homogenous, fine-grained granoblastic in the biotite-schist (Figure 5i), intergrowths with K-feldspar and REE in Tickera T2 (Figure 5d, e) and Ca-richer domains in albite from limestone (Figure 4l).

Trend type III (Figure 6f) represents the albitite and calc-silicate-schist and corresponds to the lowest ΣREY measured in albite (15 and 4 ppm, respectively). The REY fractionation trend shows slight LREE-depletion and negative Ce- and Y-anomalies. As

for trend II, the albite textures differ significantly, i.e. Ca-richer domains and sericite inclusions (Figure 2m) and granoblastic fine-grained aggregates (Figure 5h), respectively.

TIME-RESOLVED DEPTH SPECTRA

Individual time-resolved depth spectra for the K-feldspar in the Arthurton granitoid, as well as the other altered magmatic rocks, show smooth signals for Ba, Rb, Sr and Ga, whereas Ce shows a relatively ragged signal during the ablation interval (Figure 6g). This can be interpreted to indicate the presence of elements in solid solution but discrete REE-minerals as nanoscale inclusions for Ce. Variation in the signal could also be due to the low counts per seconds at sub-ppm concentration values.

Individual time-resolved depth spectra for the REE-rich trend in albite from the biotite-schist (Figure 6h) shows parallel, ragged but relatively low amplitude variations in the signals for Ce, Y and Th during ablation. This may be considered evidence for presence of widespread and pervasively distributed nanoscale inclusions of discrete REE- and/or Th-bearing minerals. As seen however, from the comparable raggedness of the Sr signal on the same figure, an element normally considered to be in solid solution in albite (see Discussion), such a hypothesis needs to be checked by further study of the albite.

Table 8a. Summary of LA-CP-MS data for K-feldspar: REE, Pb, Th and U (ppm)

	Y	La	Ce	Pr	Nd	Sm	Eu	Gd	Tb	Dy	Ho	Er	Tm	Yb	Lu	ΣREY	^{206}Pb	^{207}Pb	^{208}Pb	Th	U
ALTERED MAGMATIC ROCKS																					
Tickera granite 33PBD1, 2																					
Mean (n=49)	0.07	6.4	4.3	0.20	0.37	0.23	1.5	0.21	0.03	0.16	0.03	0.10	0.04	0.16	0.04	14	2.5	2.4	2.4	0.06	0.05
S.D.	0.04	1.8	1.2	0.06	0.12	0.06	0.49	0.07	0.01	0.05	0.01	0.04	0.01	0.06	0.01	3.2	1.1	1.2	1.1	0.03	0.02
Maximum	0.19	11	8.1	0.35	0.74	0.35	2.7	0.36	0.05	0.30	0.06	0.17	0.06	0.28	0.07	22	5.6	5.5	4.8	0.20	0.11
Minumum	0.02	3.4	2.6	0.09	0.20	0.09	0.51	0.10	0.01	0.08	0.02	0.02	0.02	0.07	0.01	8.8	0.71	0.60	0.65	0.03	0.02
Arthurton granite 227DDH2, 193DDH1																					
Mean (n=26)	0.04	2.5	0.78	0.03	0.12	0.16	0.31	0.12	0.02	0.09	0.02	0.07	0.02	0.11	0.02	4.4	3.7	3.8	3.6	0.15	0.03
S.D.	0.02	1.6	0.37	0.01	0.03	0.06	0.16	0.04	0.01	0.03	0.01	0.02	0.01	0.04	0.01	2.0	1.4	1.3	1.1	0.56	0.01
Maximum	0.11	6.3	1.4	0.04	0.19	0.31	0.64	0.21	0.04	0.17	0.04	0.13	0.04	0.26	0.04	9.0	5.9	6.3	5.7	3.0	0.06
Minumum	0.02	0.44	0.21	0.01	0.06	0.08	0.12	0.07	0.01	0.04	0.01	0.04	0.01	0.05	0.01	1.6	0.16	0.57	0.65	0.02	0.02
Felsic Volcanic 212DDH1, 2																					
Mean (n=12)	1.6	0.41	0.15	0.01	0.05	0.04	0.16	0.07	0.01	0.03	0.01	0.03	0.00	0.02	0.01	1.0	0.62	0.54	0.54	0.01	0.02
S.D.	4.3	0.11	0.05	0.00	0.02	0.01	0.06	0.02	0.00	0.02	0.00	0.01	0.00	0.01	0.00	0.16	0.20	0.19	0.21	0.01	0.02
Maximum	16	0.67	0.24	0.01	0.09	0.07	0.25	0.12	0.01	0.06	0.01	0.04	0.01	0.04	0.01	1.3	0.94	0.91	0.88	0.02	0.08
Minumum	0.01	0.22	0.08	0.01	0.03	0.03	0.07	0.04	0.01	0.01	0.01	0.01	0.01	0.01	0.01	0.67	0.32	0.18	0.21	0.01	0.01
INTENSELY ALTERED MAGMATIC ROCKS																					
Moonta Porphyry 197DDH1																					
Mean (n=7)	0.17	0.07	0.10	0.01	0.04	0.05	0.05	0.06	0.01	0.03	0.01	0.03	0.01	0.04	0.01	0.66	1.3	0.68	0.99	0.69	0.31
S.D.	0.13	0.04	0.06	<0.01	0.02	0.02	0.02	0.03	<0.01	0.02	<0.01	0.01	<0.01	0.02	<0.01	0.17	0.48	0.53	0.79	1.47	0.56
Maximum	0.43	0.16	0.22	0.01	0.08	0.07	0.08	0.11	0.01	0.06	0.01	0.04	0.01	0.06	0.02	0.88	2.0	1.9	2.8	4.28	1.68
Minumum	0.02	0.03	0.03	0.01	0.01	0.02	0.02	0.03	0.01	0.01	0.01	0.01	0.01	0.01	0.01	0.46	0.67	0.32	0.36	0.02	0.03
METASEDIMENTS																					
Biotite-feldspar schist 175DDH1																					
Mean (n=12)	0.33	0.19	0.35	0.04	0.13	0.06	0.55	0.13	0.01	0.05	0.01	0.04	0.01	0.07	0.02	2.0	4.9	3.8	4.9	0.15	0.11
S.D.	0.35	0.12	0.29	0.03	0.13	0.03	0.11	0.07	0.01	0.04	0.01	0.05	0.01	0.10	0.02	0.69	1.1	0.85	1.0	0.21	0.08
Maximum	1.3	0.44	0.83	0.10	0.41	0.12	0.67	0.27	0.02	0.14	0.05	0.17	0.03	0.37	0.06	3.1	6.3	5.2	6.2	0.83	0.27
Minumum	0.05	0.07	0.05	<0.01	<0.01	<0.01	0.35	0.04	<0.01	<0.01	0.01	<0.01	<0.01	<0.01	<0.01	1.0	3.4	2.5	3.1	0.02	0.02
Chlorite-schist B 158DDH1 (Ba-bearing)																					
Mean (n=4)	0.12	0.03	0.04	0.01	0.01	0.05	0.19	0.22	0.01	0.03	0.01	0.02	<0.01	0.02	<0.01	0.76	7.0	6.0	6.4	0.13	0.02
S.D.	0.04	0.02	0.03	0.01	0.02	0.01	0.03	0.07	<0.01	0.01	<0.01	0.01	<0.01	0.01	<0.01	0.15	0.80	0.77	1.2	0.08	0.01
Maximum	0.17	0.08	0.09	0.02	0.04	0.06	0.23	0.27	0.01	0.04	0.01	0.02	0.01	0.03	0.01	0.97	8.1	7.0	8.4	0.25	0.04
Minumum	0.06	0.02	0.01	<0.01	<0.01	0.04	0.15	0.10	<0.01	0.01	0.01	<0.01	<0.01	<0.01	<0.01	0.55	6.0	5.2	5.5	0.04	0.01
Chlorite-schist D 158DDH1																					
Mean (n=8)	0.05	0.01	0.02	0.01	0.04	0.03	0.04	0.06	0.00	0.02	<0.01	0.02	0.01	0.02	0.01	0.33	2.2	1.4	1.6	0.05	0.05
S.D.	0.02	0.01	0.01	<0.01	0.02	0.02	0.01	0.01	<0.01	0.01	<0.01	<0.01	<0.01	0.02	<0.01	0.05	0.56	0.46	0.42	0.07	0.06
Maximum	0.09	0.03	0.03	0.01	0.05	0.05	0.06	0.08	0.01	0.04	0.01	0.02	0.01	0.04	0.01	0.39	3.1	2.2	2.4	0.21	0.21
Minumum	0.04	<0.01	0.01	<0.01	<0.01	<0.01	0.02	0.04	<0.01	0.01	<0.01	0.01	<0.01	<0.01	<0.01	0.25	1.5	0.86	1.1	<0.01	<0.01
Calc-silicate schist 38PBD1																					
Mean (n=5)	0.07	0.15	0.13	0.03	0.14	0.14	0.06	0.23	0.02	0.08	0.03	0.08	0.03	0.10	0.02	1.3	0.56	0.56	0.68	0.04	0.02
S.D.	0.03	0.04	0.05	0.01	0.04	0.06	0.01	0.02	0.01	0.02	<0.01	0.02	0.01	0.04	0.01	0.12	0.33	0.23	0.34	0.01	0.01
Maximum	0.11	0.22	0.21	0.04	0.18	0.22	0.08	0.27	0.04	0.10	0.03	0.10	0.04	0.15	0.03	1.5	1.2	0.85	1.1	0.06	0.04
Minumum	0.04	0.10	0.06	0.02	0.07	0.04	0.03	0.21	0.02	0.05	0.02	0.04	0.01	0.06	0.01	1.2	0.24	0.18	0.25	0.03	<0.01

Table 8b. Summary of LA-CP-MS data for K-feldspar: other elements (ppm)

	Na	Mg	P	Ca	Sc	Ti	Mn	Fe	Cu	Zn	Ga	Rb	Sr	Zr	Cs	Ba	Ta
ALTERED MAGMATIC ROCKS																	
Tickera granite 33PBD1																	
Mean (n=49)	6745	45	14	729	2.6	80	20	931	-	3.7	39	595	127	0.27	1.2	1302	-
S.D.	3261	164	3.9	410	1.1	21	22	690	-	9.5	6.4	51	35	0.81	0.24	411	-
Maximum	#####	880	26	2971	6.1	154	122	5220	-	68	56	719	249	5.7	1.9	2324	-
Minumum	2909	0.45	8.7	272	0.96	41	0.63	525	-	0.61	31	483	42	0.02	0.80	788	-
Arthurton granite 193DDH1																	
Mean (n=26)	5029	4.7	9.7	375	1.2	49	15	483	-	2.2	66	512	183	0.08	2.8	3287	-
S.D.	2194	7.2	4.1	111	0.15	40	21	203	-	1.8	5.4	25	57	0.12	0.58	416	-
Maximum	#####	31	19	575	1.6	147	101	1053	-	9.1	76	566	264	0.62	3.5	4139	-
Minumum	2483	0.46	5.5	220	0.96	15	1.4	225	-	0.93	53	466	28	0.01	0.38	2525	-
Felsic Volcanic 212DDH1																	
Mean (n=12)	2964	6.1	11	463	1.8	54	4.5	813	-	1.7	127	359	162	0.05	0.91	3868	0.08
S.D.	514	11	3.2	99	0.18	73	5.0	1417	-	1.5	7.1	17	42	0.02	0.07	169	0.07
Maximum	4070	43	18	575	2.1	295	18	5468	-	5.0	138	394	215	0.08	1.1	4093	0.36
Minumum	2221	0.74	5.1	248	1.5	16	0.30	177	-	0.69	118	335	80	0.02	0.82	3540	0.01
INTENSELY ALTERED MAGMATIC ROCKS																	
Moonta Porphyry 197DDH1																	
Mean (n=7)	2529	401	8.8	382	1.7	95	6.4	1421	38	3.0	90	333	45	2.5	1.3	2723	0.19
S.D.	693	474	3.4	194	0.22	147	4.2	981	46	2.0	27	37	27	3.5	0.39	888	0.14
Maximum	3784	1416	17	819	2.0	439	14	3442	136	6.2	124	370	88	9.6	1.8	3827	0.46
Minumum	1827	29	6.1	208	1.3	8.5	2.0	427	4.2	0.83	34	266	9.0	0.01	0.74	946	0.03
METASEDIMENTS																	
Biotite-feldspar schist 175DDH1																	
Mean (n=12)	5818	105	690	504	1.9	46	2.3	1766	3.6	2.7	120	308	180	12	1.4	4246	0.07
S.D.	1591	157	499	80	0.38	57	1.8	1992	2.4	1.9	7.5	24	46	20	0.23	289	0.07
Maximum	#####	602	1300	673	3.0	228	7.1	6829	7.2	6.8	139	352	248	51	1.9	5001	0.31
Minumum	4115	3.4	73	371	1.4	12	0.54	166	0.36	0.86	110	265	107	0.05	0.94	3897	0.02
Chlorite-schist B 158DDH1 (Ba-bearing)																	
Mean (n=4)	4621	2758	9.1	722	6.3	59	104	3051	16	14	284	313	114	1.4	0.88	5233	0.08
S.D.	2721	4322	3.0	106	1.1	44	156	4220	15	13	31	62	21	0.76	0.16	496	0.00
Maximum	7969	10242	12	884	7.6	114	375	9608	41	33	328	401	135	2.5	1.1	5898	0.09
Minumum	1829	153	5.5	622	5.0	8.5	6.1	495	3.4	2.0	241	228	90	0.55	0.68	4516	0.08
Chlorite-schist D 158DDH1																	
Mean (n=8)	2062	1714	7.2	423	5.2	33	78	2397	13	4.5	50	537	22	0.72	0.90	930	0.07
S.D.	1454	1952	2.5	43	0.43	63	81	2255	12	3.1	6.4	57	5.8	0.70	0.31	111	0.03
Maximum	5826	4910	12	506	6.1	199	208	6553	32	9.6	63	630	32	2.0	1.5	1064	0.13
Minumum	1195	19	3.0	374	4.6	4.0	5.0	251	1.9	1.7	40	444	14	0.12	0.49	762	0.04
Calc-silicate schist 38PBD1																	
Mean (n=5)	3455	18	11	284	1.6	3.5	7.9	748	2.3	1.1	33	754	8.7	0.06	0.71	1001	0.06
S.D.	2480	4.6	2.1	121	0.24	0.91	6.1	151	2.6	0.66	5.6	72	3.7	0.03	0.22	205	0.02
Maximum	7580	24	15	500	2.0	5.2	18	958	7.6	2.5	43	862	15	0.10	0.95	1353	0.09
Minumum	1282	11	8.5	183	1.3	2.7	2.9	529	0.69	0.66	28	661	3.9	0.03	0.37	812	0.03

Table 9a. Summary of LA-CP-MS data for albite: REE, Pb, Th and U (ppm)

	Y	La	Ce	Pr	Nd	Sm	Eu	Gd	Tb	Dy	Ho	Er	Tm	Yb	Lu	ΣREY	^{206}Pb	^{207}Pb	^{208}Pb	Th	U
ALTERED MAGMATIC ROCKS																					
Tickera T1 33PBD1																					
Mean (n=10)	1.1	13	17	1.4	4.3	0.60	0.63	0.47	0.06	0.25	0.06	0.20	0.04	0.20	0.04	39	1.7	0.53	1.2	0.07	0.10
S.D.	0.64	4.9	6.0	0.64	2.1	0.28	0.34	0.18	0.03	0.14	0.02	0.10	0.01	0.07	0.01	14	0.67	0.17	0.48	0.02	0.06
Maximum	2.9	22	28	2.7	8.5	1.3	1.2	0.86	0.14	0.56	0.11	0.42	0.07	0.33	0.05	65	2.9	0.80	2.0	0.11	0.26
Minimum	0.44	6.0	7.9	0.54	1.8	0.23	0.24	0.27	0.03	0.10	0.04	0.08	0.01	0.11	0.02	19	0.80	0.29	0.46	0.04	0.04
Tickera T2 33PBD1																					
Mean (n=11)	4.9	20	39	4.3	15	2.9	0.56	1.9	0.30	1.5	0.22	0.48	0.09	0.39	0.06	91	2.1	0.64	1.4	0.28	0.12
S.D.	2.2	9.2	19	1.9	6.4	1.1	0.27	0.94	0.18	0.86	0.16	0.29	0.04	0.19	0.02	42	1.5	0.42	0.88	0.37	0.07
Maximum	8.4	36	77	8.2	30	5.2	1.0	3.4	0.61	2.8	0.53	1.1	0.17	0.76	0.10	174	6.8	1.8	3.6	1.3	0.28
Minimum	1.9	10	18	2.2	7.6	1.4	0.20	0.37	0.07	0.36	0.04	0.16	0.04	0.15	0.03	43	0.71	0.26	0.43	0.03	0.06
Arthurton 227DDH2																					
Mean (n=6)	0.73	3.6	5.5	0.28	0.82	0.14	0.10	0.13	0.03	0.12	0.04	0.10	0.03	0.16	0.03	49	1.1	0.84	1.1	0.86	0.35
S.D.	0.74	1.4	3.9	0.12	0.31	0.02	0.03	0.02	0.01	0.06	0.02	0.04	0.01	0.11	0.01	18	0.49	0.35	0.56	0.76	0.26
Maximum	2.3	6.6	14	0.52	1.3	0.17	0.15	0.17	0.04	0.24	0.08	0.20	0.05	0.40	0.06	88	2.0	1.4	1.8	2.0	0.91
Minimum	0.14	2.4	2.3	0.16	0.43	0.10	0.06	0.11	0.02	0.07	0.02	0.06	0.01	0.08	0.02	32	0.66	0.47	0.51	0.06	0.14
INTENSELY ALTERED MAGMATIC ROCKS																					
Albitite 33DDH1																					
Mean (n=66)	0.42	1.1	1.1	0.36	2.4	2.7	0.78	3.3	0.43	1.8	0.47	1.6	0.50	2.2	0.54	15	3.8	3.5	2.4	0.79	0.78
S.D.	0.15	0.96	0.69	0.12	0.64	0.86	0.26	0.81	0.12	0.60	0.12	0.47	0.13	0.53	0.17	3.0	1.5	1.1	1.9	0.25	0.43
Maximum	0.75	4.6	3.0	0.64	4.5	5.1	1.4	5.5	0.80	3.7	0.74	2.8	0.98	3.5	1.1	24	7.9	6.9	10	1.5	2.5
Minimum	0.15	0.27	0.21	0.13	1.1	1.3	0.32	2.1	0.21	0.77	0.25	0.71	0.34	1.0	0.26	10	1.7	1.7	0.51	0.29	0.29
METASEDIMENTS																					
Bt-Fds schist 175DDH1																					
Mean (n=12)	69	23	43	5.0	21	5.0	1.5	7.8	1.3	8.2	1.8	5.4	0.67	4.2	0.66	198	2.9	1.1	2.2	11	1.9
S.D.	20	7.2	12	1.4	5.4	1.7	0.46	2.0	0.36	2.3	0.52	1.5	0.21	1.4	0.17	50	0.70	0.48	0.45	3.2	0.55
Maximum	103	38	66	7.3	31	8.2	2.5	12	2.1	12	2.7	7.7	1.00	6.5	0.96	288	4.0	2.3	3.0	16	3.2
Minimum	48	16	30	3.3	13	3.0	0.97	5.3	0.83	5.8	1.2	3.5	0.43	2.7	0.43	138	2.0	0.74	1.6	7.4	1.2
Calc-silicate schist 38PBD2																					
Mean (n=16)	0.31	0.46	0.30	0.23	1.9	2.1	0.74	2.7	0.34	1.1	0.37	0.97	0.32	2.0	0.44	14	4.5	3.7	2.9	2.2	1.5
S.D.	0.23	0.17	0.22	0.16	1.3	1.00	0.44	0.94	0.22	0.92	0.20	0.69	0.27	1.1	0.23	2.8	2.6	0.98	1.9	2.1	0.94
Maximum	0.97	0.80	0.64	0.47	4.5	3.5	1.5	4.4	0.77	2.4	0.70	2.0	0.71	3.2	0.87	20	11	6.4	8.8	7.3	4.1
Minimum	0.00	0.00	0.00	0.00	0.00	0.00	0.00	0.00	0.00	0.00	0.00	0.00	0.00	0.00	0.00	10	2.0	2.2	1.1	0.00	0.51
Limestone 190DDH2a																					
Mean (n=4)	4.3	3.6	8.2	1.1	3.8	1.1	0.18	1.0	0.21	0.95	0.17	0.45	0.06	0.31	0.07	26	1.4	0.65	0.72	2.0	1.6
S.D.	1.3	0.76	2.9	0.44	1.5	0.57	0.07	0.47	0.11	0.46	0.06	0.14	0.02	0.06	0.02	8.5	0.18	0.15	0.13	0.92	0.97
Maximum	5.7	4.8	13	1.7	6.2	2.1	0.28	1.8	0.38	1.6	0.25	0.59	0.09	0.38	0.10	39	1.7	0.84	0.82	3.6	3.2
Minimum	2.6	2.9	4.9	0.57	2.2	0.64	0.08	0.46	0.08	0.51	0.09	0.24	0.04	0.24	0.04	16	1.2	0.45	0.51	1.2	0.66

Table 9b. Summary of LA-CP-MS data for albite: other elements (ppm)

	Mg	P	K	Ca	Sc	Ti	V	Mn	Fe	Cu	Zn	Ga	Rb	Sr	Zr	Nb	Sn	Cs	Ba
ALTERED MAGMATIC ROCKS																			
Tickera T1 33PBD1																			
Mean (n=10)	2339	15	22517	4966	2.7	67	5.7	101	6360	1.6	8.2	29	363	105	0.21	0.06	0.46	1.4	156
S.D.	819	3.9	3014	1653	0.87	29	1.9	22	933	1.7	1.9	3.0	81	25	0.21	0.04	0.24	0.41	58
Maximum	3587	21	27301	8732	4.7	137	8.5	150	7965	6.7	12	33	497	165	0.70	0.18	0.99	2.3	314
Minimum	1433	11	15809	2777	1.8	32	2.2	80	5061	0.77	5.6	24	212	80	0.05	0.01	0.19	0.98	109
Tickera T2 33PBD1																			
Mean (n=11)	2087	41	23266	4560	3.9	82	9.4	88	6367	2.2	8.1	30	414	104	0.45	0.15	1.2	1.8	279
S.D.	1061	28	3458	3505	1.2	33	5.2	21	967	1.9	4.0	4.5	107	66	0.73	0.14	0.98	0.65	168
Maximum	4976	91	27374	11719	5.8	152	17	133	8345	7.2	19	38	616	211	2.7	0.45	3.6	2.8	693
Minimum	930	10	16410	1164	2.6	22	1.6	64	4920	0.70	2.7	22	242	41	0.05	0.03	0.10	0.90	149
Arthurton 227DDH2																			
Mean (n=6)	1048	8.8	3188	3385	5.0	12	8.5	30	3398	4.3	2.3	13	20	44	1.6	0.09	0.67	0.25	26
S.D.	1909	3.5	1927	2341	5.0	8.6	11	23	3039	2.9	2.5	2.6	8.3	6.2	1.8	0.10	0.77	0.19	8.5
Maximum	5311	16	6610	8373	15	30	32	78	8760	9.2	7.9	16	29	56	5.1	0.29	2.0	0.59	35
Minimum	109	5.6	1234	1749	1.5	5.2	1.1	11	761	1.1	0.78	9.9	8.5	37	0.06	0.02	0.08	0.11	14
INTENSELY ALTERED MAGMATIC ROCKS																			
Albitite 33DDH1																			
Mean (n=66)	647	61	9509	4203	2.7	32	1.1	47	2901	5.1	8.1	30	105	80	1.9	0.48	1.9	0.64	67
S.D.	899	8.6	5074	2225	1.1	89	0.78	24	1700	2.2	4.0	6.2	73	32	3.7	0.68	0.72	0.62	60
Maximum	7264	91	27908	10213	6.4	742	3.1	101	9771	14	20	49	309	148	28	4.7	4.7	4.7	346
Minimum	21	47	1784	1138	1.7	6.8	0.29	4.6	345	2.8	2.9	17	4.4	28	0.36	0.16	0.95	0.22	9.8
METASEDIMENTS																			
Bt-Fds schist 175DDH1																			
Mean (n=12)	481	371	2742	6085	3.6	267	4.6	8.4	2364	14	6.7	16	14	174	51	0.65	<mdl	0.20	63
S.D.	714	67	2325	266	1.2	451	4.9	9.8	2393	5.4	2.6	2.8	14	35	48	1.1	<mdl	0.28	85
Maximum	2514	535	9084	6478	6.5	1709	16	35	9635	27	14	22	50	262	154	4.2	<mdl	1.1	341
Minimum	27	274	717	5647	2.6	10	1.2	1.3	1001	7.3	4.1	13	2.0	139	7.2	0.07	<mdl	0.01	15
Calc-silicate schist 38PBD2																			
Mean (n=16)	196	63	478	1470	4.0	22	2.6	14	3444	<mdl	<mdl	27	3.0	7.9	3.4	<mdl	<mdl	<mdl	6.6
S.D.	180	13	96	552	1.6	12	4.4	8.0	3638	<mdl	<mdl	4.6	2.2	4.3	3.3	<mdl	<mdl	<mdl	3.5
Maximum	750	90	545	3174	7.4	51	19	31	16229	<mdl	<mdl	39	8.5	21	13	<mdl	<mdl	<mdl	14
Minimum	5.9	47	131	938	1.8	11	0.41	2.9	500	<mdl	<mdl	20	0.67	4.8	0.00	<mdl	<mdl	<mdl	0.00
Limestone 190DDH2a																			
Mean (n=4)	8588	13	8204	50082*	3.0	297	11	942	5838	25	5.7	18	51	46	36	0.42	<mdl	1.7	133
S.D.	5383	0.99	6445	25113	0.45	459	7.1	397	3496	13	2.0	3.7	53	28	16	0.49	<mdl	2.6	122
Maximum	15476	14	19345	74305*	3.5	1092	22	1278	10245	46	7.9	25	143	94	57	1.3	<mdl	6.2	339
Minimum	627	11	3829	10172	2.4	8.0	1.8	278	677	11	2.5	16	15	26	15	0.05	<mdl	0.22	25

* These high concentrations could not be confirmed by SEM-EDAX - mixture with calcite at the scale of the LA-ICP-MS spot is suspected

ACCESSORY MINERALS

Analysis of apatite shows two distinct REY fractionation trends. A downwards-sloping trend is representative of all rock types except the Moonta porphyry and T2 trends from the Arthurton granitoid (Figure 7a-d). All analysed apatite displays a negative Eu-anomaly. Measured ΣREY concentrations differ in the different lithologies: from up to 1-2 wt.% in the granitoids to thousands of ppm in all the others, except the limestone (~500 ppm) (Table 10a). The Arthurton granitoid (Figure 7b) shows variation with progressive alteration from magmatic cores (T1) to rims (T2), with a marked decrease of ΣREY (1.7 wt.% to 620 ppm) and change from downwards-sloping to upwards-sloping. Similarly, the felsic volcanic shows a change in the slope with alteration (Figure 7c). In the Moonta porphyry (Figure 7d), the pattern is flat but with a distinct, upwards-sloping REY fractionation trend with alteration.

Zircon analyses from the two granitoids and albitite (Table 11) show REY fractionation trends dominated by a positive Ce-anomaly, negative Eu-anomaly and HREE-enrichment (Figure 7e). All zircons are highly fractured with varying degrees of zonation. Measured ΣREY concentrations are lower than that in apatite: up to 7000 ppm for the Tickera granitoid, 3300 ppm in the Arthurton granitoid and 2900 ppm in albitite. In addition, the dataset for zircon shows a positive correlation between U (hundreds of ppm) and ΣREY.

REY fractionation trends for (hydrothermal) rutile in the felsic volcanic and Moonta porphyry show an upwards-sloping pattern (Figure 7f). Measured ΣREY concentrations

are 200 and 280 ppm, respectively, still lower than zircon and apatite. Both datasets consistently show >7000 ppm Nb, and up to 1000 ppm Ta (Table 12).

ΣREY concentrations in titanite from the calc-silicate-schist are significantly higher (1.5 wt.%, Table 12) than rutile. This mineral displays a flat, slightly downwards-sloping REY fractionation trend with negative Eu-anomaly (Figure 7g).

Data for vein calcite from the Tickera granitoid and calc-silicate-schist indicate the carbonate to be a significant LREE host (Table 12). Concentrations of Fe, Mn, Mg and Sr are also high. Calcite in the calc-silicate-schist has a mean ΣREY concentration exceeding 3000 ppm, whereas it is an order of magnitude lower in veinlets from the Tickera granitoid. Representative REY fractionation trends (Figure 7h) are downwards-sloping and more pronounced in the calc-silicate-schist.

Other trace elements within feldspar

A ternary Rb-Ba-(Sr*10) plot separates analysed K-feldspars into clusters characterising the three main lithologies (Figure 8a). The granitoids and Moonta porphyry group towards the Ba-Sr edge, contrasting markedly with the granite at Hillside (Ismail *et al.* in press) which plots in the centre of the diagram. Interestingly, the biotite-schist also plots close to the Ba-Sr edge. The other metasediments form clusters closer to the Rb-Ba edge. Ba-rich K-feldspar (B) from the chlorite-schist plots closer to the Ba-apex whereas Ba-poor zones in K-feldspar from the same rock plot closer to the Ba-Sr edge. Replacing Ba with Sc on the plot (lower triangle on Figure 8a) shows the majority of

data plotting towards the Rb-Sr edge whereas the calc-silicate is closest to the Rb-apex. The biotite-schist clusters closer towards the Sc apex than the calc-silicate-schist.

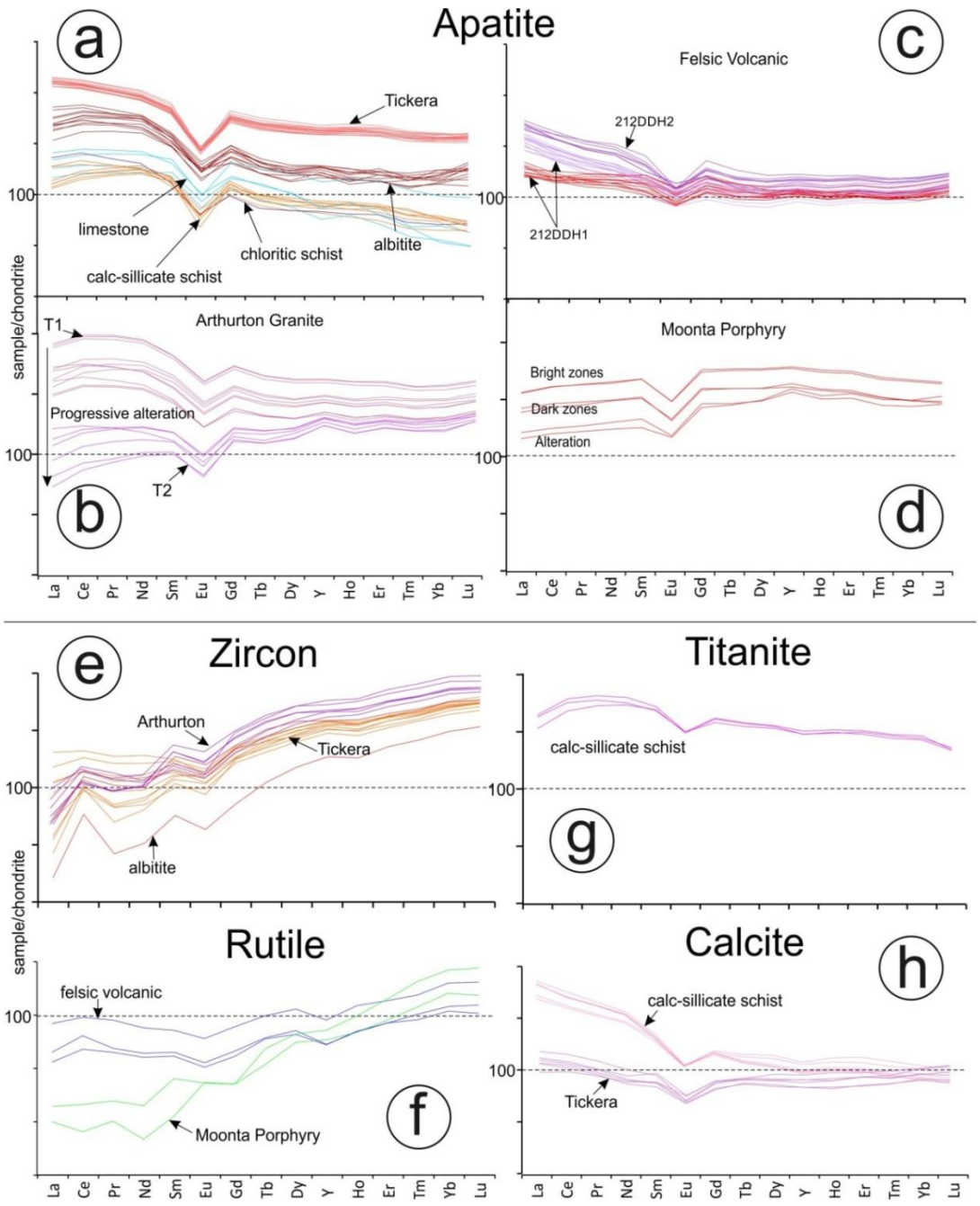

Figure 7: Chondrite-normalised REY plots outlining signatures of magmatic (a-e) and hydrothermal (f-h) accessory minerals analysed in various lithologies.

Table 10a. Summary of LA-CP-MS data for apatite: REE, Pb, Th and U (ppm)

	Y	La	Ce	Pr	Nd	Sm	Eu	Gd	Tb	Dy	Ho	Er	Tm	Yb	Lu	ΣREY	^{206}Pb	^{207}Pb	^{208}Pb	Th	U
ALTERED MAGMATIC ROCKS																					
Tickera 33PBD1, 2																					
mean (n=16)	2796	3831	8705	1023	3892	689	41	642	84	496	100	276	35	211	32	22854	39	4.4	28	214	38
S.D.	336	469	995	122	497	94	3.6	89	12	71	13	36	4.3	24	3.6	2697	11	1.2	6.5	40	10
Maximum	3561	4731	10816	1292	5057	933	48	868	115	671	134	361	43	257	39	28917	61	6.6	49	322	57
Minimum	2339	3147	7224	857	3200	566	35	517	66	395	80	224	28	171	25	18936	22	2.9	20	154	22
Arthurton 227DDH2																					
mean (n=17)	1139	476	1707	257	1096	203	29	197	26	157	34	105	14	96	18	5553	45	4.9	21	176	50
S.D.	784	525	1894	284	1181	209	30	185	22	129	26	71	9.3	62	11	5407	72	7.1	28	240	82
Maximum	2802	1624	5850	875	3635	638	93	587	72	433	88	259	33	227	41	17259	233	23	86	754	269
Minimum	374	6.4	30	6.0	37	13	2.1	27	4.6	37	10.0	35	4.9	31	6.8	628	0.89	0.10	0.81	3.3	0.41
Felsic Volcanic 212DDH1, 2																					
mean (n=29)	464	734	1087	106	394	71	12	81	10	62	14	45	6.4	45	9.0	3089	22	2.6	6.2	57	25
S.D.	167	482	706	68	255	41	3.9	41	4.5	25	5.5	17	2.3	16	2.9	1764	13	1.2	3.3	44	14
Maximum	912	1916	2900	281	1147	210	21	227	25	137	29	88	12	80	15	7434	46	4.7	14	226	60
Minimum	237	125	235	29	130	28	6.7	34	4.6	28	6.9	24	3.5	25	5.2	1179	2.5	0.72	0.54	1.3	1.6
Albitite 33DDH1																					
mean (n=12)	764	554	1726	242	1065	192	27	170	20	110	22	64	8.8	62	12	5038	9.4	2.1	3.9	16	6.3
S.D.	97	161	403	46	187	29	4.2	31	3.0	16	3.5	9.5	1.2	9.8	2.2	936	7.6	0.50	4.8	4.9	1.9
Maximum	879	899	2502	324	1326	240	35	215	25	140	28	81	11	78	15	6787	32	2.9	19	27	9.8
Minimum	595	303	1035	159	740	151	19	119	16	81	17	52	6.7	49	7.1	3361	2.1	1.3	0.93	7.1	4.0
INTENSELY ALTERED MAGMATIC ROCKS																					
Moonta Porphyry 197DDH1																					
mean (n=5)	3669	190	615	102	553	204	32	392	74	513	109	301	37	215	31	7037	3.6	0.77	2.8	18	2.3
S.D.	1501	94	318	53	277	103	15	184	35	241	49	131	16	96	12	3110	2.4	0.45	3.4	26	1.2
Maximum	5633	301	992	165	896	325	50	638	119	824	174	479	58	341	47	11016	7.2	1.3	9.4	68	3.9
Minimum	2026	60	184	31	174	65	13	162	29	224	54	161	19	117	20	3339	0.65	0.33	0.45	0.97	0.54
METASEDIMENTS																					
Chl schist 158DDH1																					
(n=1)	866	629	1772	249	1119	234	8.3	233	31	182	35	87	10	53	7.2	5515	22	3.1	11	86	24
Calc-silicate schist 38PBD2																					
mean (n=7)	894	443	1534	229	1126	234	22	233	26	150	29	78	9.5	52	6.5	5066	13	7.0	7.3	12	5.8
S.D.	147	220	613	53	150	28	2.3	46	4.5	27	5.2	15	2.2	8.8	0.94	874	10	6.5	6.7	2.2	1.7
Maximum	1093	898	2800	339	1382	275	27	300	32	195	37	97	13	62	7.7	6826	37	22	24	18	9.2
Minimum	684	268	989	174	914	188	19	168	19	117	21	52	5.9	35	5.1	3945	3.9	2.4	3.1	10	3.9
Limestone 190DDH2b																					
mean (n=4)	89	50	150	23	107	27	3.3	28	3.8	21	3.5	8.4	0.88	4.7	0.64	520	2.8	0.77	0.97	3.3	2.5
S.D.	49	16	47	6.9	32	6.6	0.61	9.7	1.5	10	1.8	5.4	0.67	3.5	0.53	162	0.68	0.04	0.16	1.3	0.63
Maximum	173	72	213	31	145	36	4.0	43	6.1	38	6.5	18	2.0	11	1.5	728	3.4	0.81	1.1	4.4	3.2
Minimum	46	30	92	14	68	19	2.4	17	2.0	11	1.8	3.9	0.39	2.1	0.28	354	1.7	0.72	0.72	1.3	1.5

Table 10b. Summary of LA-CP-MS data for apatite: other elements (ppm)

	Na	Mg	Al	Si	K	Sc	Ti	V	Mn	Fe	Cu	Ga	As	Rb	Sr	Zr	Ba
ALTERED MAGMATIC ROCKS																	
Tickera 33PBD1, 2																	
mean (n=16)	238	675	735	6140	24	1.2	274	8.4	288	2365	-	2.2	24	0.66	69	9.4	0.56
S.D.	61	951	960	1477	25	0.75	586	3.3	55	2045	-	0.93	4.0	0.29	2.5	9.7	0.28
Maximum	449	3271	3419	9593	98	3.0	2079	16	348	7745	-	4.6	32	1.6	76	36	1.1
Minimum	171	34	0.82	4218	7.6	0.51	1.8	2.2	154	580	-	1.2	19	0.34	66	2.1	0.21
Arthurton 227DDH2																	
mean (n=17)	161	412	269	2052	17	2.0	168	7.5	281	1092	-	0.44	176	0.30	136	1.4	1.1
S.D.	58	1039	658	2222	20	1.9	272	3.4	49	2018	-	0.74	67	0.18	18	1.3	0.71
Maximum	304	4501	2834	9493	86	6.3	862	18	472	8948	-	3.3	244	0.66	165	3.4	3.1
Minimum	83	9.0	0.76	227	2.5	0.11	1.3	4.6	252	206	-	0.04	42	0.13	104	0.02	0.12
Felsic Volcanic 212DDH1, 2																	
mean (n=29)	266	47	120	1065	135	0.83	6.1	1.8	230	791	-	0.42	44	0.56	204	12	4.6
S.D.	217	31	209	931	269	0.37	7.5	4.0	102	464	-	0.30	15	0.97	72	53	7.8
Maximum	1133	172	982	3879	1340	1.7	33	23	378	2376	-	1.4	90	4.6	482	291	32
Minimum	64	15	0.26	384	2.0	0.22	1.6	0.25	66	333	-	0.12	27	0.03	129	0.05	0.65
Albitite 33DDH1																	
mean (n=12)	358	38	25	1425	32	1.6	108	2.1	111	683	-	0.65	51	0.31	102	0.43	1.5
S.D.	45	31	52	383	62	0.62	331	0.59	5.0	240	-	0.32	8.2	0.15	3.7	0.35	0.30
Maximum	427	137	173	2254	236	3.0	1207	2.9	118	1436	-	1.6	67	0.76	108	1.5	1.8
Minimum	262	24	1.4	872	12	0.88	5.5	1.1	100	472	-	0.20	35	0.13	94	0.22	0.93
INTENSELY ALTERED MAGMATIC ROCKS																	
Moonta Porphyry 197DDH1																	
mean (n=5)	821	391	338	1673	225	0.36	28	0.93	126	1440	-	0.41	13	2.6	118	2.6	1.3
S.D.	206	407	310	903	119	0.22	23	0.83	14	1090	-	0.24	2.7	2.2	1.6	2.8	1.5
Maximum	1009	1171	909	3046	355	0.70	56	2.4	141	2776	-	0.79	17	5.2	120	6.3	3.9
Minimum	420	31	39	673	69	0.09	1.6	0.09	101	352	-	0.07	9.2	0.29	117	0.11	0.11
METASEDIMENTS																	
Chl schist 158DDH1																	
(n=1)	104	142	88	1451	11	-	11	1.6	327	493	6.0	0.49	9.1	0.16	168	<mdl	0.46
Calc-silicate schist 38PBD2																	
mean (n=7)	400	164	303	2475	22	5.8	4.9	46	1067	3.6	4.2	0.76	182	0.73	88	<mdl	1.4
S.D.	388	121	629	2100	13	2.3	1.1	4.7	415	2.9	1.6	0.30	13	0.51	8.9	<mdl	0.74
Maximum	1347	364	1841	7587	47	9.9	5.9	53	1657	9.0	7.6	1.2	203	1.6	104	<mdl	2.4
Minimum	188	22	1.5	1357	9.4	3.8	2.9	40	590	0.56	2.5	0.32	163	0.17	75	<mdl	0.00
Limestone 190DDH2b																	
mean (n=4)	616	1663	1574	4120	271	56	2.9	1066	3697	154	150	0.86	72	1.7	99	46	9.3
S.D.	816	1370	1292	3720	228	45	2.7	391	3464	182	244	0.79	53	1.6	24	24	6.5
Maximum	2027	3854	3130	9949	651	128	7.3	1374	9368	453	573	2.2	157	4.3	133	71	18
Minimum	105	277	99	525	45	17	0.36	399	585	3.9	0.56	0.09	26	0.08	67	19	2.5

Table 11. Summary of LA-CP-MS data for zircon (ppm)

	Na	Mg	Al	P	K	Ca	Sc	Ti	V	Mn	Fe	Cu	Zn	Ga	As	Rb	Sr	Nb	Mo	Sn	Ba	Hf	Ta	W
ALTERED MAGMATIC ROCKS																								
Tickera granite 33PBD1-Zr-6																								
Mean (n=6)	435	5367	6039	986	72	1344	651	4339	29	312	11422	5.1	18	6.6	12	1.7	15	55	1.8	14	7.9	10965	5.9	4.2
S.D	93	6100	5681	570	37	746	147	6941	26	138	8617	2.6	15	5.3	6.6	0.20	6.0	86	0.35	23	5.2	801	5.4	3.8
Maximum	601	18409	17661	1738	152	2830	953	19464	86	493	26464	9.6	49	17	24	2.1	26	247	2.3	66	16	11836	18	12
Minimum	295	98	440	360	46	522	522	60	11	91	2032	1.8	3.9	0.65	3.8	1.5	7.0	7.5	1.3	1.9	3.7	9324	3.0	0.50
Arthurton granite 193DDH1																								
Mean (n=10)	72	196	5613	1590	4191	919	419	33	12	11	3545	31	50	2.7	3.8	10	475	4.1	1.7	0.76	21	10030	1.7	1.7
S.D	70	222	6919	665	6760	697	25	16	7.6	7.8	3545	24	51	2.5	1.9	13	537	0.86	0.92	0.37	31	419	0.43	0.85
Maximum	233	617	18330	2885	20936	2408	453	68	25	25	10097	71	164	6.9	7.4	40	1675	5.4	4.1	1.4	110	10650	2.7	3.3
Minimum	14	9.7	145	630	24	192	377	14	2.8	3.7	94	2.2	3.2	0.31	0.46	0.45	14	2.9	0.86	0.26	0.93	9337	1.2	0.68
INTENSELY ALTERED MAGMATIC ROCKS																								
Albitite 33DDH1																								
Mean (n=2)	267	27	950	185	673	424	269	20	4.3	31	5023	1.3	0.96	1.3	9.8	3.1	6.8	3.5	4.3	1.4	32	4205	0.87	0.58
S.D	244	21	365	5.1	159	231	25	11	4.0	27	3467	0.43	0.04	0.59	6.5	0.44	5.1	0.80	0.44	0.83	16	259	0.08	0.08
Maximum	511	48	1315	190	832	655	293	31	8.3	58	8490	1.7	0.99	1.9	16	3.5	12	4.3	4.8	2.3	48	4464	0.95	0.65
Minimum	24	5.2	585	180	514	193	244	8.4	0.32	3.3	1556	0.84	0.92	0.71	3.2	2.6	1.6	2.7	3.9	0.60	16	3946	0.79	0.50

	Y	La	Ce	Pr	Nd	Sm	Eu	Gd	Tb	Dy	Ho	Er	Tm	Yb	Lu	ΣREY	^{206}Pb	^{207}Pb	^{208}Pb	Th	U
ALTERED MAGMATIC ROCKS																					
Tickera granite 33PBD1-Zr-6																					
Mean (n=6)	4206	11	97	10	56	56	14	145	52	556	161	670	132	1154	183	7170	443	46	42	893	661
S.D	1005	8.6	28	3.4	16	19	5.3	45	15	149	39	173	36	308	46	1330	66	8.2	11	443	104
Maximum	6018	29	136	16	84	83	24	204	72	741	225	979	197	1722	269	9072	521	57	54	1620	813
Minimum	2937	4.4	66	7.1	42	28	7.4	79	29	340	113	468	93	820	135	5267	369	36	24	337	516
Arthurton granite 193DDH1																					
Mean (n=10)	1937	25	116	12	64	29	8.1	79	23	226	64	252	48	424	73	3379	251	29	30	370	243
S.D	293	29	67	9.3	45	10	2.3	17	4.3	40	10	37	6.4	61	9.7	471	33	4.4	7.5	69	37
Maximum	2318	98	268	33	167	46	12	106	28	276	78	289	56	522	94	4035	308	38	43	490	320
Minimum	1397	1.7	54	2.3	19	15	4.2	54	15	155	44	178	36	306	55	2349	183	21	20	270	182
INTENSELY ALTERED MAGMATIC ROCKS																					
Albitite 33DDH1																					
Mean (n=2)	1632	2.8	59	5.5	25	30	7.9	66	24	234	59	231	45	391	67	2878	199	22	35	204	200
S.D	1049	2.3	39	4.9	21	26	7.0	56	19	174	39	139	26	216	35	1853	52	5.1	17	105	86
Maximum	2681	5.1	99	10	46	56	15	122	43	408	98	370	71	607	101	4731	251	27	53	309	286
Minimum	583	0.53	20	0.57	4.4	4.6	0.96	10	4.6	59	19	92	19	175	32	1025	147	17	18	100	114

Table 12. Summary of LA-CP-MS data for rutile, titanite and calcite (ppm)

	Na	Mg	Al	Si	P	K	Ca	Sc	V	Cr	Mn	Fe	Cu	Zn	Ga	Rb	Sr	Zr	Nb	Mo	Sn	Sb	Ba	Hf	Ta	W
RUTILE -ALTERED MAGMATIC ROCKS																										
Felsic Volcanic 212DDH1																										
Mean (n=2)	245	196	194	3249	12	37	1087	243	216	5.7	142	2548	12	10	0.85	0.30	8.1	797	7092	1.8	108	0.53	18	47	773	13
S.D.	125	24	95	2.7	2.9	21	833	43	27	1.7	90	204	0.55	3.2	0.43	0.09	4.3	155	1780	0.02	10	0.22	10	7.8	393	0.36
Maximum	370	220	289	3252	15	59	1920	286	243	7.4	232	2752	12	13	1.3	0.40	12	952	8871	1.8	118	0.75	28	55	1166	13
Minimum	120	172	99	3247	9.4	16	254	199	188	4.0	52	2344	11	7.1	0.43	0.21	3.9	641	5312	1.7	97	0.31	8.0	39	380	13
RUTILE - INTENSELY ALTERED MAGMATIC ROCKS																										
Moonta Porphyry 197DDH1																										
Mean (n=2)	160	6842	9649	15047	11	2520	829	398	135	8.9	37	13374	417	24	7.1	15	6.1	102	7738	0.39	514	0.18	7.2	9.3	1049	51
S.D.	13	4859	6137	9154	1.9	1165	221	69	5.0	1.0	9.4	5029	236	9.0	4.0	8.4	1.5	32	380	0.09	14	0.11	0.31	1.1	156	5.7
Maximum	174	11701	15786	24201	13	3685	1050	467	140	10.0	46	18403	654	33	11	23	7.6	133	8117	0.48	528	0.29	7.5	10	1204	57
Minimum	147	1983	3513	5893	9.4	1355	608	329	130	7.9	28	8346	181	15	3.1	6.5	4.7	70	7358	0.30	501	0.08	6.9	8.2	893	46
TITANITE - METASEDIMENTS																										
Calc-sillicate schist 38PBD2																										
Mean (n=3)	622	922	7238	6202	39	3.9	912	60	130	17653	6.8	10	15	17	6.4	58	3.7	2555	193	1707	14	545	2.2	12	67	8.2
S.D.	381	401	1270	8557	20	0.37	173	16	32	2693	6.9	6.3	4.4	2.1	1.9	8.1	2.5	190	67	94	3.8	63	0.66	2.8	5.2	3.3
Maximum	1156	1480	8779	18302	67	4.2	1106	78	171	20417	17	19	21	20	9.0	70	7.2	2822	277	1834	18	631	3.1	14	75	12
Minimum	288	557	5669	38	20	3.4	685	39	92	14003	0.95	4.3	11	15	4.4	52	1.5	2399	114	1610	9.0	482	1.5	7.7	63	4.1
CALCITE - ALTERED MAGMATIC ROCKS																										
Tickera granite 33PBD2																										
Mean (n=6)	48	833	70	285	9.6	21	-	8.0	0.20	-	7743	808	-	-	0.06	0.10	105	-	-	-	-	-	2.4	-	-	0.04
S.D.	13	385	59	143	2.2	20	-	2.5	0.08	-	1295	117	-	-	0.04	0.07	21	-	-	-	-	-	1.4	-	-	0.02
Maximum	62	1397	179	429	13	63	-	11	0.34	-	10454	981	-	-	0.12	0.23	131	-	-	-	-	-	4.5	-	-	0.09
Minimum	21	433	2.8	11	7.2	4.3	-	3.5	0.11	-	6662	593	-	-	0.00	0.02	63	-	-	-	-	-	0.27	-	-	0.01
CALCITE - METASEDIMENTS																										
CALCITE - Calc-sllicate schist 38PBD1																										
Mean (n=6)	260	3636	15	334	62	11	-	32	0.87	-	4572	18354	6.5	1.9	0.24	0.16	171	-	-	-	-	-	0.68	-	-	-
S.D.	18	1132	18	141	9.8	6.2	-	5.9	0.18	-	2673	3326	9.1	3.1	0.08	0.14	20	-	-	-	-	-	0.36	-	-	-
Maximum	286	5238	43	541	84	24	-	43	1.1	-	10073	23622	23	8.8	0.33	0.43	201	-	-	-	-	-	1.1	-	-	-
Minimum	237	1600	0.07	180	56	5.6	-	23	0.56	-	2281	12754	0.03	0.16	0.11	0.01	135	-	-	-	-	-	0.06	-	-	-

	Y	La	Ce	Pr	Nd	Sm	Eu	Gd	Tb	Dy	Ho	Er	Tm	Yb	Lu	ΣREY	^{206}Pb	^{207}Pb	^{208}Pb	Th	U
RUTILE -ALTERED MAGMATIC ROCKS																					
Felsic Volcanic 212DDH1																					
Mean (n=2)	90	10	36	4.9	18	5.4	1.4	8.2	2.5	22	5.7	21	4.4	44	7.0	281	99	61	82	163	28
S.D.	43	6.9	21	2.9	9.8	2.7	0.76	4.5	1.1	11	2.8	9.2	1.7	20	3.1	140	35	25	33	79	9.4
Maximum	132	17	58	7.8	28	8.1	2.2	13	3.6	33	8.4	30	6.0	64	10	421	134	87	114	243	38
Minimum	47	3.4	15	2.0	8.1	2.7	0.65	3.7	1.4	11	2.9	12	2.7	24	3.9	140	65	36	49	84	19
RUTILE - INTENSELY ALTERED MAGMATIC ROCKS																					
Moonta Porphyry 197DDH1																					
Mean (n=2)	72	0.41	0.99	0.19	0.66	0.65	0.34	1.1	0.69	9.9	4.1	23	7.2	76	12	209	46	19	27	3.8	18
S.D.	14	0.13	0.51	0.08	0.40	0.43	0.00	0.01	0.22	1.7	1.4	9.6	3.5	34	6.3	70	9.5	4.8	7.4	1.8	1.9
Maximum	87	0.53	1.5	0.27	1.1	1.1	0.34	1.2	0.91	12	5.5	33	11	110	18	279	56	24	34	5.6	20
Minimum	58	0.28	0.48	0.11	0.26	0.22	0.34	1.1	0.47	8.1	2.8	13	3.7	42	5.9	140	37	14	20	2.0	16
TITANITE - METASEDIMENTS																					
Calc-sillicate schist 38PBD2																					
Mean (n=3)	9.5	773	4400	791	3635	812	96	631	91	551	96	271	35	205	18	14959	180	53	74	78	92
S.D.	2.2	204	1060	158	597	73	2.2	59	7.1	31	7.2	20	2.8	18	1.0	2277	96	33	53	34	32
Maximum	13	961	5585	987	4459	911	97	690	97	584	106	294	38	228	19	17877	311	100	148	124	134
Minimum	7.3	488	3012	600	3060	737	93	550	81	510	89	246	31	185	17	12320	84	25	32	43	57
CALCITE - ALTERED MAGMATIC ROCKS																					
Tickera granite 33PBD2																					
Mean (n=6)	86	29	67	8.0	29	8.6	1.5	10.0	2.1	14	3.1	9.8	1.6	12	1.9	284	0.57	0.24	0.42	0.25	0.05
S.D.	15	7.0	15	1.6	5.6	1.6	0.19	1.3	0.18	2.2	0.65	1.8	0.28	2.1	0.47	35	0.17	0.12	0.15	0.07	0.08
Maximum	111	42	95	11	40	11	1.8	11	2.3	18	4.3	12	2.1	15	2.5	342	0.89	0.47	0.65	0.36	0.24
Minimum	69	19	49	6.3	23	6.6	1.3	8.0	1.8	11	2.3	7.4	1.3	9.3	1.3	233	0.39	0.12	0.25	0.12	0.00
CALCITE - METASEDIMENTS																					
CALCITE - Calc-sllicate schist 38PBD1																					
Mean (n=6)	166	946	1458	151	497	63	6.7	43	5.7	34	6.6	19	2.5	14	1.8	3415	3.5	1.6	2.7	4.3	0.13
S.D.	34	247	341	32	86	6.1	0.21	2.3	0.83	7.3	1.5	4.8	0.63	3.3	0.42	658	0.68	0.34	0.57	2.7	0.08
Maximum	222	1227	1971	194	608	73	7.0	47	7.2	47	9.4	28	3.7	20	2.6	4323	4.4	2.1	3.5	9.6	0.28
Minimum	132	560	972	104	368	54	6.5	39	4.9	28	5.2	15	1.9	11	1.4	2410	2.5	1.1	2.0	2.1	0.00

Albite analyses from altered magmatic rocks, and the albitite in particular, show a large spread in the centre of the ternary Rb-Ba-Sr but towards the Ba-Rb edge (particularly Tickera granitoid T2). The metasediments are, in contrast, dispersed along the Ba-Sr edge, allowing a line to be drawn separating the two groups (Figure 8b). The ternary Rb-Sr-(Sc*10) plot (lower triangle on Figure 8b) shows the magmatic rocks clustering around the Sr-Rb edge, whereas the metasediments form a second trend parallel to the Sr-Sc edge, with the calc-silicate-schist close to the Sc-apex.

A ternary (Th*10)-^{208}Pb-(U*10) plot for K-feldspar (Figure 8c) shows an uneven spread for K-feldspar in terms of lithologies, however all analyses congregate towards the Pb apex. The Th-^{208}Pb-U diagram for albite (Figure 8d) discriminates between lithologies in the same way as the plots in Figure 8b. Albite from the biotite-schist is closest to the Th-apex whereas the Tickera granitoid tightly clusters towards the Pb apex. The albitite, calc-silicate-schist and Arthurton granitoid plot towards the centre of the diagram.

There is an overall positive correlation between Rb and Ba concentrations in K-feldspar (Figure 8e), with each lithological group forming a tight cluster. The Rb vs. Ba plot for albite (Figure 8f) also shows tight clusters but with a strong negative correlation between the two elements. Concentrations of both elements are higher in K-feldspar. The opposite sense of slope for the two minerals may possibly reflect inherited magmatic signatures, in the case of K-feldspar, versus formation of hydrothermal albite under equilibrium conditions from a common fluid (noting also how, within each cluster on Figure 8f, the individual points also correlate).

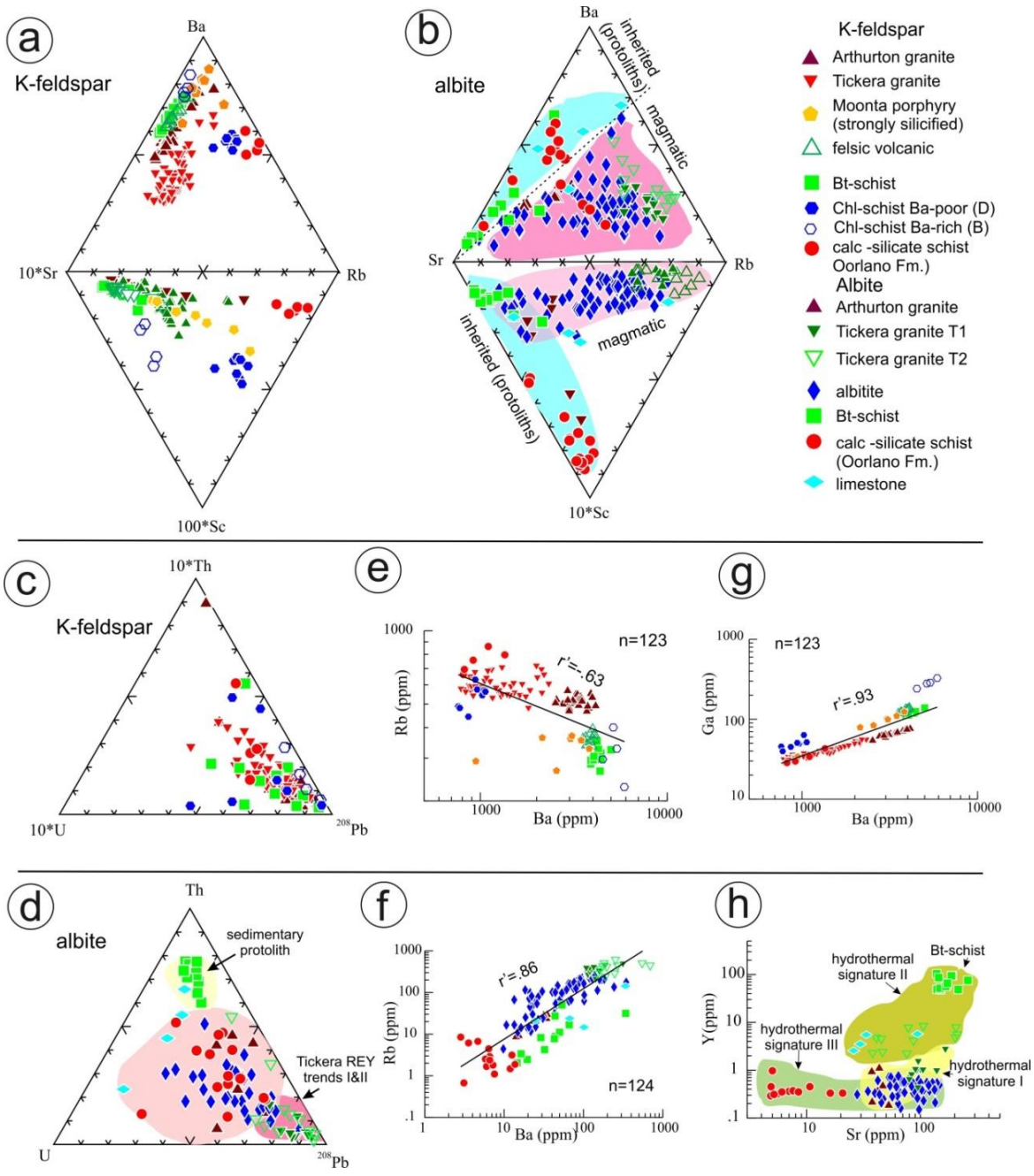

Figure 8: Plots for feldspars showing other trace element patterns and correlations. (a, c) Ternary plots of Rb-Ba-(Sr*10), Rb-(Sc*100)-(Sr*10) and ^{208}Pb-(Th*10)-(U*10) for K-feldspar. (b, d) Ternary plots of Rb-Ba-Sr, Rb-(Sc*10)-Sr and ^{208}Pb-Th-U for albite. (e, g) Binary plots of Rb vs. Ba and Ga vs. Ba for K-feldspar. (f, h) Binary plots of Rb vs. Ba and Y vs. Sr for albite.

The Ga vs. Ba plot for K-feldspar (Figure 8g) indicates a strong positive linear relationship (r' = 0.93), particularly for the magmatic K-feldspar, possibly suggestive of a coupled substitution relationship. The plot of Y vs. Sr for albite (Figure 8h) reflects the groupings based on absolute ΣREY concentrations. The three signatures for albite (Figure 6d-f) cluster well. Albitite has higher Sr concentrations, possibly inherited from calcic domains in albite (see above, Figure 2m). Calc-silicate-schist has lowest Sr, attributable to the availability, in that rock, of other minerals capable of incorporating Sr. In contrast, in the biotite-schist, there are no calcic minerals, leading to the incorporation of Sr in albite.

Element mapping

LA-ICP-MS mapping allows a visual assessment of changes in trace element distributions during alteration. Element maps of a brecciated magmatic feldspar within the Arthurton granitoid (Figure 9) show patterns of trace element redistribution during progressive albitization propagated via fractures. The maps show clearly that an increase in Na due to albitization is positively correlated with an increase in Sr and in LREE (La shown as a proxy on the maps). In the areas showing Na-enrichment, Ba and Ga are markedly depleted. The element map for Rb shows a homogeneous distribution, indicating it is neither enriched nor depleted.

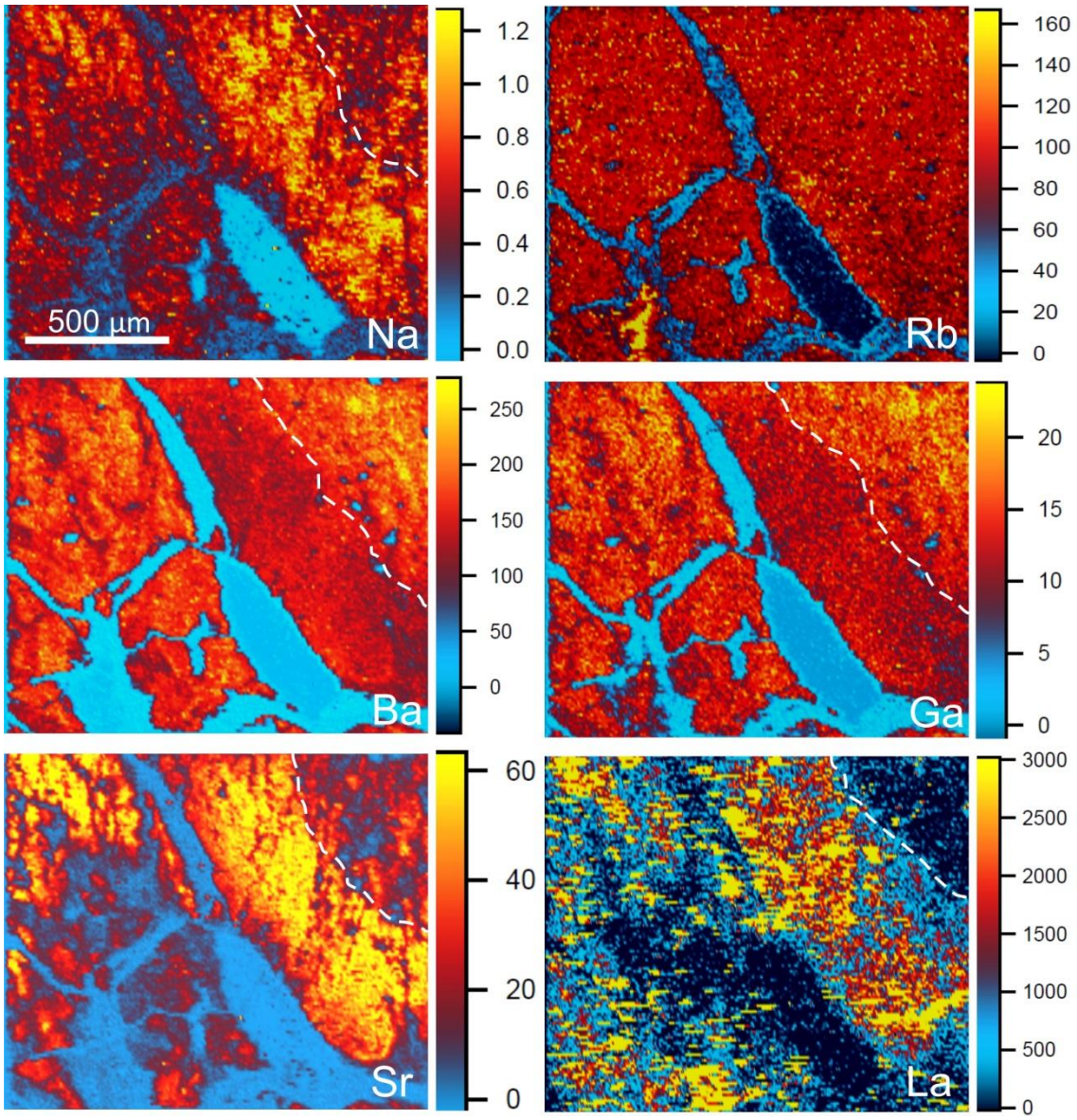

Figure 9: LA-ICP-MS elemental maps displaying distributions within brecciated K-feldspar in the Arthurton granitoid. Note white line representing onset of albitization and brecciation. Scale for La in counts per second (cps); 10^3 cps for Rb, Ba, Ba, Sr; 10^6 cps for Na.

The map for albite with a K-feldspar band in the middle from biotite-schist (Figure 10) shows enrichment in Rb, Ba and Ga, corresponding to the K-feldspar, whereas LREE are enriched in albite relative to K-feldspar. Other elements, notably Cs, Zn, Ti and Nb, but also some REE, are enriched in the small inclusions of biotite. This map shows clearly that, of the two feldspars, albite incorporates more LREE, either as sub-microscopic mineral inclusions or in solid solution.

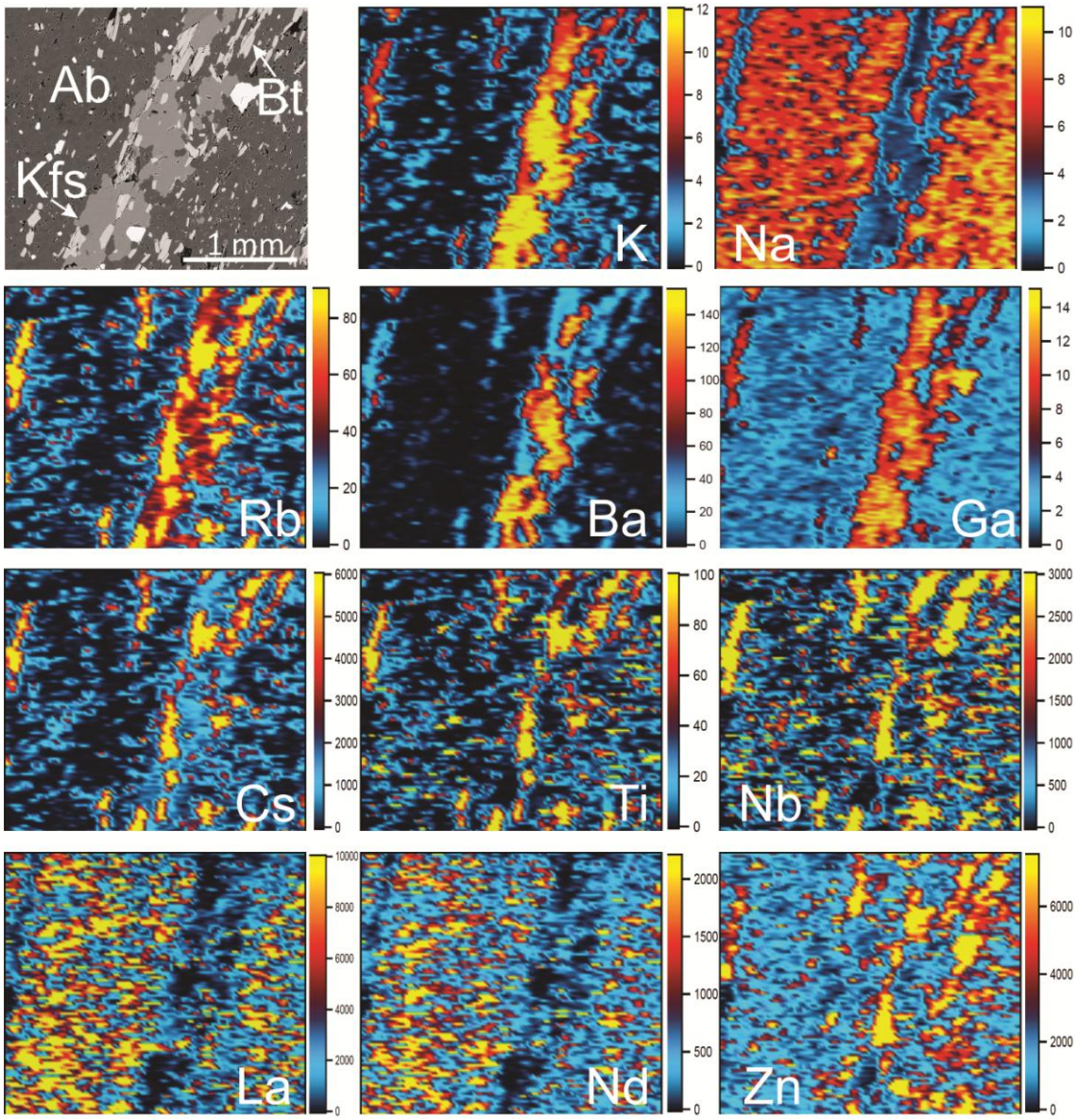

Figure 10: BSE image and LA-ICP-MS element maps for albite and K-feldspar in the biotite-schist. Scales for Cs, Nb, La, Nd, Zn in cps; 10^3 cps for Rb, Ba, Ga, Ti; 10^6 cps for K and Na.

DISCUSSION

Mineral chemistry and trace element incorporation

Mineral chemistry is dependent on the affinity for, and crystallographic site preferences of, particular elements. In the present study, minerals formed from granitic melts as well as via fluid-rock interaction have been analysed.

During element partitioning in melts and solids, elemental idiosyncrasies, in particular atomic radius and valence (Goldschmidt 1937), determine the outcomes of nanoscale interactions. Fluid-rock interactions during hydrothermal processes can remobilise elements, causing them to fractionate within new minerals based on the stabilities of ligands within the fluid (e.g. Dongen *et al.* 2010). Ions will form complexes relative to the size and charge of a particular ligand. For example, small, highly-charged REE, Y and Zr ions preferentially form complexes with ligands of similar attributes such as fluoride complexes (Bau & Dulski 1995). The mineral chemistry of a given magmatic-hydrothermal system is reliant not only on element ligands in the fluid, but also on element affinities and ultimately, crystal structure of each mineral component in the rock.

As documented in previous sections, feldspars show a range of trace element concentrations and REY-anomalies. Potassium feldspar and albite are framework silicates given by the formulae: $KAlSi_3O_8$ and $NaAlSi_3O_8$, respectively. Due to the presence of alkali ions in these minerals, coupled substitutions commonly occur among incompatible LILE (e.g. K, Ba, Rb, Cs, $Pb^{2+,}$ Sr and Eu^{3+}). Moreover, LREE are suggested to be more effective than HREE in competing for the K^+ and Na^+ sites in feldspars (Stix & Gorton 1990).

The relative elemental affinities between Ba and Rb can be used to further explain the trends observed on the Ba vs. Rb plots for feldspar (Figure 8e, f). Ba^{2+} and Rb^+ ions

have a similar ionic radius to K^+, but are much larger than the Na^+ ion, thus readily explaining enrichment of these elements in potassium feldspar relative to albite. Apatite-group minerals, in this case fluorapatite, [$Ca_5(PO_4)_3F$], is a recognised repository for significant REE. Substitution of REE^{3+} for Ca^{2+} is compensated by replacement of P^{5+} by Si^{4+} (Fleet & Pan 1994). Similarly, zircon ($ZrSiO_4$) hosts substantial REE. Substitutions are common for both incompatible LILE and High Field Strength Elements (HFSE). In addition, Y and Sr are highly compatible within both apatite and zircon (Rakovan & Hughes 2000). Due to the resistant nature and ability of both minerals to host trace elements, they have been widely used as petrogenetic indicators (e.g. Belousova *et al.* 2002a; Belousova *et al.* 2002b). Moreover, apatite analysed in this study frequently displays REY-depleted hydrothermal rims relatively to magmatic cores in the igneous rocks, and can thus be used to further constrain trace element remobilisation during hydrothermal alteration.

As documented here, hydrothermal accessory minerals formed during albitization such as rutile (TiO_2), titanite ($CaTiSiO_5$) and calcite ($CaCO_3$) can also carry significant concentrations of trace elements (Figure 7f-h).

REY distributions

Fractionation of trivalent REE and Y within minerals is predominantly governed by the systematic decrease in atomic radius with increased atomic number (e.g. Smith *et al.* 2004). However, hydrothermal processes, such as albitization, are accompanied by changes in fluid characteristics (e.g. redox conditions, pH, temperature and salinity), which can assist partitioning of adjacent REE from one another (Bau 1991). Trivalent

Eu and Ce can change oxidation states to Eu^{2+} and Ce^{4+}, creating measurable anomalies relative to adjacent elements. In addition, the anomalous behaviour of Y relative to neighbouring elements, i.e. Dy and Ho, in hydrothermal systems can be a useful petrogenetic indicator (Smith *et al.* 2009). Subsequently, REY trends of magmatic-hydrothermal systems can be discriminated by variations in Eu-, Ce- and Y-anomalies and changes in REY-slopes.

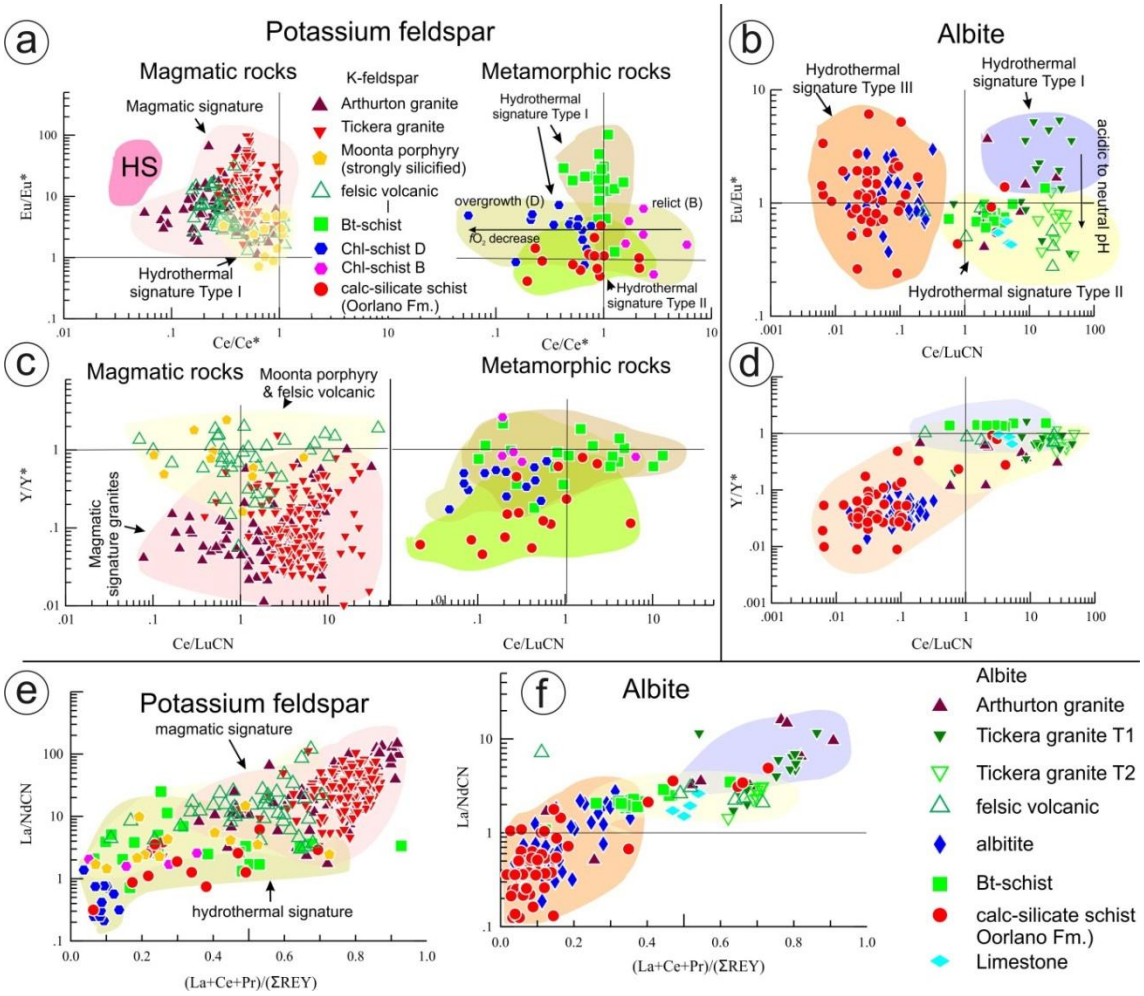

Figure 11: Plots representing anomalies and slopes within chondrite-normalised REY trends of feldspars. Eu/Eu* = $Eu_{CN}/[(Sm_{CN} + Gd_{CN})/2]$, Ce/Ce* = $Ce_{CN}/[(La_{CN} + Pr_{CN})/2]$ and Y/Y* = $Y_{CN}/[(Dy_{CN} + Ho_{CN})/2]$.

Feldspar REY fractionation trends can be differentiated by their Eu/Eu* vs. Ce/Ce* ratios (Figure 11a, b). Magmatic K-feldspar is characterised by a pronounced positive Eu-anomaly and negative Ce-anomaly, whereas hydrothermal K-feldspar is quite variable in terms of these anomalies. All magmatic K-feldspar clusters together, and are separated from Hillside granite (Ismail *et al.* in press); the Tickera and Arthurton granitoids are, however, slightly discriminated from one another in Figure 11a. This indicates both regional and local differences among granitoids from the Hiltaba suite. This possibly relates to variations in the oxidation state of magmas, as also shown by the differences in Fe-Ti-speciation in each rock. Hydrothermal K-feldspar shows transition from positive to negative Ce-anomaly correlating to Ba-rich relicts to Ba–poor rim in the chlorite-schist. Such changes can be attributed to variation in either redox or pH in the fluid. The former is more feasible, considering that hematite, which is sensitive to redox changes, is partially replaced by magnetite.

Eu/Eu* vs. Ce/Lu_{CN} (a measure of the LREE/HREE fractionation) for albite distinctively clusters all three REY fractionation trends (Figure 11b). The Tickera granitoid shows a spread from positive to negative Eu-anomaly for albite type-I and type-II, respectively. This can be interpreted either as a change in pH from acidic to neutral, supported by co-crystallisation of hydrothermal K-feldspar and T2-albite, or as a decrease in fO_2 (from hematite to magnetite stability). Both Fe-oxides are present as minute inclusions within domains of reaction where hydrothermal K-feldspar is formed.

Y/Y* vs. Ce/Lu_{CN} plot for K-feldspar separates the granitoids from felsic volcanics, whereas the plot for metamorphic rocks shows no clear separation of the hydrothermal

trends (Figure 11c). This suggests equilibrium partitioning of REE in accessory minerals, particularly in abundant zircon, in the granitoids relative to felsic volcanics. Such an interpretation is supported by the observed clustering of zircon with early magmatic Fe-Ti-oxides. Y/Y* vs. Ce/Lu_{CN} plot for albite (Figure 11d) shows a pronounced negative Y-anomaly only for hydrothermal signature III in rocks with abundant Y-bearing accessory minerals (rutile and titanite in the albitite and calc-silicate-schist).

The La/Nd_{CN} vs. (La+Ce+Pr)/ΣREY plot for K-feldspar shows a separation of magmatic from hydrothermal signatures, whereby the latter shows no particular discrimination by lithology (Figure 11e). A similar plot for albite shows discrimination between the three hydrothermal signatures where a positive correlation is seen between the two variables and the trends from III to I (Figure 11f). Variation of the La/Nd ratio in discrete REE-minerals from Bayan Obo has been attributed to $X(CO_2)$ concentration in hydrothermal fluids relating to different mineralization stages (Smith *et al.* 2000). The albite groupings observed here could also be interpreted as reflecting variation in volatiles and their speciation during albitization.

Anomalies in REY fractionation trends displayed by magmatic apatite have been used to infer variation in the oxidation state of magma (e.g. Cao *et al.* 2012). Eu/Eu* vs. Ce/Lu_{CN} and Eu/Eu* vs. Ce/Ce* plots for apatite here show magmatic apatite in granitoids as tighter clusters when compared to apatite from felsic volcanics or other rocks (Figure 12 a, b). On both diagrams, Tickera apatite cores show larger negative Eu-anomalies and lower Ce-anomalies relative to Arthurton. This clearly correlates with the

interpretations above, indicating a more reduced magma character for the Tickera granitoid. There is no correlation Eu/Eu* and Ce/Ce* in the LREE-depleted rims with either Eu- or Ce-anomalies. A plot of Y/Y* vs. Ce/Lu_{CN} (Figure 12c) shows that apatite of the Tickera and Arthurton granitoids share a common inverse relationship between the two variables. Tickera has a small negative Y-anomaly and is LREE-enriched relative to Arthurton and is also distinguished by a positive Y-anomaly. Apatite from felsic volcanics are clearly separated from apatite from all the other rocks on the La/Nd_{CN} vs. (La+Ce+Pr)/ΣREY plot (Figure 12d). Their positions at higher La/NdCN ratios suggest fluids with variable and high volatile concentration during albitization development. A comparable separation of apatite in felsic volcanic is also notable in terms of Ce-anomaly. This correlates with progressive alteration resulting in LREE-depletion.

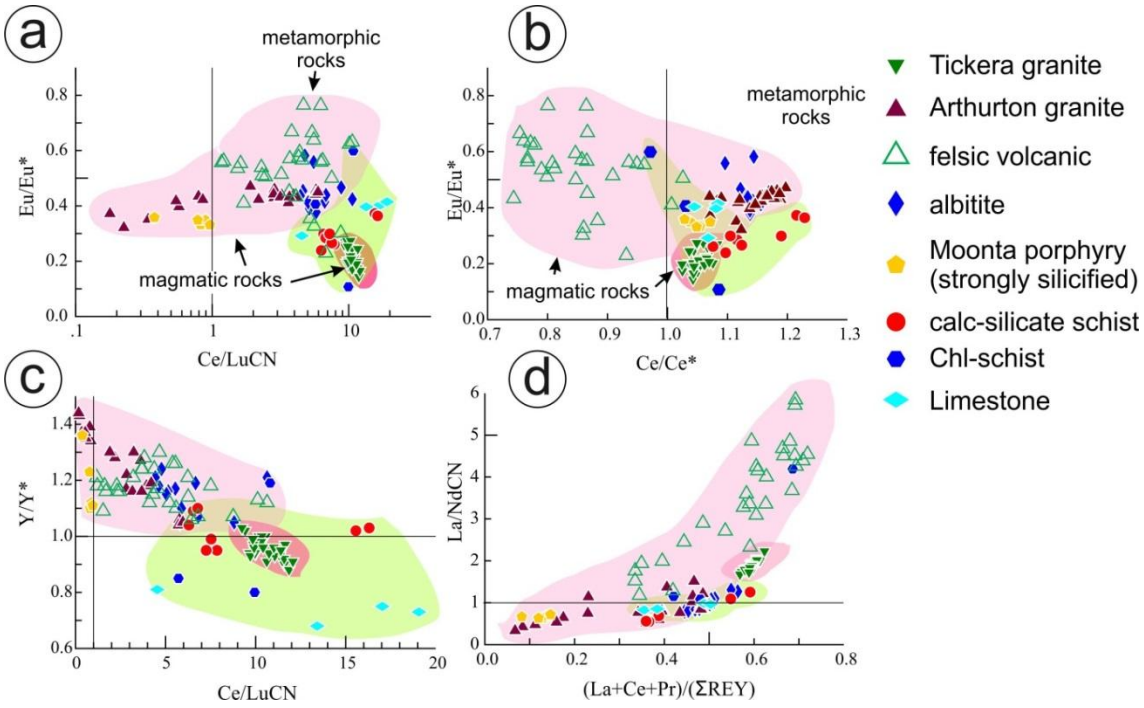

Figure 12: Plots representing anomalies and slopes within chondrite-normalised REY trends of apatite. Eu/Eu* = $Eu_{CN}/[(Sm_{CN} + Gd_{CN})/2]$, Ce/Ce* = $Ce_{CN}/[(La_{CN} + Pr_{CN})/2]$ and Y/Y* = $Y_{CN}/[(Dy_{CN} + Ho_{CN})/2]$

In addition to the above plots, the REY patterns of zircon justify the interpreted magmatic oxidation state reflected by apatite in the granitoids. The observed increase in Ce-anomaly for Arthurton relative to Tickera zircon can be attributed to an increase in fO_2, as documented in experimental studies with hydrous silicate melts at 10 kbar and 800-1300 ºC (Trail *et al.* 2012).

Alkali-metasomatism

The range of mineral reactions, textural variety and REY-signatures summarising regional alkali-metasomatism in the Moonta-Wallaroo area is shown schematically on Figure 13. All discrete REY- and REY-bearing accessory minerals are also carriers of U, and in most cases also Th, and therefore account for the broad U-enrichment in IOCG systems.

Other contenders for REY-incorporation are Fe-oxides and hydroxides. Preliminary LA-ICP-MS data (not included here) show that both groups are REY-carriers. However, their mineralogical speciation requires further investigation. Their textures, including those resulting from superimposed weathering processes, indicate a complexity that needs to be addressed at the sub-micron-scale. A treatment of the role of these minerals is beyond the scope of the present paper.

SODIC ALTERATION: ALBITIZATION

The hypothesis linking albitization and REY-enrichment in IOCG systems can be proven by showing that albite formation accounts for the anomalous REY-enrichment

of a given rock that is part of the regional alteration. Regional metamorphism, without addition of alkalis from an external source, can account for alkali feldspar-rich lithologies given the right pre-metamorphic protolith (e.g. the presence of evaporites in a sedimentary sandstone-shale sequence). This cannot, however, explain the anomalously high-ΣREY (~200 ppm) contained within lithologies such as the biotite-schist (Figure 13a). The data here shows that albite, a major component (~30%) of the biotite-schist, not only accounts for the bulk of ΣREY in this rock but also mimics the whole-rock REY pattern (Figure 13b). The demonstrated REY-enrichment in such a lithology thus requires an additional source of fluids.

Alteration throughout the magmatic rocks can be tied to metasomatic reactions involving a highly-oxidised (hematite-stable), slightly acidic fluid (breakdown of perthitic feldspar and andesine). Assuming metamorphism is coeval with metasomatism in the area (e.g. Conor *et al.* 2010), then the same fluid should explain REE-rich-albite-K-feldspar-biotite prograde formation in the sedimentary sequence. Whether this early fluid is also Na-bearing is difficult to constrain due to the lack of data on pre-metamorphic protoliths in the area. A progressive neutralisation of this fluid is shown by the late occurrence of hydrothermal K-feldspar in the magmatic and metamorphic rocks. Initial albitization promotes sericite but precludes K-feldspar formation, as seen from the absence of the latter in the limestone.

Formation of discrete REY-minerals is determined by local reactions with different expression in each rock type, e.g. breakdown of Fe-Ti-oxides, and the formation of rutile + bastnäsite + xenotime and titanite + bastnäsite assemblages in granitoids and

calc-silicate-schist, respectively. The mineral reactions portrayed for the magmatic rocks (Figure 13b) show how Ca, K and REY can also be locally remobilised from one site of reaction to another, and conclude with an increased abundance of REY- or REY-bearing accessory minerals (rutile) in albitite. Analogously, progressive enrichment of REY- or REY-bearing minerals (epidote, actinolite, titanite and apatite) in the calc-silicate-schist is apparent. Accordingly, the REY-signatures of albite reflect equilibrium partitioning in each respective assemblage. In the absence of REY-hosting minerals, albite from the biotite-schist is the sole REY-carrier. The granoblastic textures shown by albite in both the biotite- and calc-silicate-schists support the prograde sense of reaction in both cases, but the differences in the REY signature of albite reflect the effects of partitioning as stated above. The differences in the nature of the pre-metamorphic protoliths are highlighted by the LILE plots for both K-feldspar and albite (Figure 8a, b), as well as by the Th-^{208}Pb-U plot for albite (Figure 8d). Overall, the suggested element exchange during feldspar reactions is also backed-up by the element maps (Figures 9, 10).

Hövelmann *et al.* (2010) suggest that albitization emanates via an interface-coupled-dissolution-(re)-precipitation mechanism, during which increased porosity drives pervasive fluid flow. Furthermore, experiments performed by Hövelmann *et al.* (2010) also reveal remobilisation and incorporation of Ti, Fe, Mg, Sr, Ba, Rb, Pb, La, Ce and Eu within the fluid of the amorphous stage of albitization.

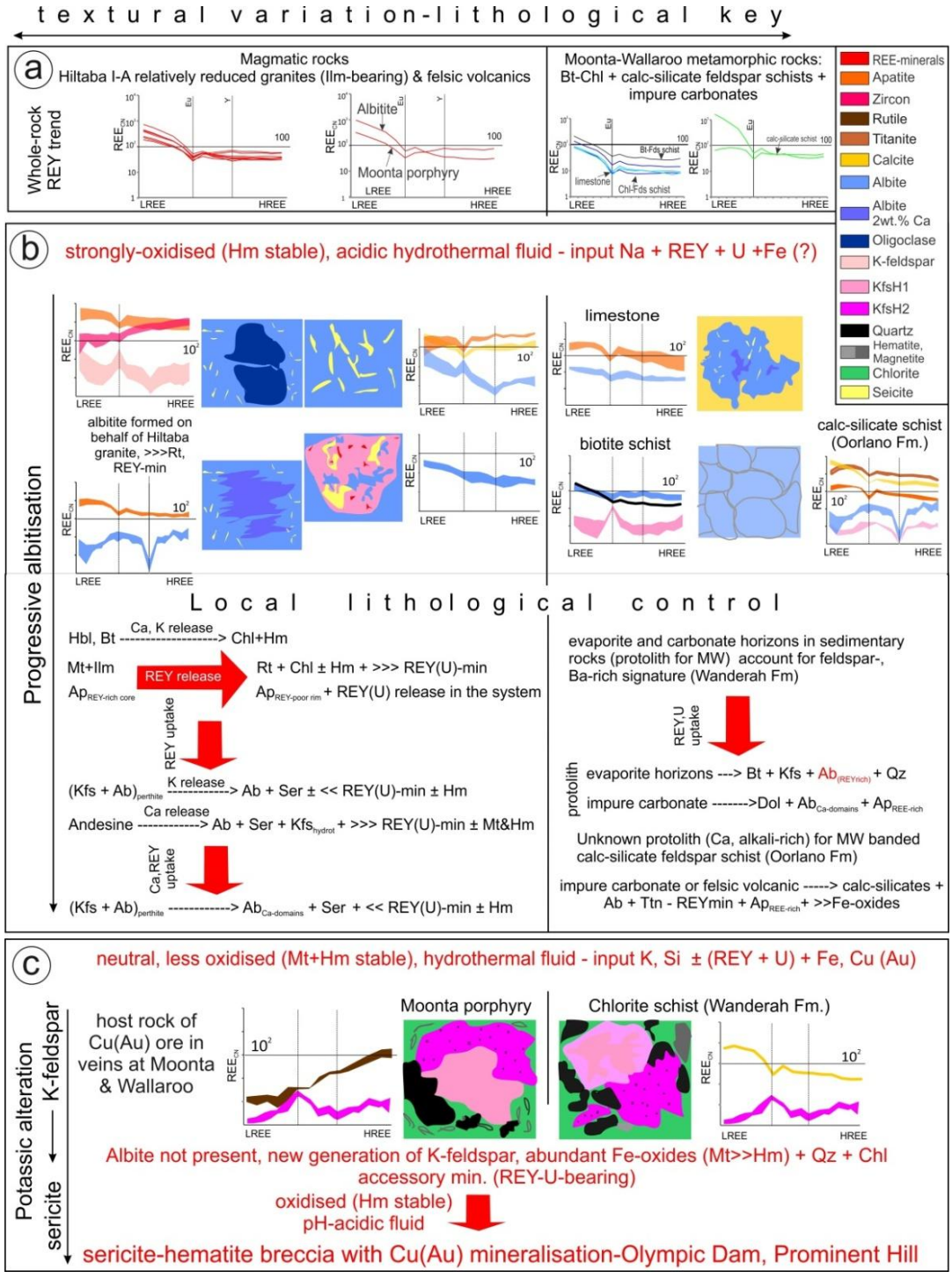

Figure 13: Schematic diagram showing development of alkali-metasomatism expressed by varying textures and geochemical signatures within main lithologies. Legend applies to (b) and (c). (a) Chondrite-normalised REY trends from whole-rock analyses of magmatic and metamorphic rocks (based on data from Forbes, 2012). (b) Key textures, REY-mineral trends and mineral reactions representing progressive albitization. Note the overlap between REY-trend of albite and whole-rock REY pattern (black) in the biotite schist (c) Key textures, REY-mineral trends and mineral assemblages representing potassic alteration from K-feldspar to sericite dominant.

POTASSIC ALTERATION

Disappearance of albite and progressive stability of K-feldspar, which is associated with abundant Fe-oxides (magnetite forms but hematite is still stable), quartz and chlorite, requires interaction with a neutral-pH, lower fO_2 fluid (Figure 13c). This fluid, although hematite-stable, can be inferred to be less oxidised based on the presence of magnetite. The sense of the Ce-anomaly for K-feldspar in chlorite-schist also supports this interpretation (Figure 11a). In the present study, potassium alteration is expressed by K-feldspar stability in rocks hosting Cu-Au mineralization within veins in the Moonta-Wallaroo district. REY signatures and textures of K-feldspar in the chlorite-schist are strikingly comparable to those in the Moonta porphyry. Additionally, apatite records this stage in REY-depleted rims whereas the Moonta porphyry shows formation of relatively HREE-enriched rutile (e.g. Figure 7f).

Such K-feldspar-dominant rocks could be protoliths for hematite-sericite breccias hosting Cu-Au mineralization, similar to Olympic Dam and Prominent Hill, if subjected to highly acid fluids and hydrolytic alteration.

Implications for IOCG genesis and exploration models

The findings of this study have several implications in terms of constraints of IOCG genetic models and their application in exploration. Albitization has been shown to be responsible for REY-U enrichment within the Moonta-Wallaroo region. This is a novel idea and is the first time that such a link has been tested and proven for an alteration stage otherwise considered barren (e.g. Hitzman *et al.* 1992; Williams *et al.* 2005). The data shows that although local lithologies may account for alkali-metasomatism, the

REE-U-enrichment requires an additional fluid source which is tied to magmatism. Thus, the present outcomes favour a dominant magmatic-model for REY-U-enriched IOCG mineralization (e.g. Pollard *et al.* 2007; Groves *et al.* 2010) over alternative basinal-derived metal sources (e.g. Barton & Johnson 2004; Chiaradia *et al.* 2006). However, this does not rule out the possibility of metal sources from leaching REY-rich protolith, such as pre-existing magmatic rocks, if these are present in a given area.

Furthermore, albitization is shown to increase the overall porosity of rocks during initial stages and thus promotes higher rates of fluid flow through the mineralising system. This makes albitization one of the quintessential processes in the development of characteristic alteration patterns within IOCG terranes. However, the question of how much metal endowment follows intense albitization remains open. Experimental evidence (Hövelmann *et al.* 2010) and interpretation of data here, obtained on a natural IOCG system, strongly support the idea that fluid changes are a response to dissolution-(re)-precipitation reactions leading from one type of alteration to another. Thus, the potassic alteration stage naturally follows albitization and leads to hydrolytic alteration (sericite-dominant), as in the Olympic Dam deposit. This opens up a debate on whether Olympic Dam is more advanced simply because of a greater fluid capacity than Moonta-Wallaroo. Alternatively, is Moonta-Wallaroo a deeper part of an Olympic Dam-style deposit of which the upper part has been eroded away?

The significance of feldspar trace element signatures has also been highlighted. The fact that albitization redistributes a range of trace elements – all of which are recorded in

mineral signatures - clearly validates its importance in understanding a complex petrogenetic history.

Trace element signatures in K-feldspar reflect the transition from magmatic to hydrothermal stages within the evolving IOCG system. The low-REY concentration in magmatic K-feldspar of the Hiltaba suite granitoids provides the regional background signature for Moonta-Wallaroo and Hillside areas, which can be tested for the entire Olympic Province. If this is proven, the practical application of these signatures will be an invaluable tool for exploration, leading to targeted drilling/sampling and subsequently improving time and cost efficiency.

CONCLUSIONS

This study allows the following conclusions to be made:

- REY-signatures of feldspars and accessory minerals are geochemical tracers of alteration stages within a magmatic-hydrothermal system.
- There is a strong link between albitization and REE-U-enrichment in IOCG deposits. This is because albitization consumes, redistributes and locks-in REY, LILE and HFSE via complex fluid-rock reactions dependent on the pre-existing mineral assemblages and fluid characteristics.
- This pilot study provides a model for IOCG-driven alkali metasomatism. Defining the boundaries between albitization and the concentration of anomalous REY in a ‘fertile’ IOCG terrane, and regional-scale alkali metasomatism requires testing in other terranes, including those in which metasomatism might be only the product of regional metamorphism.

- Geochemical data on fresh magmatic rocks and pre-metamorphic protoliths will better constrain the source of Na during alkali metasomatism e.g. Na-rich fluids (mixing of magmatic + metamorphic fluids?) or sedimentary sequences (evaporites etc.).
- Trace element signatures in K-feldspar reflect the transition from magmatic to hydrothermal stages within an evolving IOCG system. Such signatures could prove invaluable in exploration since they allow alteration associated with mineralization to be distinguished from background. This deserves to be tested elsewhere in the Olympic Province.

ACKNOWLEDGMENTS

I wish to sincerely express my gratitude to my supervisors, Dr. Cristiana L. Ciobanu and A/Prof Nigel Cook, for their advice, support and valuable guidance in the preparation of this thesis. Their generosity was considerable in investing so much time and effort. I would like to acknowledge the Deep Exploration Technologies Cooperative Research Centre for their project opportunities and financial contribution. I would also like to acknowledge Dr. Caroline Forbes for sample contribution and preliminary data, and Roniza Ismail for her assistance. Finally, I would also like to thank the staff at Adelaide Microscopy, in particular Deputy Director Angus Netting, Dr. Benjamin Wade, Aoife McFadden and Ken Neubaur for their training, assistance and sample preparation.

REFERENCES

BARTON, M. D. & JOHNSON, D. A. 2004. Footprints of Fe-oxide (-Cu-Au) systems, *University of Western Australia Special Publication* **33**, 112-116.

BASTRAKOV, E. N., SKIRROW, R. G. & DAVIDSON, G. J. 2007. Fluid evolution and origins of iron oxide Cu-Au prospects in the Olympic Dam district, Gawler Craton, South Australia, *Economic Geology* **102:8**, 1415-1440.

BAU, M. 1991. Rare-earth element mobility during hydrothermal and metamorphic fluid-rock interaction and the significance of the oxidation state of europium *Chemical Geology* **93:3**, 219-230.

BAU, M. & DULSKI, P. 1995. Comparative study of yttrium and rare-earth element behaviours in fluorine-rich hydrothermal fluids, *Contributions to Mineralogy and Petrology* **119:2-3**, 213-223.

BELOUSOVA, E. A., GRIFFIN, W. L., O'REILY, S. Y. & FISHER, N. I. 2002a. Apatite as an indicator mineral for mineral exploration: trace-element compositions and their relationship to host rock type, *Journal of Geochemical Exploration* **76:1**, 45-69.

BELOUSOVA, E. A., GRIFFIN, W. L., O'REILY, S. Y. & FISHER, N. I. 2002b. Igneous zircon: trace element composition as an indicator of source rock type, *Contributions to Mineralogy and Petrology*

143:5, 602-622.

BELPERIO, A., FLINT, R. & FREEMAN, H. 2007. Prominent Hill: A Hematite-Dominated, Iron Oxide Copper-Gold System, *Economic Geology* **102:8**, 1499-1510.

BELPERIO, A. & FREEMAN, H. 2004. Common geological characteristics of Prominent Hill and Olympic Dam-Implications for iron oxide coppergold exploration models, *Australian Institute of Mining Bulletin, Nov-Dec. Issue*, 67-75.

CAO, M., LI, G., QIN, K., SEITMURATOVA, E. Y. & LIU, Y. 2012. Major and trace element characteristics of apatites in granitoids from Central Kazakhstan: implications for petrogenesis and mineralization, *Resource Geology* **62:1**, 63-83.

CHIARADIA, M., BANKS, D., CLIFF, R., MARSCHIK, R. & DE HALLER, A. 2006. Origin of fluids in iron oxide–copper–gold deposits: constraints from δ 37Cl, 87Sr/86Sri and Cl/Br, *Mineralium Deposita* **41:6**, 565-573.

CIOBANU, C.L., WADE, B., COOK, N.J., SCHMIDT MUMM, A. & GILES, D. (in press). Uranium-bearing hematite from the Olympic Dam Cu-U-Au deposit, South Australia; a geochemical tracer and reconnaissance Pb-Pb geochronometer. Precambrian Research, doi:10.1016/j.precamres.2013.10.007

CONOR, C., RAYMOND, O. L., BAKER, T., TEALE, G., SAY, P. & LOWE, G. 2010. Alteration and Mineralisation in the Moonta-Wallaroo Copper-Gold Mining Field Region, Olympic Domain, South Australia. In PORTER T. M. ed. Hydrothermal Iron Oxide Copper-Gold & Related Deposits: A Global Perspective - Advances in the Understanding of IOCG Deposits. Adelaide: PGC Publishing, 1-24

COWLEY, W., CONOR, C. & ZANG, W. 2003. New and revised Proterozoic stratigraphic units on northern Yorke Peninsula, *MESA Journal* **29**, 46-58.

CUNEY, M. 2010. Evolution of uranium fractionation processes through time: driving the secular variation of uranium deposit types, *Economic Geology* **105:3**, 553-569.

DAVIDSON, G. J., PATERSON, H., MEFFRE, S. & BERRY, R. F. 2007. Characteristics and origin of the Oak Dam East breccia-hosted, iron oxide Cu-U-(Au) deposit: Olympic Dam region, Gawler craton, South Australia, *Economic Geology* **102:8**, 1471-1498.

EHRIG, K., MCPHIE, J. & KAMENETSKY, V. 2012. Geology and mineralogical zonation of the Olympic Dam Iron Oxide Cu-U-Au-Ag deposit, South Australia.

FERRIS, G. M., SCHWARZ, M. P. & HEITHERSAY, P. 2002. The geological framework, distribution and controls of Fe-oxide and related alteration, and Cu–Au mineralisation in the Gawler Craton, South Australia. Part I, Geological and tectonic framework, *Hydrothermal iron oxide copper-gold and related deposits: A global perspective* **2**, 9-31.

FLEET, M. E. & PAN, Y. 1994. Site Preference of Nd in Fluorapatite [Ca_{10} $(PO_4)_6F_2$], *Journal of Solid State Chemistry* **112:1**, 78-81.

FORBES, C. 2012. Report on production of first version of top of basement solid geology map for the central Yorke Peninsula, Project 3.2/3.3: Yorke Peninsula Project, *DET CRC*

GOLDSCHMIDT, V. M. 1937. The principles of distribution of chemical elements in minerals and rocks. The seventh Hugo Müller Lecture, delivered before the Chemical Society on March 17th, 1937, *Journal of the Chemical Society (Resumed)*, pp. 655-673.

GROVES, D. I., BIERLEIN, F. P., MEINERT, L. D. & HITZMAN, M. W. 2010. Iron oxide copper-gold (IOCG) deposits through earth history: implications for origin, lithospheric setting, and distinction from other epigenetic iron oxide deposits, *Economic Geology* **105:3**, 641-654.

HAND, M., REID, A. & JAGODZINSKI, L. 2007. Tectonic framework and evolution of the Gawler craton, southern Australia, *Economic Geology* **102:8**, 1377-1395.

HAYWARD, N. & SKIRROW, R. 2010. Geodynamic setting and controls on iron oxide Cu-Au (±U) ore in the Gawler craton, South Australia, *Hydrothermal iron oxide copper-gold and related deposits: A global perspective, volume 3, advances in the understanding of IOCG deposits*, pp. 105-131.

HITZMAN, M. W., ORESKES, N. & EINAUDI, M. T. 1992. Geological characteristics and tectonic setting of proterozoic iron oxide (Cu-U-Au-REE) deposits, *Precambrian Research* **58:1**, 241-287.

HITZMAN, M. W. & VALENTA, R. K. 2005. Uranium in iron oxide-copper-gold (IOCG) systems, *Economic Geology* **100:8**, 1657-1661.

HÖVELMANN, J., PUTNIS, A., GEISLER, T., SCHMIDT, B. C. & GOLLA-SCHINDLER, U. 2010. The replacement of plagioclase feldspars by albite: observations from hydrothermal experiments, *Contributions to Mineralogy and Petrology* **159:1**, 43-59.

ISMAIL, R., CIOBANU, C.L., COOK, N.J., GILES, D., SCHMIDT MUMM, A. & WADE, B. (in press). Rare

Earths and other trace elements in minerals from skarn assemblages, Hillside iron oxide-copper-gold deposit, Yorke Peninsula, South Australia, Lithos doi:10.1016/j.lithos.2013.07.023

MCPHIE, J, KAMENETSKY, V., ALLEN, S., EHRIG, K., AGANGI, A. & BATH, A. 2011. The fluorine link between a supergiant ore deposit and a silicic large igneous province, *Geology* **39: 11**, 1003-1006.

POLLARD, P. J. 2006. An intrusion-related origin for Cu–Au mineralization in iron oxide–copper–gold (IOCG) provinces, *Mineralium Deposita* **41: 2**, 179-187.

RAKOVAN, J. F. & HUGHES, J. M. 2000. Strontium in the apatite structure: strontian fluorapatite and belovite-(Ce), *The Canadian Mineralogist* **38:4**, 839-845.

RAYMOND, O., FLETCHER, I. & MCNAUGHTON, N. 2002. Copper-gold mineral systems in the south-eastern Gawler Craton-Another Mt Isa Eastern succession. Geological Society of Australia Abstracts. pp. 69-69. Geological Society of Australia; 1999.

REID, A., HAND, M., JAGODZINSKI, E., KELSEY, D. & PEARSON, N. 2008. Paleoproterozoic orogenesis in the southeastern Gawler Craton, South Australia, *Australian Journal of Earth Sciences* **55:4**, 449-471.

REID, A. J. & HAND, M. 2012. Mesoarchean to Mesoproterozoic evolution of the southern Gawler Craton, South Australia, *Episodes*- **35:1**, 216.

RUANO, S. M., BOTH, R. A. & GOLDING, S. D. 2002. A fluid inclusion and stable isotope study of the Moonta copper-gold deposits, South Australia: evidence for fluid immiscibility in a magmatic hydrothermal system, *Chemical Geology* **192:3-4**, 211-226.

SKIRROW, R. G. & ASHLEY, P. M. 2000. Proterozoic Cu–Au systems of the Curnamona Province—members of a global family, *MESA Journal* **19**, 48-50.

SKIRROW, R. G., BASTRAKOV, E., DAVIDSON, G. J., RAYMOND, O. L. & HEITHERSAY, P. 2002. The geological framework, distribution and controls of Fe-oxide Cu-Au mineralisation in the Gawler Craton, South Australia. Part II-alteration and mineralisation. in - Porter, T.M. (Ed), 2002 - Hydrothermal Iron Oxide Copper-Gold and Related Deposits: A Global Perspective, *PGC Publishing*, *Adelaide* **2**, 33-47.

SKIRROW, R. G., BASTRAKOV, E., EVGENIY, N., BAROVICH, K., FRASER, G. L., CREASER, R. A., FANNING, C. M., RAYMOND, O. L. & DAVIDSON, G. J. 2007. Timing of iron oxide Cu-Au-(U) hydrothermal activity and Nd isotope constraints on metal sources in the Gawler craton, South Australia, *Economic Geology* **102: 8**, 1441-1470.

SMITH, M., HENDERSON, P. & CAMPBELL, L. 2000. Fractionation of the REE during hydrothermal processes: constraints from the Bayan Obo Fe-REE-Nb deposit, Inner Mongolia, China, *Geochimica et Cosmochimica Acta* **64:18**, 3141-3160.

SMITH, M., HENDERSON, P., JEFFRIES, T. E., LONG, J. & WILLIAMS, C. T. 2004. The rare earth elements and uranium in garnets from the Beinn an Dubhaich Aureole, Skye, Scotland, UK: constraints on processes in a dynamic hydrothermal system, *Journal of Petrology* **45:3**, 457-484.

SMITH, M., STOREY, C. D., JEFFRIES, T. E. & RYAN, C. 2009. In situ U–Pb and trace element analysis of accessory minerals in the Kiruna district, Norrbotten, Sweden: new constraints on the timing and origin of mineralization, *Journal of Petrology* **50:11**, 2063-2094.

STIX, J. & GORTON, M. P. 1990. Variations in trace element partition coefficients in sanidine in the Cerro Toledo Rhyolite, Jemez Mountains, New Mexico: Effects of composition, temperature, and volatiles, *Geochimica et Cosmochimica Acta* **54:10**, 2697-2708.

TRAIL, D., BRUCE WATSON, E. & TAILBY, N. D. 2012. Ce and Eu anomalies in zircon as proxies for the oxidation state of magmas, *Geochimica et Cosmochimica Acta* **97**, 70-87

VAN DONGEN, M., WEINBERG, R. F. & TOMKINS, A. G. 2010. REE-Y, TI, and P remobilization in magmatic rocks by hydrothermal alteration during Cu-Au deposit formation, *Economic Geology* **105: 4**, 763-776.

WILLIAMS, P. J., BARTON, M. D., JOHNSON, D. A., FONTEBOTÉ, L., DE HALLER, A., MARK, G., OLIVER, N. H. S. & MARSCHIK, R. 2005. Iron oxide copper-gold deposits: geology, space-time distribution, and possible modes of origin, *Economic Geology* **100**, 371-405.

WILLIAMS, P. J. & POLLARD, P. J. 2001. Australian Proterozoic iron oxide-Cu-Au deposits: An overview with new metallogenic and exploration data from the Cloncurry district, northwest Queensland, *Exploration and Mining Geology* **10:3**, 191-213.

ZANG, W. L., FANNING, G. M., PURVIS, A. C., RAYMOND, O.L. & BOTH, R. A. 2007. Early Mesoproterozoic bimodal plutonism in the southeastern Gawler Craton, South Australia, *Australian Journal of Earth Sciences* **54:5**, 661-6

APPENDIX A: DETAILS OF ANALYTICAL METHODOLOGY

Samples were set in epoxy resin and prepared as one-inch polished blocks for mineralogical and petrographic analysis.

Electron Probe Microanalysis (EPMA)

Cameca SX-Five Electron Probe Microanalyser operated at an accelerating voltage of 20 kV and beam current of 20 nA. Standards, X-ray lines, count times and typical minimum detection limits (mdl) for this work are given in the table below.

Element	Standard	X-ray line	Count time (s) unknown/background	Average mdl (ppm)
Na	Albite	Na Kα	20/10	120
K	Sanadine	K Kα	20/10	130
Ca	Wollastonite	Ca Kα	20/10	120
Mn	Rhodonite	Mn Kα	20/10	300
Mg	Almandine	Mg Kα	20/10	220
Fe	Almandine	Fe Kα	20/10	350
Al	Almandine	Al Kα	20/10	250
Si	Almandine	Si Kα	20/10	300
Ti	Rutile	Ti Kα	20/10	150
F	Synthetic CaF_2	F Kα	30/15	300
Cl	Tugtupite	Cl Kα	30/15	200
P	Apatite	P Kα	20/10	200
Sr	Celestite	Sr Lα	20/10	600
Y	Synthetic REE-aluminosilicate	Y Lα	20/10	380
Zr	Synthetic zircon	Zr Lα	20/10	325
La	La-Ca-Al-silicate	La Lα	20/10	395
Ce	Ce-Ca-Al-silicate	Ce Lα	20/10	540
Pr	Pr-Ca-Al-silicate	Pr Lß	20/10	900
Nd	Nd-Ca-Al-silicate	Nd Lß	20/10	750
Sm	Sm-Ca-Al-silicate	Sm Lß	20/10	860
Eu	EuF_3	Eu Lß	20/10	1500
Gd	Gd-Ca-Al-silicate	Gd Lß	20/10	1000
Tb	Tb metal	Tb Lα	20/10	580
Dy	Dy-Ca-Al-silicate	Dy Lß	20/10	600
Ho	Ho metal	Ho Lα	20/10	1100
Er	Er-Ca-Al-silicate	Er Lß	20/10	640
Yb	Yb metal	Yb Lα	20/10	1000
Hf	Zircon	Hf Lα	20/10	740
Ta	Ta metal	Ta Lα	20/10	1025
W	W metal	W Lα	20/10	750

Pb	Synthetic Pb-silicate	Pb Mß	20/10	375
Th	Huttonite	Th Mα	20/10	1500
U	UO_2	U Mß	20/10	360

Laser-Ablation Inductively-Coupled Mass Spectrometry (LA-ICP-MS)

All multi-element LA-ICP-MS data was collected on a Resonetics M-50-LR 193-nm Excimer laser microprobe coupled to an Agilent 7700cx Quadrupole ICP-MS (AM-UoA). This new-generation laser system offers excellent spatial resolution coupled with sub-ppm level sensitivity for most trace elements.

Trace element spot analysis was made with a uniform spot size diameter of 30 µm for silicates and 22 µm for oxides and phosphates. The laser system was operated at pulse rates of 10 Hz and power levels of 50% power level; laser energy was typically 6-9 J/cm^{-2}, giving an ablation rate of approx. 1.5µm/s^{-1}. The following basic set of isotopes were monitored: ^{23}Na, ^{24}Mg, ^{27}Al, ^{29}Si, ^{31}P, ^{39}K, ^{43}Ca, ^{45}Sc, ^{47}Ti, ^{48}Ti, ^{49}Ti, ^{51}V, ^{53}Cr, ^{55}Mn, ^{57}Fe, ^{58}Fe, ^{59}Co, ^{60}Ni, ^{65}Cu, ^{66}Zn, ^{69}Ga, ^{75}As, ^{85}Rb, ^{88}Sr ^{89}Y, ^{90}Zr, ^{93}Nb, ^{95}Mo, ^{118}Sn, ^{133}Cs, ^{137}Ba, ^{139}La, ^{140}Ce, ^{141}Pr, ^{146}Nd, ^{147}Sm, ^{153}Eu, ^{157}Gd, ^{159}Tb, ^{163}Dy, ^{165}Ho, ^{166}Er, ^{169}Tm, ^{172}Yb, ^{175}Lu, ^{178}Hf, ^{181}Ta, ^{182}W, ^{206}Pb, ^{207}Pb, ^{208}Pb, ^{232}Th and ^{238}U. Multiple isotopes of Fe and Ti were measured to test for data consistency. Analysis time for each spot analysis was a uniform 90 seconds, comprising a 30-second measurement of background (laser-off), and 60-second analysis of the unknown (laser-on).

Standard reference materials for all mineral matrices were NIST-610 using coefficients given by Pearce *et al.* (1997). Standards were run after each 20-24 unknowns; detection limits were calculated for each element in each spot analysis. Internal calibration was achieved using concentration values of Al (feldspars), Ca (apatite, calcite, and titanite), Ti (rutile) and Zr (zircon), using values obtained via EPMA. Data reduction was performed using Glitter software (Van Achterbergh *et al.* 2001).

LA-ICP-MS element maps of different-sized areas of large K-feldspar and albite grains were generated to obtain visual images of trace element distributions. Mapping was conducted using the same Resonetics M-50-LR instrument as above. The M-50 instrument utilizes a two-volume small volume ablation cell (Laurin Technic Pty designed for excellent trace element sensitivity (e.g. Müller *et al.* 2009). Ablation was performed in an atmosphere of UHP He (0.7 l/min), and upon exiting the cell the aerosol cell is mixed with Ar (0.93 l/min) immediately after the ablation cell, after which the mix is passed through a pulse-homogenizing device or "squid" prior to direct introduction into the torch. The ICPMS was optimized daily to maximize sensitivity on isotopes of the mass range of interest, while keeping production of molecular oxide species (i.e. $^{232}Th^{16}O/^{232}Th$) and doubly charged ion species (i.e. $^{140}Ce^{2+}/^{140}Ce^{+}$) as low as possible, and usually <0.2%.

Imaging of grains was performed by ablating sets of parallel line rasters in a grid across the sample. A beam size of 6 – 22 µm (depending on desired resolution and counts) and

a scan speed of 1.5 x beam size (μm/s) were chosen which resulted in the desired sensitivity of elements of interest, and adequate spatial resolution for the study. To ensure the lines covered the entire selected area, spacing between lines was always equal to the beam size. The effect of redeposition during mapping was minimized by pre-ablating each line prior to its main data collection run. A laser repetition of 10 Hz was selected at a constant energy output of 100 mJ, resulting in an energy density of ≈6 J/cm^2 at the target. Using these beam conditions depth of ablation during mapping was around 5-10 μm. A set of 21 elements were analyzed with dwell time for all masses set to 0.003 seconds, resulting in a total sweep time was ~0.07 seconds. A 30 second background acquisition was acquired at the start of every raster, and to allow for cell wash-out, gas stabilization, and computing processing, a delay of 20 seconds was used after each line. Identical rasters were done on USGS reference glasses NIST SRM 610 at the start and end of a mapping run. Further details of practices used in the University of Adelaide LA-ICP-MS laboratory, particularly with respect to generation of trace element maps, are given by Cook *et al.* (2013).

Element maps were compiled and processed using the program Iolite developed by the Melbourne Isotope Group at Melbourne University (e.g. Woodhead *et al.* 2007). Iolite is an open source software package for processing ICP-MS data, and is an add-in for the data analysis program Igor developed by WaveMetrics. A typical mapping run was analyzed over a 6-7h session, in which significant instrument drift could occur. To correct for this, standards were analyzed immediately before and after the run to assess drift and if present, was corrected for by applying a linear fit between the two sets of standards. Following this, for each raster and every element, the average background was subtracted from its corresponding raster, and the rasters were compiled into a two-dimensional image displaying combined background/drift corrected intensity for each element.

References

COOK, N.J., CIOBANU, C.L., MERIA, D., SILCOCK, D., WADE, B., 2013. Arsenopyrite-pyrite association in an orogenic gold ore: tracing mineralization history from textures and trace elements. *Economic Geology* **108**, 1273-1283.

MULLER, W., SHELLEY, M., MILLER, P. & BROUDE, S. 2009 Initial performance metrics of a new custom-designed ArF excimer LA-ICPMS system coupled to a two-volume laser-ablation cell, *Journal of Analytical Atomic Spectrometry* **24**, 209–214.

PEARCE N.J.G., PERKINS W.T., WESTGATE J.A., GORTON M.P., JACKSON S.E., NEAL C.R. & CHENERY S.P. 1997 A compilation of new and published major and trace element data for NIST SRM 610 and NIST SRM 612 glass reference material, *Geostandards Newsletter: The Journal of Geostandards and Geoanalysis* **21**, 115–144.

VAN ACHTERBERGH, E., RYAN, C.G., JACKSON, S.E. & GRIFFIN, W.L. 2001 LA-ICP-MS in the Earth Sciences - Appendix 3, data reduction software for LA-ICP-MS, in Sylvester, P.J., ed., Short Course volume **29**: St. John's, *Mineralogical Association of Canada*, 239-243.

WOODHEAD, J.D., HELLSTROM, J., HERGT, J.M., GREIG, A. & MAAS, R. 2007 Isotopic and elemental imaging of geological materials by laser ablation inductively coupled plasma-mass spectrometry, *Geostandards and Geoanalytical Research* **31**, 331–343.